Behavior of Dust in the Martian Atmosphere

Thesis by

Anthony Domenick Toigo

In Partial Fulfillment of the Requirements

for the Degree of

Doctor of Philosophy

California Institute of Technology

Pasadena, California

2001

(Submitted May 18, 2001)

Acknowledgements

I would like to acknowledge all of the people who made this thesis possible and successful:

To my parents for supporting me throughout my life and giving me the courage to pursue my dreams. There aren't words to describe how grateful I am for their love and support, and the influence they have had on making me who I am.

To my brothers, Mark and Michael: our sibling rivalry made me strive for the best, but their friendship helped me to be my best.

To my advisor, Andy Ingersoll for being a singular mentor and an ever-full fountain of good advice.

To Mark Richardson, my collaborator and sponge to absorb all of my pessimism. Without his infinite well of wisdom and optimism, I would probably have never made it this far.

To my thesis committee, Andy Ingersoll, Arden Albee, Yuk Yung, and Bruce Murray, whose constructive criticism fluctuated between being more constructive and being more critical, but was always helpful. Special thanks to Bruce Murray for making the second half of my stay in Japan possible and introducing me to some treasured new Japanese friends.

To the support staff at Caltech, especially Irma and Mike Black, who helped with all of the small administrative and computer details, which left me free to selfishly concentrate on learning and finishing my thesis.

To my officemates, Antonin Bouchez, Huiqun (Helen) Huang, and Lori Fenton, for putting up with my complaining and my music, and for being great conversation partners when any one of us needed a short break from work.

To Albert and Sue Haldemann, who let me be their adopted bitter middle child, and knew when I needed to be pulled away from the office.

To all of my friends, too numerous to name, but especially to Chris Nolte and the planetary cabal of Mark Roulston, Matt Pritchard, Sarah Stewart, Shane Byrne, Mark Richardson, Mark Abolins, and Hari Nair, who helped keep me sane during my extended stay and prevented me from doing harm to myself and to others. I don't know how I would've made it without any of them.

And finally to Jodi Nooyen, for whose love and emotional support I am eternally grateful.

Abstract

Two aspects of the dust cycle on Mars are examined: the seasonal variation of dust aerosols in the atmosphere as observed by spacecraft and dust lifting by high wind stress at the south pole during late spring employing a specially developed mesoscale atmospheric model. Reanalysis of Viking mission optical depth measurements shows that the visible to infrared ratio of total extinction opacity varies with season, and is due to seasonally varying water ice haze. The Martian atmosphere is clearer of dust, especially during northern spring and summer, than previously thought. Water ice hazes can provide roughly 50% of the total visible opacity in these seasons, and that they represent only $1-5\%$ of the total water column. Next, the conversion for use on Mars of a terrestrial mesoscale atmospheric model (the Mars MM5) is presented and described. Validation of the Mars MM5 is conducted by comparison with a general circulation model on scales of a few hundred kilometers and with Martian surface landers (Viking Lander 1, Viking Lander 2, and Mars Pathfinder) on scales of a few kilometers, and in both cases there is good agreement in the meteorological variables of temperature, pressure, and wind. Tides are found to be at least as important as slopes in generating the diurnal cycle of winds at the lander sites, in contrast to previous one-dimensional studies. Finally, assuming that dust injection is related to the movement of sand-sized grains or aggregates, the Mars MM5 predicts wind stresses of sufficient strength to initiate movement of sand-sized particles, and hence dust lifting, during late southern spring in the south polar region. It is found that the direct cap edge thermal contrast provides the primary drive for high surface wind stresses at the cap edge at this season while sublimation flow is not found to be particularly important. Comparison between simulations, in which dust is injected when wind stresses are high and those with inactive dust injection, show no signs of consistent feedback due to dust clouds on the surface wind

stress fields during the late spring season examined here.

Contents

List of Figures

1 Introduction

Dust on Mars is analogous to water on Earth in the key role it plays in both climate dynamics and the shaping of geology. The effect dust has on the absorption and re-radiation of energy is similar to the effect that water has on Earth's climate system through the latent heat exchange from the evaporation and condensation of water. Similarly, water is a major terrestrial erosional agent, whereas dust on Mars is an indicator of erosion. The deposition and movement of dust also plays a major role in shaping the surface of Mars.

The dust cycle intersects many other cycles on Mars, and thus a better understanding of the dust cycle leads to a better understanding of many other Martian systems. The amount, distribution, and properties of dust are crucial for modeling their radiative feedback on the atmospheric dynamical system. The role of dust particles as condensation nuclei is important in both the CO_2 and water cycles. The deposition and erosion of dust, as well as its variance throughout the history of Mars, are key for understanding the geology expressed on the surface today.

In this thesis I seek to explore the dust cycle in more detail. Since a detailed examination of the complete dust cycle would require too much time and length for a thesis, I have chosen to focus on two aspects of the cycle: the seasonal variation of dust aerosols in the atmosphere, and an analysis of dust lifting by high wind stress at the south pole during late spring.

First, a reexamination of the annual dust cycle during the Viking years is undertaken to better understand the seasonal variation in the dust cycle, and modify the long-held assumption that the optical depth of the atmosphere is controlled solely by dust in all seasons. Exploration of one mechanism for injecting dust into the atmosphere, at one specific area (near the south pole) and at one specific time (late southern spring), is also explored. This

investigation is made possible by the application of a new (with respect to application to the Martian environment) tool, the mesoscale atmospheric model, capable of investigating the small-scale (tens of meters to hundreds of kilometers) atmospheric motions and interactions with the surface. Thus, before the work on dust lifting at the south pole is given, a description of a new mesoscale atmospheric model for use on Mars, and its validation against previous models and *in situ* data, is presented.

The history of man's knowledge of dust on Mars dates back to the earliest telescopic observations. "Yellow clouds" were observed to obscure portions of the Martian disk at various times and locations. These were in contrast to "bluish" or "white clouds" that were also observed. We now know that the yellow clouds are dust clouds and that the white clouds are condensate (water or CO_2) clouds. With the arrival of spacecraft at Mars during the 20th century, we have been able to better quantify the amount, composition, and optical properties of dust in the Martian atmosphere, and thus begin to decipher its role in Martian systems as described above.

One of the most important measures of dust is the optical depth of the atmosphere. It is this quantity, in combination with the optical properties of dust particles (e.g., single scattering albedo) which is used in models to determine the radiative feedback of suspended dust particles. However, since the actual mass of dust is hard to measure directly, it is necessary to use knowledge of the optical depth, in combination with appropriate knowledge of dust optical properties and density and the distribution of particle sizes, to convert from optical depth at a given wavelength to mass. In this way transport of material can be quantified.

The current view of the dust cycle on Mars derives from Viking Lander measurements of optical depth at visible wavelengths. The Infrared Thermal Mapper instrument aboard the Viking Orbiters allowed for a determination of the optical depth of the atmosphere in a silicate absorption band at infrared (9 μm) wavelengths. The observations at different wavelengths allowed the opacity to be separated into contributions due to dust and water

ice. The seasonal variation of the ratio of optical depth in the visible to the infrared leads to an investigation of the seasonal cycle of aerosols, both dust and water, in Chapter 2.

The mechanisms by which dust is lifted from the surface and injected into the Martian atmosphere have not been fully investigated. Several theories have been put forth to explain the raising of dust, such as: dust fountaining by explosive desorption of CO_2 and water, small convective vortices ("dust devils"), unstable atmospheric conditions, movement triggered by impact from larger particles (saltation), and clumping of dust grains to form larger particles which are then more easily mobilized. Investigation of some of these processes requires modeling atmospheric motion at very small scales. Similarly, the development of local and great dust storms, and the transition from the former to the latter, also requires knowledge of small-scale atmospheric motions and their interaction with surface. With these motivations in mind, I set out to convert a pre-existing terrestrial mesoscale model, the Pennsylvania State University/National Center for Atmospheric Research Fifth Generation Mesoscale Model (MM5), for use on Mars. The terrestrial version, used for weather prediction, is widely used in the meteorology community, and has decades of use and support behind it. Thus its accuracy and reliability (after appropriate conversions to Martian conditions) make it ideal for investigating small-scale atmospheric motions, especially as they relate to the dust cycle. Chapter 3 describes the model, its conversion to Martian use, and calibration of the model by comparison of model simulations on a global scale with general circulation models, and with Martian lander meteorological measurements on the local (a few to tens of kilometers) scale.

An investigation of dust lifting processes using this new tool is undertaken in Chapter 4. Mars Global Surveyor observations of local dust storms and clouds near the receding south polar seasonal cap during late southern spring motivate an attempt to model how these storms are created. Under the assumption that sand-sized particles are being mobilized (either as aggregates of dust or as triggering particles), the occurrence of high wind stresses sufficient to initiate mobilization is investigated. Different forcing parameters (e.g., slopes,

thermal contrast, sublimation flow) are isolated to find which one is dominant in creating high cap-edge wind stresses. Simulations where large amounts of dust are injected at locations of high wind stress are compared to Mars Global Surveyor observations of dust activity at this time.

Finally, in Chapter 5, a summary of these works, their conclusions, and possibilities for future investigations is presented.

2 Seasonal Variation of Aerosols in the Martian Atmosphere[1]

Abstract

Reanalysis of Viking Lander (VL) visible and Viking Orbiter infrared optical depth measurements shows that the visible to infrared ratio of total extinction opacity varies with season. The ratio is near to its previously reported constant value, 2.5, during dust storm periods and higher during northern spring and summer. The increase in ratio is hypothesized to be due to seasonally varying water ice haze, which produces a higher optical depth in the visible than in the infrared. This differs significantly from previous analyses of VL visible opacities, which have assumed that only dust contributes to the optical depth measured during the early afternoon. Consequently it is suggested that the Martian atmosphere is clearer of dust, especially during northern spring and summer, than previously suggested based upon VL data. Dust visible optical depths are 0.1 – 0.4 during the northern spring and summer seasons, compared to previous estimates of 0.4 – 0.6. Water ice hazes provide roughly 50% of the total visible opacity in these seasons. For southern spring and summer, dust optical depths are more variable, but generally $\geq$0.4, with water ice opacity $\leq$0.1. The data suggest water ice optical depths are slightly higher and peak earlier (L_s=80° – 90°) at VL1 than at VL2 (L_s=115° – 130°). Average northern summer water (daytime minimum) ice masses are estimated to be roughly 0.1 – 0.5 precipitable microns, depending on the assumed particle size distribution and hence 1 – 5% of the total water column. The observation of significant and previously unrecognized amounts of water ice haze suggests a larger role for water in controlling atmospheric heating rates and the vertical distribution of

[1] Anthony D. Toigo and Mark I. Richardson, *Journal of Geophysical Research*, Vol. 105, No. E2, Pages 4109–4121, 2000,

dust and water vapor than has been widely accepted to date.

2.1 Introduction

Dust has a profound impact on the Martian atmosphere. It is both an effective absorber of solar radiation and an effective emitter/absorber of thermal infrared radiation. Consequently, the amount and distribution of dust in the atmosphere significantly affects atmospheric heating rates and hence the circulation [*Zurek et al.*, 1992]. Thus characterization of the seasonal dust cycle is of prime importance in understanding the current Martian climate.

The seasonal cycle of dust on Mars is the keystone to the other seasonal cycles because of its impact on atmospheric temperature structure and transport and, through this, its impact on volatile cycles and climate. The current standard view of the dust cycle derives from Viking Lander (VL) measurements of the visible optical depth since the optical depth of the atmosphere provides a measure of the amount of suspended aerosols. The key assumption in the interpretation of these data has been that only dust significantly contributes to the daytime opacity [*Pollack et al.*, 1979; *Colburn et al.*, 1989] and hence that the amount of atmospheric dust can be directly derived from them. However, dust is not the only aerosol in the Martian atmosphere. Water ice and CO_2 ice particles also form in the atmosphere [*Curran et al.*, 1973; *Herr and Pimental*, 1969], and while CO_2 ice particle formation is limited to the winter polar regions and high altitudes, water ice particles can form at most latitudes and at most seasons.

The optical depth of the atmosphere has also been measured in the infrared by the Viking Orbiters' Infrared Thermal Mapper (IRTM) instruments [*Martin*, 1986; *Martin and Richardson*, 1993]. Through observations of the depth of the 9 μm silicate absorption feature relative to the 7 μm "continuum," these measurements theoretically allow the derivation of dust optical depth independent of other aerosols. However, water ice particles can

affect the infrared opacity, though to a much smaller degree than in the visible. The ratio of dust optical depth in the visible to that in the infrared has physical significance in that the opacity in the visible is a gauge of the effectiveness of solar heating due to dust absorption, while the opacity in the infrared represents the ability of the atmosphere to radiate heat to space through infrared emission by dust. The ratio is also of diagnostic importance as it is sensitive to dust properties. The value of the visible to infrared ratio for dust has typically been taken to be constant at roughly 2.5 [*Martin*, 1986]. Again assuming that dust is the only aerosol, this fixed value of the opacity ratio has been used in atmospheric circulation model heating rate calculations as well as to help constrain dust particle properties, such as composition and particle size distribution.

Seasonal variation in this ratio would have a wide range of implications. However, the ratio has not been derived for a good fraction of the annual cycle. Variations in the ratio as a function of season could imply that aerosol populations have been incorrectly assessed in the past (i.e., neglecting water ice aerosols is not valid), that dust particle size distributions vary significantly, or that our current understanding of the vertical distribution of dust is wrong. In any case, opacity ratio variations reflect variations in atmospheric aerosol properties that are not incorporated in current atmospheric radiative models, and hence, circulation models. This study was begun in order to examine any temporal variations in this ratio and found a significant seasonal cycle with northern summer peak values exceeding 20. In section 2.2 the means by which the ratio was derived is described and the seasonal variations are shown. Then, in section 2.3 three likely causes for the variation are discussed. The options are changes in the dust particle size distribution, changes in the vertical distribution of dust, or variations in the amount of dust and water ice in the atmosphere. Indeed, the conclusion is that the primary cause must be a significant contribution to opacity by water ice hazes (the phrases "water ice," "water ice hazes," and "water ice clouds" will be used interchangeably) during northern spring and summer, arguing that the standard interpretation of VL opacity as being solely a measure of dust must be abandoned. Next, in

section 2.4 the Mars Pathfinder optical depth measurements are reanalyzed in terms of the mixed dust/water ice model. In section 2.5 the results are discussed within the context of a new picture of Mars climate. Finally, in section 2.6 the conclusions are reviewed, primarily that water ice hazes play a significantly greater role in the seasonal aerosol cycle than has been previously suspected.

2.2 Data

The most widely reported measurements of the atmospheric optical depth are those derived from the VL cameras. Both landers measured optical depth by directly imaging the Sun at various zenith angles in the broadband solar channel centered on 670 nm [*Pollack et al.*, 1977, 1979; *Colburn et al.*, 1989]. These are shown in Figures 2.1a and 2.1d. Data have been filtered to show only the afternoon values, where the water ice cloud contribution will be at a minimum [*Colburn et al.*, 1989]. The common assumption is that this minimum corresponds to the absence of water ice clouds and that the opacity observed at these local times is due entirely to dust. The graphs show a relatively clear northern spring and summer (L_s=0° – 180°) with visible optical depths of 0.4 – 0.7. Values for VL2 are slightly smaller, due to its position at higher elevation and the fact that aerosol opacity roughly scales with atmospheric mass [*Kahn et al.*, 1981]. A more dusty southern spring and summer (northern fall and winter, L_s=180° – 360°) is also apparent, including the two great dust storms of 1977 during which visible optical depths reached values in excess of 3.

The retrieval of optical depth in the infrared (9 μm) from IRTM observations has been described by *Martin* [1986] and *Martin and Richardson* [1993]. Using the corrected IRTM 15 μm brightness (T_{15}) temperatures [*Wilson and Richardson*, 2000], the surface emissivities of *Christensen* [1982], and the two-stream source-function radiation code of *Zurek* [1981], the infrared optical depths for the first two Viking years were rederived. Additionally, the two-stream code was modified to treat nonuniform (i.e., nonconstant mixing

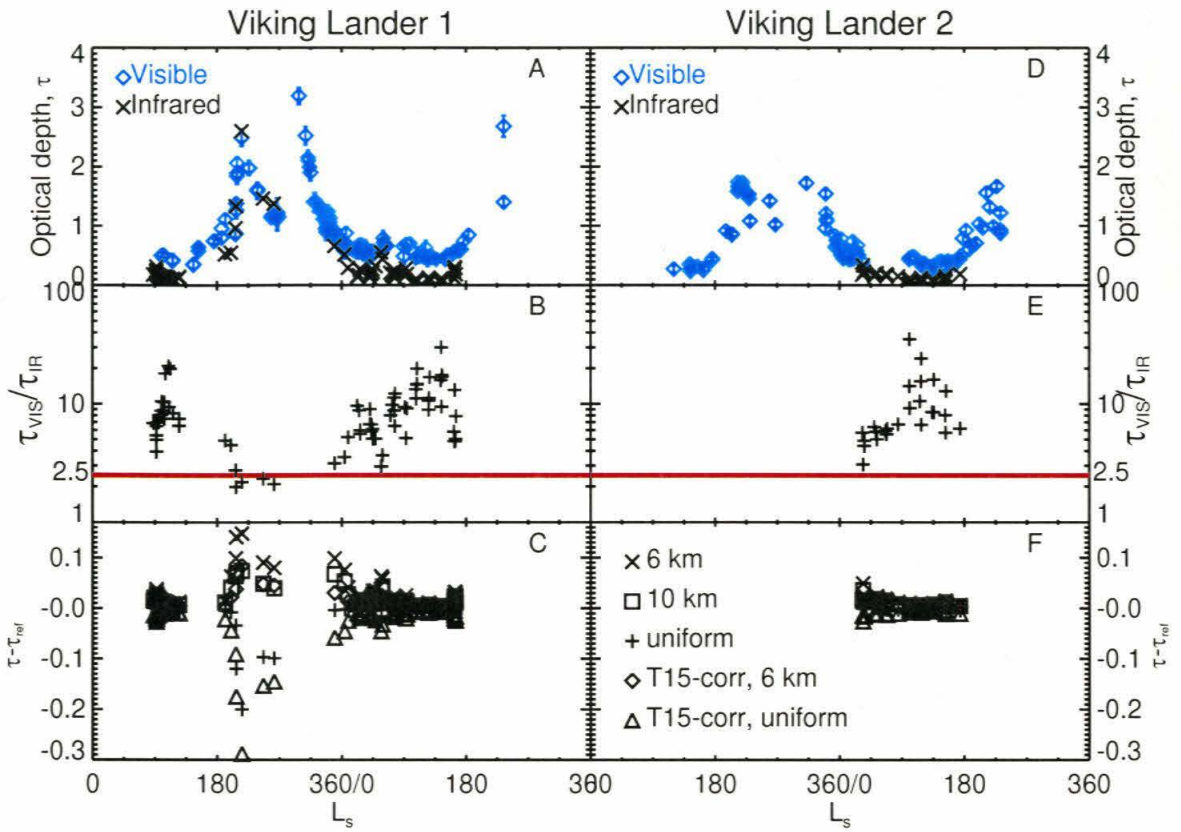

Figure 2.1: (a) Optical depth versus L_s for the Viking Lander 1 location. L_s values range from 0 to 720, with 360−720 representing the second Martian year of Viking observations. Viking Lander derived values are shown in blue diamonds, with their associated error bars. The Infrared Thermal Mapper (IRTM) derived values are shown as black crosses. The IRTM values have been scaled by a factor of 2.5 to show their good agreement during dusty periods (L_s=180°−360°) and their lack of agreement during the clear periods (L_s=0°−180°). (b) Plot of the ratio of visible to infrared optical depths versus L_s for the Viking Lander 1 location. (c) Difference between the derived infrared optical depths for the reference case (using corrected T_{15} temperatures and dust confined to 1 scale height) and optical depths derived for various combinations of corrected and uncorrected T_{15} temperatures and dust distributed uniformly, to 10 km, and to 6 km. (d)–(f) Similar to Figures 2.1a−2.1c, respectively, except for the Viking Lander 2 location.

ratio) vertical distributions of dust. Once again, it is common to assume that these infrared opacities are due to atmospheric dust alone. While the effect of water ice on these opacities will certainly be smaller than on the visible opacities, the impact is likely non-negligible and is addressed in section 2.3. The derived values of 9 μm optical depths are shown in Figures 2.1a and 2.1d in conjunction with the visible opacities. The infrared data shown in Figures 2.1a and 2.1d correspond to IRTM observations near both landing sites. The infrared data included in this study fell within a $5° \times 5°$ latitude-longitude box centered on each lander and had emission and incidence angles $<60°$ (to minimize atmospheric mass effects). The infrared values have been scaled up by the canonical factor of 2.5 to more readily highlight deviations from this assumed constant ratio value. The general cycle of orbiter-derived opacity followed that of the landers.

The ratio of optical depths (visible to infrared) of 2.5 was derived by *Martin* [1986] by comparing Viking Orbiter and VL data sets during the dusty southern summer period; comparison during the rest of the annual cycle was not pursued due to the "very low opacities in that period" [*Martin*, 1986, p. 9]. The concern was that random noise in these low-opacity data would make meaningless any comparison with the visible opacities. However, Figures 2.1a and 2.1d show that the random variation in opacities is consistently less than the difference between the visible and infrared opacities, even when scaled by 2.5; therefore, comparison outside the dust storm season is valid.

A very clear trend in the opacity behavior emerges when the visible and infrared values are compared over the full annual cycle. While the seasonal trends in the visible and infrared optical depths at each landing site are similar, the infrared optical depths are lower during northern spring and summer than the VL values, even after scaling the values by the canonical factor of 2.5.

The error bars for the visible opacity are shown. The error is harder to quantify for the infrared data; however, there is enough infrared data that the random error can be gauged from the scatter of individual data points. Again, it is important to note that the scaled

infrared values are consistently lower than the visible values in the northern spring and summer seasons. Even in the unlikely event that the infrared opacities are biased low by the 10 – 25% error that *Martin* [1986] quotes, the scaled infrared opacities would still be lower than the visible values.

The derivation of infrared opacities uses the T_{15} temperatures, which have been shown to be biased by surface temperatures during the middle portion of the day [*Wilson and Richardson*, 2000]. As infrared opacities during the late morning and early afternoon were derived, the impact of the corrected T_{15} temperatures on the model temperature profile constructed within the optical depth retrieval code were examined. The results are shown in Figures 2.1c and 2.1f. It can be seen that during relatively dust-free periods the difference between opacities derived using corrected and uncorrected T_{15} temperatures is roughly 10%.

All previous derivations of 9 μm infrared opacity [*Martin*, 1986; *Martin and Richardson*, 1993; *Fenton et al.*, 1997] have used a uniform distribution of dust. However, this may not always be appropriate, and so, the sensitivity of optical depth retrievals to varying vertical distributions of dust was tested. A vertical distribution of dust that is capped at 10 km was chosen as the standard case (the mixing ratio as a function of height was described following *Conrath* [1975] using $\nu = 0.5$). This height was chosen as it likely represents a realistic lower bound on the depth of dust mixing during the northern spring and summer period [*Richardson*, 1999]. Additionally, opacities for a uniform vertical distribution and for an extremely shallow distribution capped at 6 km ($\nu = 1$) (Figures 2.1c and 2.1f) were calculated.

It is clear from Figures 2.1a and 2.1d that while a visible to infrared ratio of 2.5 is good for dusty periods (southern spring and summer), the ratio increases significantly during the clearer periods (northern spring and summer). The visible to infrared ratios derived by comparing the infrared observations with those from VL are shown in Figures 2.1b and 2.1e. A strong anti-correlation can be seen between the ratio and opacity. The ratio reaches

its minimum near 2.5 during the extremely dusty periods and increases both in value and in its variation during the clear periods.

2.3 Interpretation

There are three possible explanations for the increased ratio during the clear periods: (1) changes in the mean size of suspended dust particles, which would vary the visible to infrared ratio assuming that the total extinction is due to dust, (2) confinement of dust within a shallower layer of the atmosphere, which would produce an underestimate of infrared opacity (and an overestimate of the ratio) when retrieved assuming a uniform vertical distribution of dust, and (3) increased visible opacity due to the presence of previously neglected water ice clouds, while the dust visible to infrared opacity ratio is assumed to remain constant.

2.3.1 Changes in the Dust Particle Size Distribution

The settling and removal of larger dust particles following dusty periods may result in the shrinking of both the mean size of the particle size distribution and the width of the distribution, leading to increased visible to infrared ratios as the smaller particles exert more influence in the visible wavelengths. Figure 2.2 shows a plot of the dependence of the visible to infrared opacity ratio as a function of cross-section weighted mean particle size and effective width for spherical particles. Although the ratio increases with decreasing mean particle size and decreasing width of the distribution, the ratio never reaches values as high as those seen during the clear northern spring and summer seasons. Particle scattering calculations using nonspherical particles [*Pollack and Cuzzi*, 1980] can increase the ratio somewhat for a given effective radius (r_{eff}) and distribution width (v_{eff}); however, the increase does not reach the values seen in Figures 2.1b and 2.1e, except for distributions with very small effective radii and which are unrealistically narrow (r_{eff} <0.4μm and v_{eff} <0.1,

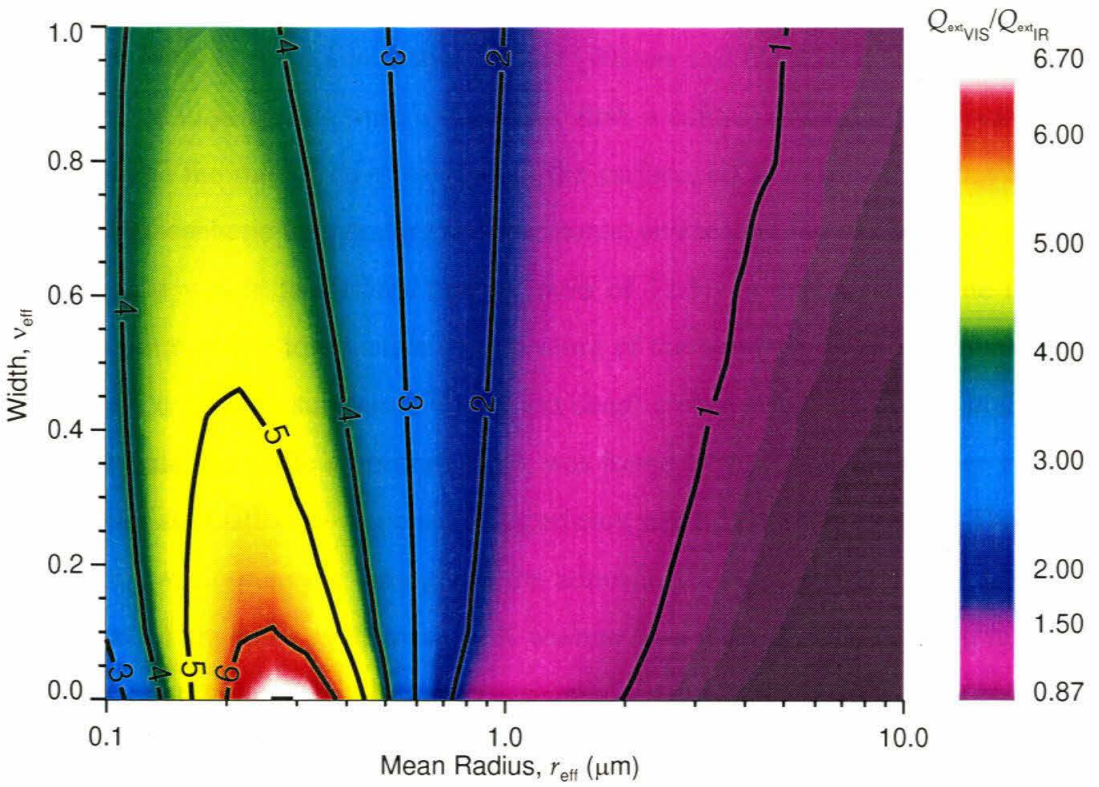

Figure 2.2: Ratio of optical depths in the visible and infrared as a function of cross-section weighted mean particle size (r_{eff}), in microns, and effective width of the distribution (v_{eff}) for a modified gamma distribution of spherical dust particles. Indices of refraction in the visible came from *Ockert-Bell et al.* [1997] and in the infrared from *Toon et al.* [1977]. Note that modified gamma distribution has three independent variables, α, γ, and $\mathrm{r_{mode}}$ (r_{eff} is a function of all three, and v_{eff} is a function of α and γ), one of which is usually held constant. A constant value of $\alpha = 2$ was chosen for consistency with *Toon et al.* [1977] and *Pollack et al.* [1979]. The visible to infrared opacity ratio (as a function of r_{eff} and v_{eff}) is relatively insensitive to the choice of α.

Figure 2.2) (see *Pollack et al.* [1995] for a review).

It is interesting to consider the impact of a high visible to infrared ratio of optical depth on the behavior of an atmospheric model, assuming that dust provides the only source of opacity. Such an experiment was undertaken with the Geophysical Fluid Dynamics Laboratory Mars General Circulation Model [*Wilson and Hamilton*, 1996]. Specifically, two numerical experiments were undertaken: first, a control simulation that was carefully tuned, through the rate of dust injection at the surface, so as to match Viking IRTM and Mariner 9 atmospheric temperature measurements; and second, an otherwise identical simulation with a visible to infrared opacity ratio of 12.5. In keeping with the fact that a high ratio corresponds to effective solar heating of the atmosphere and relatively ineffective cooling to space, a substantial (5–10 km deep) global inversion, absent in the control simulation (and hence the spacecraft data), was found to form near the surface of the high opacity ratio simulation in response to significant net heating due to dust. The effect of dust heating was noticeable throughout the atmosphere below roughly 50 km, with temperatures at 10 km being as much as 25 K warmer than those in the control simulation and 10 K warmer at 25 km. The deep inversion greatly reduced lower atmospheric convection and lead to a sharp reduction in dust lifting such that after 30 sols (Mars days) the opacities had dropped by a rough factor of 2 relative to the control simulation. In short, high dust visible to infrared ratios do not appear to be consistent with the Martian atmosphere as it is observed [*Zurek et al.*, 1992], and thus a seasonal variation of the dust (as opposed to total aerosol) visible to infrared opacity ratio by the amounts suggested in Figures 2.1a and 2.1b is not physically credible.

A final argument against the dust particle size variation relates to the fact that if the visible to infrared optical depth ratio were varying significantly during the year due to dust alone, the spectral shape of the 9 μm silicate absorption feature should also change. In Figure 2.3, the variation of dust extinction in and around the 9 μm absorption feature is shown for two combinations of (r_{eff},v_{eff}): (0.3 μm, 0.0) and (1.8 μm, 0.5). These two combinations

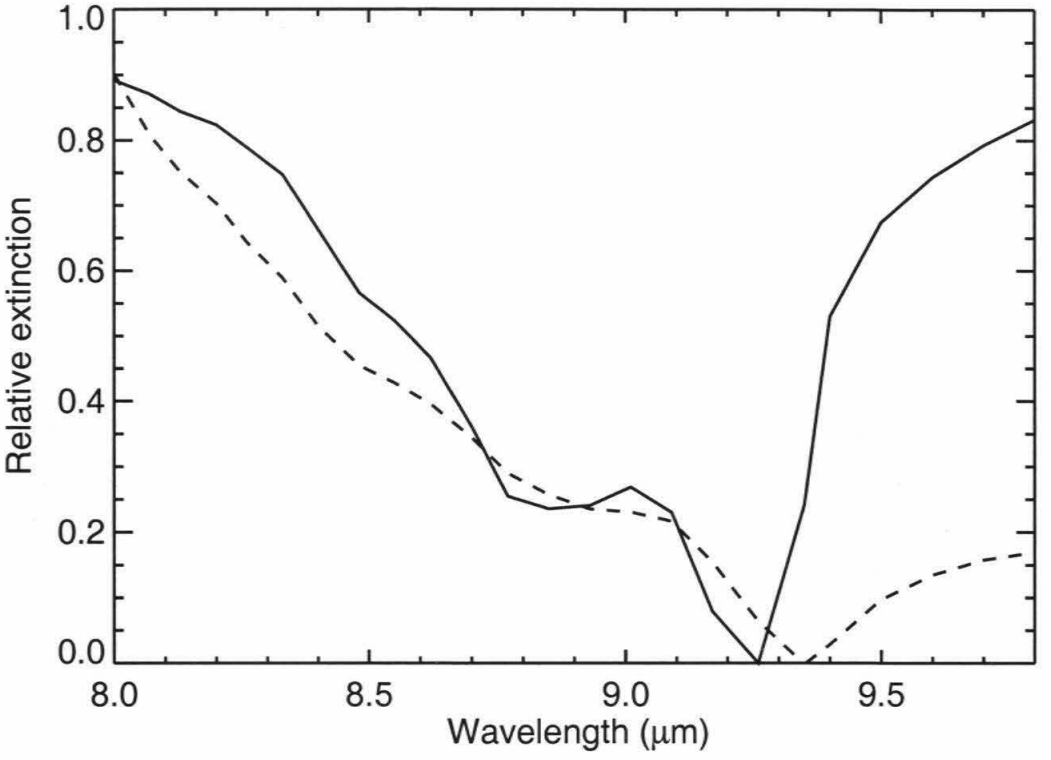

Figure 2.3: Relative extinction due to dust particles as a function of wavelength, assuming spherical particles. The solid line represents a dust particle size distribution with $r_{\text{eff}} = 0.3$ μm and $v_{\text{eff}} = 0.0$, which yields a visible to infrared optical depth ratio of approximately 6.5. The dashed line represents a dust particle size distribution with $r_{\text{eff}} = 1.8$ μm and $v_{\text{eff}} = 0.5$ (similar to the particle size distributions derived by *Pollack et al.* [1995] and *Smith and Lemmon* [1999]), which yields a visible to infrared optical depth ratio of approximately 1.5. Refractive indices are from *Toon et al.* [1977].

correspond to visible to infrared ratios of 6.5 and 1.5, respectively. There is a significant difference in the shape longward of 9.25 μm, and there is a noticeable secondary maxima in extinction at 8.8 μm in the former case, which is absent in the latter. However, analysis of recent Thermal Emission Spectrometer (TES) data [*Smith et al.*, 2000a; *Bandfield et al.*, 2000] has shown that the dust absorption spectra are fairly invariant with time (excluding the earliest phases of dust storms). This provides a strong indication that the dust particle size distribution is not varying significantly. Further, the absence of a secondary minima in most TES and Mariner 9 Infrared Interferometer Spectrometer (IRIS) spectra suggests that particle size variations cannot explain visible to infrared opacity ratios as large as 6.

2.3.2 Changes in the Vertical Distribution of Dust

Another potential explanation for the ratio variations relates to variations in depth to which dust is mixed. Specifically, it could be argued that if a uniform vertical distribution of dust is assumed in the retrieval of infrared opacities, while the true distribution had dust confined to relatively low heights in the atmosphere, the actual dust opacity would be underestimated by the retrieval, relative to dust distributed deeply through the atmosphere. Dust confined lower in the atmosphere is warmer and hence has a higher emission temperature. This results in a smaller difference in the brightness temperatures at 7 and 9 μm. Consequently, more dust (opacity) is needed to fit a given observed T_7 (7 μm brightness temperature) minus T_9 (9 μm brightness temperature) value in the confined dust case. In order to address this possibility the radiative scheme used by *Martin* [1986] and *Martin and Richardson* [1993] was modified to treat arbitrary vertical dust distributions. The results for uniform, moderately confined (to 10 km), and shallowly confined (to 6 km) dust distributions are shown in Figures 2.1c and 2.1f. Dust distributions shallower than 6 km were not considered since at the low and midlatitude landing sites, the daytime boundary layer depth should in general be roughly 6 km [*Haberle et al.*, 1993]. This effect of dust distribution assumption

on the retrieval turns out to be rather small. It is <10% for clearer periods, increasing greatly during the dusty conditions of southern summer. However, during these periods the most likely case is a close to uniform distribution.

The explanation for the relatively small impact of the dust distribution assumption (for reasonable ranges) on retrieval opacity is rather straightforward. "Uniform" dust refers to a constant dust mass mixing ratio as a function of height, which means that the total dust amount decreases exponentially with height (along with pressure). The difference between a uniform and a shallowly confined distribution is that while the dust amounts in the former decrease exponentially with height to the top of the atmosphere, the confined dust case has dust amounts decreasing exponentially to 6 km and decreasing more rapidy above that level. However, in both cases, the majority of the dust mass (and hence opacity) is located in the lowest half-scale height of the atmosphere, where the distributions are very similar. In short, variation in dust vertical distribution cannot explain the magnitude of the observed variation in the visible to infrared opacity ratio.

2.3.3 Water Ice Hazes

These facts together suggest that the third hypothesis, added visible opacity due to water ice clouds, is more likely. Dusty periods lead to increases in atmospheric temperature, preventing the formation of water ice clouds. The clearer periods are colder, allowing water clouds to form more readily. Water ice clouds contribute opacity in visible wavelengths but much smaller amounts at the 7 and 9 μm wavelengths [*Curran et al.*, 1973; *Smith et al.*, 2000a] used for 9 μm optical depth retrieval, making the ratio of opacities increase. If it is assumed that the ratio of optical depth of dust (as opposed to total aerosol) in the visible to the infrared is truly 2.5, then Figure 2.4 shows the amount of opacity that is then due to water ice. Again it is important to note that daytime observations were used and, therefore, inferred water ice opacities and hence water ice mass estimates representative of

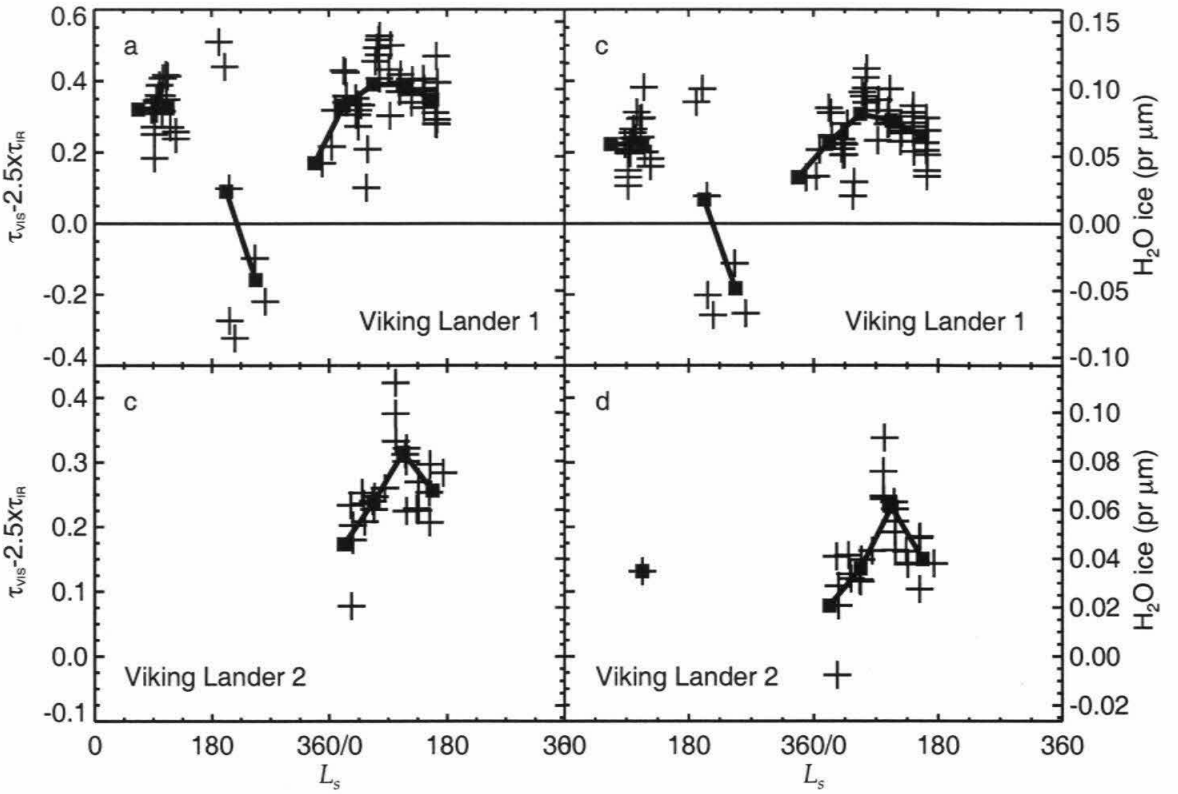

Figure 2.4: (a)–(b) Excess optical depth versus L_s for the Viking Lander 1 and 2 sites, respectively. Assuming the ratio of visible to infrared opacities for dust is a constant 2.5, $\tau_{\text{VIS}} - 2.5\,\tau_{\text{IR}}$ is a measure of the optical depth in the visible due to other opacity sources, such as water ice clouds. The boxes and lines are a boxcar average of all values in a 45° L_s box. A size of 45° in $L_s$was used to span gaps in the temporal coverage; averages over a shorter interval follow the random noise, and averages over a longer interval damp out seasonal trends. It was also assumed that there is no relative difference in T_7 and T_9 brightness temperatures due to water ice and that vertical dust distribution is capped at 10 km. The right-hand axis corresponds to the right-hand axis in Figures 2.4c and 2.4d, and indicates the amount of precipitable microns of water that would need to be converted to water ice aerosols to produce the whole amount of excess optical depth, using a modified gamma distribution ($\alpha = 8$, $\gamma = 3$, $r_{\text{eff}} = 0.3\,\mu$m, and $v_{\text{eff}} = 0.03$, see section 2.4) and the water ice optical parameters of *Warren* [1984]. (c)–(d) Excess optical depths similar to Figures 2.6a and 2.6b, except that a $T_7 - T_9$ difference of -1 K was assumed. The right hand axis shows the opacities converted to water ice amounts.

daytime minimum values. The right-hand axis shows the amount of precipitable microns of water that is necessary to be frozen into ice in order to produce the required optical depth, using a modified gamma distribution ($r_{\text{eff}} = 0.3\,\mu$m and $v_{\text{eff}} = 0.03$, see section 2.4) and the water ice refractive indices of *Warren* [1984]. If the particle size distribution derived by *Curran et al.* [1973] ($r_{\text{eff}} = 2\ \mu$m and $v_{\text{eff}} = 0.03$) is used, the values shown on the right-hand axis of Figure 2.4 should be multiplied by 4. Similarly, if the ice grows around a dust core, concentric shell calculations [*Bohren and Huffman*, 1983] show that an ice mantle of roughly the same thickness as the original dust core radius is sufficient to make the composite dust/ice particle indistinguishable from pure ice in the visible and infrared. In this case the masses shown on the right-hand axis overestimate the true ice mass as the amount of water needed to grow around a dust core is less than the amount needed to grow a pure ice particle. The ice mass estimates are therefore likely only accurate to the order of magnitude level.

Although previous studies have assumed that water ice is neglectible in the retrieval of 9 μm dust opacity, water ice can produce a spectral contrast between 7 and 9 μm. In Figure 2.5, the IRTM 7 and 9 μm channel brightness temperature differences are shown possible for a range of water ice particle size distributions assuming a surface temperature of 250 K, an ice cloud temperature of 200 K, and an ice cloud opacity of 0.4 in the visible. In these calculations the scattering and absorbing radiative model of *Paige et al.* [1994] and *Tamppari et al.* [2000] was used. These values represent the most extreme case (i.e., the case that will produce the largest ice cloud signal) that is still consistent with the opacity and IRTM temperature data. The $T_7 - T_9$ differences have a minimum value of approximately -1 K and are generally negative throughout most of the domain. The $T_7 - T_9$ values from the IRTM data set, used in the determination of dust opacity, typically have values between 0.7 and 1.5 K. Taking the extremum value of -1 K, from Figure 2.5, as the general impact of ice, suggests that the true $T_7 - T_9$ difference resulting solely from dust should be nearer 1.7 to 2.5 K. To test the impact of such $T_7 - T_9$ difference biasing by ice, the infrared

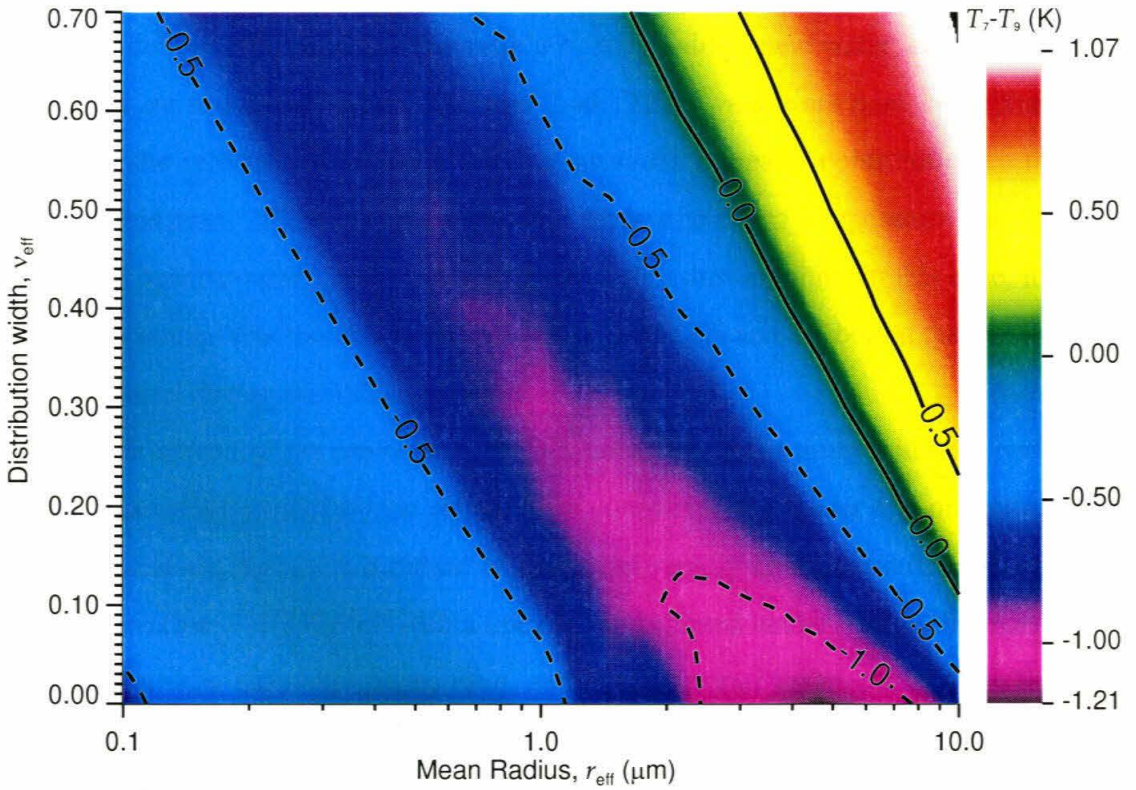

Figure 2.5: Difference between the IRTM T_7 (7 μm brightness temperature) and T_9 (9 μm brightness temperature) caused by water ice particles as a function of cross-section weighted mean particle size (r_{eff}), in microns, and effective width of the distribution (v_{eff}) for a modified gamma distribution of spherical dust particles. Indices of refraction came from *Warren* [1984]. The comment on the variables of the particle size distribution is the same as for Figure 2.2.

dust optical depth was retrieved for $T_7 - T_9$ values 1 K greater than was extracted from the IRTM data set. The resulting opacity values are shown in Figure 2.6 along with the standard values from Figures 2.1a and 2.1d. The increase in dust optical depth is only really significant during the relatively clear periods. Here the values increase from roughly 0.03–0.1 to 0.05–0.15. Applying the canonical dust opacity ratio of 2.5 and calculating the opacity deficit with respect to the visible opacity values, new water ice opacities were derived and are shown in Figures 2.4b and 2.4d. These values are now lower than those derived for the reference case since the dust provides a greater contribution to the total opacity in this case. Given the rather extreme surface-to-cloud temperature contrasts and the high ice opacity values used in deriving the higher dust amounts in this case, it can be reasonably claimed that the two cases shown in Figures 2.6 and 2.4 bound the true dust and water ice values during the Viking mission.

The wide spread of ice amounts at the VL sites during the dusty southern spring and summer seasons are caused by the difficulty of comparing the lander and orbiter observations of optical depth during a period of large and rapidly changing dust amounts. The IRTM observations are matched with a linearly interpolated lander opacity in order to calculate the visible to infrared opacity ratio, and thus the water ice amounts. This linear interpolation is valid during the relatively steady northern spring and summer, but introduces larger errors during the southern spring and summer periods of rapid change. However, one can tell the visible and infrared values produce a good match, using the ratio of 2.5, based on simple visual inspection of Figure 2.1.

A seasonal cycle of cloudiness can now clearly be seen in the data, with cloud opacity disappearing during the dust storm periods and peaking during the northern spring and summer. Although the data are noisy, the ice opacity values appear to peak around the northern solstice. There is even an indication that the peak at VL1 occurs earlier (L_s=80° – 90°) than at VL2 (L_s=115° – 130°). If true, these differences in timing may reflect a dependence of lower-latitude clouds on the strength of the overturning (Hadley) circulation,

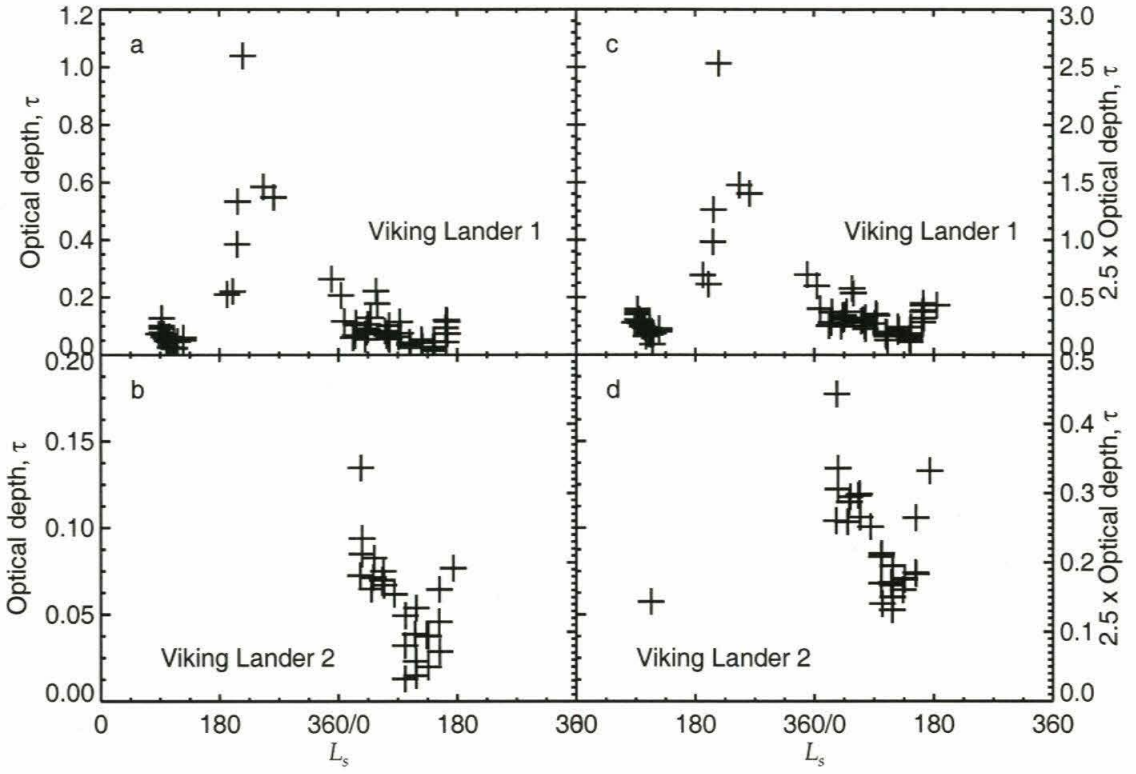

Figure 2.6: (a) – (b) Optical depths of dust in the infrared as a function of L_s for the Viking Lander 1 and 2 sites, respectively, assuming that there is no relative difference in T_7 and T_9 brightness temperatures due to water ice and that vertical dust distribution is capped at 10 km. The right-hand axis corresponds to the right-hand axis in Figures 2.6c and 2.6d, and shows the infrared values scaled by 2.5 for comparison with visible optical depths. (c) – (d) Dust optical depths in the infrared similar to Figures 2.6a and 2.6b, except that a $T_7 - T_9$ difference of -1 K was assumed to be due to water ice aerosols. The right-hand axis shows the opacities scaled by 2.5 for comparison with the visible.

while the higher-latitude clouds respond more to the increasing vapor amounts. In any case, this cycle of water ice is consistent with the cycle of water vapor observed by Mars Atmospheric Water Detector (MAWD) [*Jakosky and Farmer*, 1982], which peaks in the Northern Hemisphere during northern summer. A similar seasonal cycle of the apparition of water ice cloudiness and haziness has been reported by ground-based observers [*Beish and Parker*, 1990].

The values of "excess" optical depth due to water ice clouds in the Viking data, as well as the values derived from the Mars Pathfinder data, are of the order of a tenth to one precipitable micron. These are amounts that the atmosphere should have no difficulty supplying during these seasons given vapor amounts of a few tens of precipitable microns [*Jakosky and Farmer*, 1982]. The ice opacities derived are consistent with measurements of water ice opacity made in the ultraviolet by Hubble Space Telescope [*James et al.*, 1996] after scaling for the difference in wavelength. It is also important to note that the ice amounts derived refer to the daytime minimum values. Models suggest a diurnal cycle of cloud ice, involving up to a few precipitable microns [*Richardson*, 1999]. The daytime-derived values are not inconsistent with a cycle of this magnitude.

2.4 Reanalysis of Mars Pathfinder Optical Depths

Data from the Mars Pathfinder mission allow us to check the model of increased influence of water ice aerosols. The Imager for Mars Pathfinder (IMP) enabled the atmospheric optical depth to be measured at four wavelengths (0.45, 0.67, 0.883, and 0.989 μm). Changes in the particle size distribution of dust and water ice will change their respective absorption spectra (derived from Mie scattering calculations) at these wavelengths; consequently, the measured spectra can be used to constrain the particle size distributions of water ice and dust by shape fitting. Once the optimum distributions are computed, the mass fraction can be derived by matching to the total observed extinction. In this way it can be tested whether

the picture of the seasonal variation of aerosols presented in this work is consistent with the amount of dust and water ice opacity observed in the Mars Pathfinder measurements.

The IMP observations [*Smith and Lemmon*, 1999] show a similar amount of dust in the 0.67 μm region as the VL measurements for the 90 sols for which they operated (L_s=143° – 188°). In general, IMP saw similar or slightly higher optical depth in the blue filter compared to the red filter. *Smith and Lemmon* [1999] account for this extra opacity in the blue wavelengths with high-altitude Rayleigh-scattering ice particles. They note that this solution is not unique, and indeed, it was found that a haze of low-altitude ice particles also provides a fit to their wavelength-dependent observations.

The dust particle size distribution derived by *Tomasko et al.* [1999] and based upon the angular dependence of the Pathfinder spectral observations was used. The effective mean radius of their distribution ($r_{\text{eff}} = 1.6\,\mu$m) is in good agreement with previous Viking and Phobos measurements (see *Pollack et al.* [1995] for a summary), but they were unable to constrain the distribution width beyond a value of $v_{\text{eff}} \geq 0.2$. Thus the dust distribution widths were varied and both the effective radius and width of water ice distributions were also varied. It was found that the ice distribution specified by *Curran et al.* [1973] was unable to fit the Pathfinder opacity observations regardless of the dust distribution width. In fact, only ice distributions with an effective particle size ≤ 0.5 μm were capable of producing a fit, in combination with the dust distribution of *Tomasko et al.* [1999]. The width of the ice distribution was found to have a negligible effect on the quality of the fit or the derived dust/ice fraction. In addition, it was found that the best fit to the Pathfinder data, regardless of the ice distribution, was obtained with a dust distribution v_{eff} of 0.6. This is within the range specified by *Tomasko et al.* [1999] and should be viewed as a refinement of their estimate.

The Viking data for the Pathfinder observation period now allow us to constrain the ice particle size effective radius even further. The VL1 data for the Pathfinder period suggest a water ice contribution of optical depth in the 0.67 μm channel of 0.0 – 0.1. It was found that

an effective radius of 0.3 ± 0.1 μm produces red optical depths within this range. Figure 2.7 shows the solution for the amount of ice and dust necessary to fit both the Pathfinder and VL1 measurements of optical depth.

2.5 Current State of the Martian Climate

One of the primary results of the Viking mission was a detailed description of the current Martian climate. The annual cycles of atmospheric temperature, dust, and volatiles were defined by observations spanning several Martian years. However, *Clancy et al.* [1990, 1996] have recently suggested that this picture may not be representative of every, or even most, years. Specifically, they claimed that the bulk Martian atmosphere near 25 km is now (1980 – present) cooler by roughly 15 – 20 K than during the Viking period (1976 – 1980). Based upon Hubble Space Telescope observations, they also suggested that Mars is less dusty than was observed during the Viking era and emphasized both the presence of water ice clouds and their potential role in limiting the vertical distribution of dust (hence reducing atmospheric temperatures through decresed solar absorption).

It is now known that the Martian climate has not changed significantly between the Viking mission and more recent times [*Richardson*, 1998]. The discrepancy between air temperatures derived from Viking IRTM measurements and those derived from ground-based observations results from a systematic warm bias in the Viking observations [*Wilson and Richardson*, 2000]. The Viking year mean air temperatures now appear to agree with the more recent TES [*Conrath et al.*, 2000] and microwave observations [*Clancy et al.*, 2000]. However, both the Mars Pathfinder [*Smith and Lemmon*, 1999] and TES [*Smith et al.*, 2000b] measurements of optical depth were found to be in good agreement with Viking values. At first glance this would appear to be inconsistent with the downward revision of atmospheric temperatures, especially during the cool northern spring and summer seasons. Agreement between Viking and Pathfinder visible optical depths results mainly

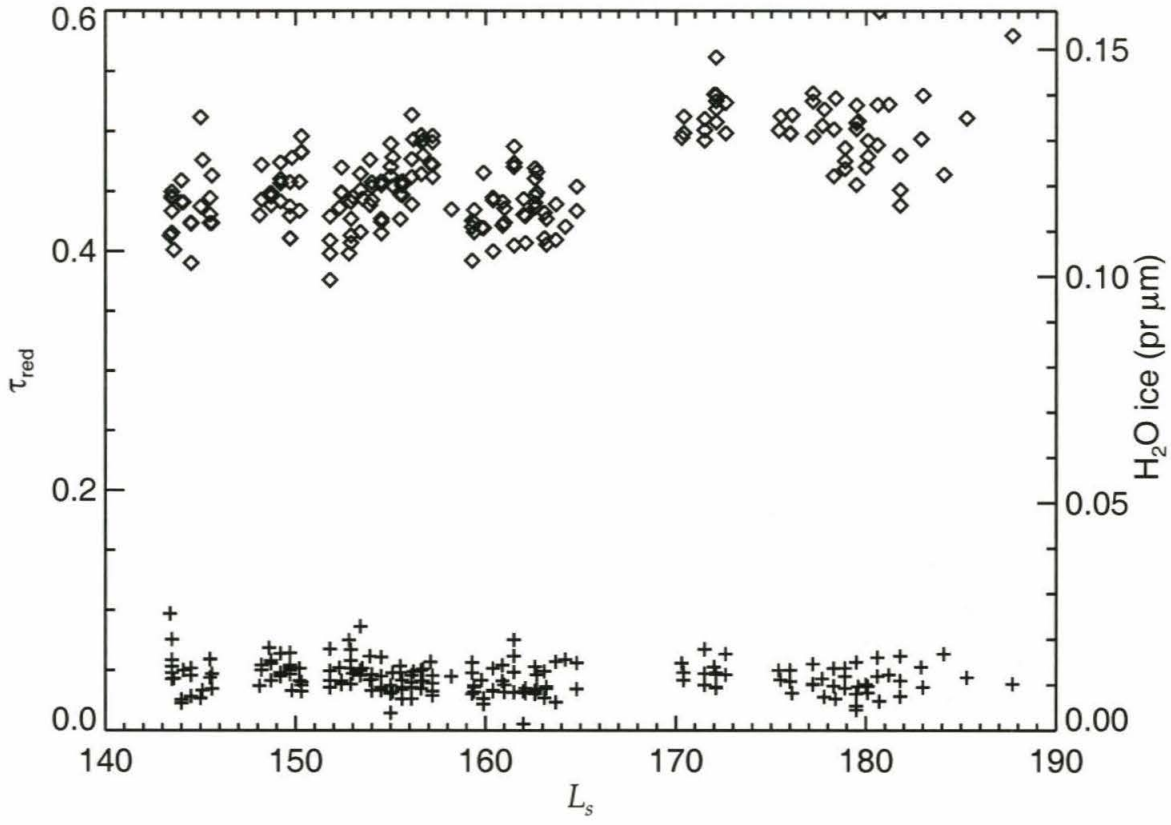

Figure 2.7: Derived values of optical depths of dust and ice in the red (0.67 μm) versus L_s for Mars Pathfinder. Only measurements made during the afternoon (after 1200 LT and before 1800 LT) were used in order to remove the diurnal water ice cycle. Diamonds are the dust optical depth, and crosses are the water ice optical depth (where optical depth solutions of 0.0 for ice have not been plotted). The particle size distribution of *Tomasko et al.* [1999] ($r_{\text{eff}} = 1.6\,\mu$m and $v_{\text{eff}} = 0.6$) was used for dust, while a modified gamma distribution with $r_{\text{eff}} = 0.3\,\mu$m and $v_{\text{eff}} = 0.03$ ($\alpha = 8$ and $\gamma = 3$) was used for ice. Refractive indices of *Ockert-Bell et al.* [1997] and *Warren* [1984] were used for dust and ice, respectively. These solutions were constrained by total optical depth measurements in the 0.45, 0.67, 0.883, and 0.989 μm filters. The right-hand axis indicates the amount of precipitable microns of water that would need to be converted to water ice aerosols to produce the water ice optical depth seen using the above-mentioned ice distribution.

from the fact that the Pathfinder observations occurred during the late northern summer, when atmospheric water ice constitutes a small fraction of the atmospheric aerosol load. For northern spring and summer the inconsistency is resolved by the recognition that previous analysis of the Viking visible optical depth measurements overestimated dust optical depths and by neglecting the water ice opacity. Thus the "new" picture of the Viking era includes lower atmospheric temperatures, lower dust opacities, and more atmospheric water ice.

The results of this study suggest that at least the northern spring and summer seasons are less dusty than generally interpreted, based on the Viking Lander observations. In addition, there is significant seasonal variation in the ubiquitous water ice haze. This latter suggestion is in keeping with recent Mars Orbiter Camera (MOC) [*Malin et al.*, 1998] observations and reanalysis of Viking IRTM data [*Tamppari et al.*, 2000], which show rather widespread haziness due to water ice. In general, evidence suggests a rather repeatable northern spring and early summer [*Richardson*, 1998; *Clancy et al.*, 2000; *Martin and Richardson*, 1993; *Smith et al.*, 2000b] and a downward revision of visible dust opacitites during these seasons would appear to help in reconciling atmospheric temperature and dust observations.

2.6 Summary and Conclusions

9 μm optical depths from the Viking IRTM data were rederived and compared them with measurements of visible opacity from the Viking Landers. The ratio of visible to infrared opacity, which is typically assumed to be constant, varies significantly with season. Both the visible and infrared opacities are usually assumed to relate only to the dust amount in the atmosphere. Indeed, two potential explanations for the opacity ratio variations that involve only variations in the dust properties were investigated. The first argues that variations in dust particle sizes affect the ratio. However, it was shown that realistic particle size variations can explain less than half the range in the derived opacity ratios, that even

these variations do not appear to be reasonable based on TES observations, and that such high ratios of visible-to-infrared dust opacity would result in an unrealistic atmospheric temperature structure and circulation. The second potential explanation argues that if dust is confined low in the atmosphere, the retrieval scheme (which assumes uniformly mixed dust) would underestimate the true infrared dust opacity. In this case the true opacity ratio would remain constant, but would appear to vary due to errors in the infrared opacity calculation. The retrieval scheme was modified to treat nonuniform dust, but found this explanation able to account for only 10% of the peak opacity ratio variation, even for dust confined to an unrealistically shallow column.

The most likely explanation for variations in the opacity ratio is the previously neglected role of persistent water ice hazes and clouds during northern spring and summer. The implication here is that the Viking-derived visible and infrared optical depths are not representative ofthe seasonal cycle of dust, but of the combined cycles of dust and atmospheric water ice. Thus Mars is less dusty and more cloudy than was believed on the basis of VL observations, especially during the northern spring and summer seasons. Visible optical depths during the northern spring and summer seasons are typically $0.1-0.4$ for dust and $0.1-0.4$ for water ice, during the daytime. During the rest of the year the water ice visible opacities fall below 0.1, while dust opacities vary greatly, but generally are above 0.4. The variations in dust and water ice opacities appear to be strongly anticorrelated. The ice amounts peak in early norther summer (with the opacities possibly peaking earlier at VL1 than at VL2), while the dust opacity is a minimum at these times. The ice mass amounts derived from the peak ice opacities are sensitive to ice particle sizes, but are of order $0.1-0.5$ pr μm. This is roughly $1-5\%$ of the total water column.

Using both the Pathfinder and Viking data, a tighter constraint on the dust particle size distribution of *Tomasko et al.* [1999] (r_{eff} =1.6 μm and v_{eff} = 0.6) was determined, and the background water ice size distribution (r_{eff} = 0.3 μm and v_{eff} = 0.03) was derived. However, the ice particle size distribution may change as a function of season. In addition,

we suggest that for dust the ratio of optical depth in the infrared to the visible is likely to lie near 2.5, and that consequently, models which use this constant value are likely not in error.

3 A Mesoscale Model for the Martian Atmosphere

Abstract

An existing, well-tested and well-documented mesoscale model, the Pennsylvania State University (PSU)/National Center for Atmosphere Research (NCAR) Mesoscale Model Version 5 (MM5), has been converted for use on Mars. A description of the model and its applicability to modeling various processes are provided. Modifications are based upon schemes implemented in the Geophysical Fluid Dynamics Laboratory (GFDL) Mars General Circulation Model (GCM). Validation of the Mars MM5 is conducted by comparison with the GFDL Mars GCM in order to examine the comparability of the large-scale dynamics in the two models. The agreement between the two models on similar scales (a few hundred kilometers) is shown to be good. Validation is also performed against both Viking Landers and Mars Pathfinder meteorological observations with the model run at much higher vertical (lowest level at 1.6 m) and horizontal resolution (a few kilometers). Good agreement with near-surface air temperature, pressure, and wind direction observations is found. These results demonstrate that the model accurately simulates surface heat balance and the propagation of global thermal tides. However, wind speeds are underpredicted. The model generates the correct phasing of wind speeds with local time at the Viking Lander 2 site during winter, but does not generate the correct phasing at the other sites or seasons. This suggests that further work on the variation of winds in the lower boundary layer needs to be done. The importance of slopes and global tides in generating the diurnal cycle of winds at the Viking and Pathfinder sites is examined. Tides are found to be at least as important as slopes, in contrast to previous one-dimensional studies. This study

suggests that when used in combination with a GCM, the Mars MM5 promises to be a powerful tool for the investigation of processes central to the Martian climate on scales from hundreds of kilometers to tens of meters.

3.1 Introduction

The study of dynamical processes operating within the Martian atmosphere has benefited greatly from the modification and application to Mars of atmospheric models developed for Earth. These models have provided insight into the dynamics of the Martian general circulation, including the response of the Hadley circulation to changes in aerosol heating [*Haberle et al.*, 1982; *Wilson*, 1997], and the behavior of the aerosol and volatile cycles [e.g., *Pollack et al.*, 1993; *Murphy et al.*, 1995; *Richardson*, 1999]. However, to date these models have been global and of sufficient resolution to resolve only synoptic scale processes (greater than a few hundred kilometers). Results from global models increasingly suggest the importance of smaller scale processes, for example, the lifting of dust from the surface and injection into the atmosphere, and the exchange of water with and transport of vapor to or from the northern polar cap. At the same time, high resolution thermal and imaging data from the Mars Global Surveyor are now available that require atmospheric models capable of resolving motions on scales of a few hundreds of meters to a few hundreds of kilometers. These data include observations of the polar regions, dust devils, dust storms, water ice cloud systems, and aeolian features.

In this paper, a Martian mesoscale model that is designed to address motions on scales smaller than resolvable by current numerical models of the atmosphere is introduced. The model is based on the Pennsylvania State University (PSU)/National Center for Atmosphere Research (NCAR) Mesoscale Model Version 5 (MM5) [*Dudhia*, 1993] and is fully converted to Martian conditions. The model is designed to work in tandem with a global model which provides initial and boundary conditions. The mesoscale model (Mars MM5)

simulates a limited domain within this global context, at resolutions ranging from 10^2 to 10^5 m. The model has been developed to address a number of outstanding problems in Martian atmospheric studies. These include:

- How is dust lifted from the surface and injected into the atmosphere?
- What is the nature of the polar regional circulation and how does the circulation moderate transport of aerosols and volatiles into and out of the polar caps?
- What processes are important in cloud formation?
- What controls the evolution and structure of Martian dust storm systems?
- How does the atmosphere interact with the surface in terms of mechanically eroding, transporting, and depositing sediment, and sculpting the surface?
- What processes control the dynamics of the boundary layer? How important are tides vs. slopes in generating the diurnal cycle of wind at the surface?

The application of the Mars MM5 to the problems listed above should advance the insight gained from other, more global, modeling efforts. However, an important task that must be undertaken first with such a complex model is to develop an understanding of how well the model performs compared both to well-validated global models and to appropriate observational data sets. Such a study is analogous to careful calibration and characterization of a particularly complex piece of experimental apparatus. Thus, the current paper has two purposes. The first is to fully describe the Mars MM5 and the physical parameterizations that distinguish it from the well-documented terrestrial MM5 model. This description is provided in Section 3.2 along with a discussion of the global model, which is used to provide context. The second purpose is to demonstrate the validity of the model as compared with the global model (when operated at similar resolution) and with the available

surface weather station data. The comparison with the global model is discussed in Section 3.3, and that with the surface meteorological observations in Section 3.4. In the latter case, simulations executed with resolutions of a few tens of kilometers can explain most of the diurnal variability of temperature, pressure, and winds at the landing sites. Finally, in Section 3.5 a summary is provided.

3.2 Model Descriptions

3.2.1 Mars MM5

The basis of the model used is the fifth-generation (version 3) PSU/NCAR Mesoscale Model (MM5), which was adapted for Mars. The original version of the model is described by *Anthes and Warner* [1978] and the current version is described by *Dudhia* [1993]. The model is nonhydrostatic and uses time split-explicit integration. The model uses an Arakawa "B" grid, where temperature and pressure are calculated at grid points at the center of a box, and the winds are calculated at the corners of the box. The model also uses terrain-following sigma-coordinates, with an upper boundary set by the user. Currently a top at the 5 Pa pressure surface (~50 km) is used. The model allows for arbitrary domain specification (using 3 different map projections) and for multiple domain nesting, which creates higher-resolution areas within the coarser grid. These higher-resolution domains can be nested one within each other up to a maximum of 4 times.

The initial and boundary conditions are provided by the Geophysical Fluid Dynamics Laboratory (GFDL) Mars General Circulation Model (GCM), described in Section 3.2.2. The details of the coupling are described in Section 3.2.3. The upper boundary condition is a constant pressure surface, with no air exchange across the surface.

Conversion of the model to Mars involved three different types of modification. First, structural changes within the model related to the time integration of the various forcing

functions were made. These included the planetary rotation and orbital revolution periods and modification of the model's definition of a "day" and a "year." The model's orbital code, which generates the daily and seasonal cycles of solar insolation, was also changed. Second, various constants within the model, such as the planetary radius, the Coriolis parameter, the gravitational constant, the gas constant of the atmosphere, and the solar constant. Third, the whole scale replacement of parameterizations for physical processes, which are significantly different on Mars, such as radiation, the surface and subsurface heat balance model, the CO_2 cycle, the water cycle, and the dust cycle. In all cases the Mars-specific parameterizations are taken directly from the version of the Geophysical Fluid Dynamics Laboratory (GFDL) Mars General Circulation Model (GCM) described by *Wilson and Hamilton* [1996].

The model includes the radiation scheme used in the *Wilson and Hamilton* [1996] version of the Geophysical Fluid Dynamics Laboratory (GFDL) Mars General Circulation Model (GCM). This radiation scheme treats solar absorption by CO_2 gas using a parameterized band model [*Burk*, 1976] and by atmospheric dust using a two-stream model [*Briegleb*, 1992]. The optical depth used in the radiation code is derived from dust tracers of two particle sizes that are advected and diffused by the model dynamics. In the infrared, radiative heating due to CO_2 is treated using the band model of *Hourdin* [1992]. For dust the infrared scheme developed by *Haberle et al.* [1982] is used, and again the optical depths derived from the model dust tracers are used. The optical properties for dust are the same as used in *Wilson and Hamilton* [1996].

The surface models used were topography derived from the Mars Orbiter Laser Altimeter (MOLA); albedo maps of the equatorial regions are from *Pleskot and Miner* [1981] and of the polar regions from *Paige et al.* [1994] and *Paige and Keegan* [1994]; and ground thermal inertia maps of the equatorial region from *Palluconi and Kieffer* [1981] (as modified by *Haberle and Jakosky* [1991]) and of the polar regions from *Vasavada et al.* [2000]. The ground temperature calculation scheme uses a 12-layer subsurface heat diffusion model

that captures the annual and seasonal temperature waves by simulating the uppermost 2 m of the subsurface. The subsurface layer temperatures are initialized from the GCM input, and are implicitly integrated (as implemented in the GCM [*Wilson and Hamilton*, 1996]).

The model has been modified to handle the presence of interactive tracers, such as dust particles, which are used in the radiation scheme. Two dust particle sizes are currently used as described in *Wilson and Hamilton* [1996], although this will be expanded to a greater number in the future. The water cycle is also simulated in the model, including water vapor transport, atmospheric ice formation, transport, and precipitation, and the formation of surface ice deposits. These processes are taken from *Richardson* [1999] and used in place of the various hydrological cycle parameterizations included in the terrestrial version of the MM5. In the case of transport of dust, water vapor, and water ice, the tracer transport dynamics built into the MM5 were used unmodified.

The MM5 boundary layer option employed in simulations is the Medium Range Forecast (MRF) scheme, based on the one used in the National Center for Environmental Prediction (NCEP) Medium Range Forecast (MRF) model. It is described by *Hong and Pan* [1996] and is based on the formulation by *Troen and Mahrt* [1986]. This parameterization of the boundary layer is only modified by the coupling to the calculation of surface temperatures and heat fluxes determined by the Mars subsurface model.

3.2.2 GCM Description

The mesoscale model requires a description of both initial and boundary conditions. As implemented in this study, the mesoscale model is driven by boundary conditions which evolve with a two-hour time step. These initial and boundary conditions are derived from the Geophysical Fluid Dynamics Laboratory (GFDL) Mars General Circulation Model (GCM) [*Wilson and Hamilton*, 1996]. Compatibility between the Mars MM5 and the GFDL Mars GCM is maximized by the use of common physical parameterizations in both

models. These include the treatment of radiation, dust injection, surface and subsurface heat balance and diffusion, planetary orbit, and condensation/sublimation of CO_2, including the treatment of surficial CO_2 ice. These schemes have been described in Section 3.2.1 and their description is not repeated here. Additionally, the Mars MM5 includes a full water cycle, which is again based on that in the GFDL Mars GCM [*Richardson*, 1999]. As water is not considered in this study, description of water processes is deferred to a later paper.

The GFDL Mars GCM differs from the Mars MM5 in treatment of large-scale dynamics, subgrid-scale diffusion, and the planetary boundary layer. The most obvious difference in the treatment of large scale dynamics is the use of the primitive equations in the GCM, which filters out vertically propagating sound waves by employing a hydrostatic approximation for the vertical momentum equation. In addition, purely horizontally propagating sound waves (Lamb waves) are filtered out by setting vertical velocity to 0 at the surface. The GCM also treats Coriolis acceleration as a purely horizontal process (producing horizontal accelerations due to horizontal winds). These approximations are based on the small values of vertical acceleration on large scales, and on the negligible heat and momentum transports due to sound waves on large scales. Another difference is the model grid structure. The GCM calculates all variables at the same horizontal grid point (this is the Arakawa "A" grid, as opposed to the "B" grid used in the MM5 [*Arakawa and Lamb*, 1977]), and employs a mixed sigma/pressure vertical structure, such that the vertical coordinate is terrain-following in the lower domain, and is a constant pressure surface in the upper portion. The GCM domain extends up to approximately 85 km in order to fully capture the southern summer Hadley circulation [*Wilson*, 1997]. Subgrid-scale mixing away from the surface layer is treated in the vertical as a diffusive processes acting on heat and momentum with a Richardson number-dependent coefficient. The scheme is described in *Hamilton et al.* [1995]. In the horizontal, mixing is dependent on the flow curvature, as described by *Andrews et al.* [1983]. No explicit treatment of the boundary layer is included

above the surface layer beyond that which results naturally from the diffusion schemes. The surface layer is treated with a drag coefficient scheme which is based on Monin-Obuhkov theory, in which the fluxes of momentum and heat at the surface depend upon the total wind speed, the Richardson number, the height of the lowest model level, and the roughness length [*Wilson and Hamilton*, 1996].

3.2.3 Coupling of the Mars MM5 with the GCM

The Mars MM5 is a limited area model. As such, it needs boundary and initial conditions to integrate the equations of motion, energy, and mass. These are provided by the GFDL Mars GCM (as described above) through a series of "preprocessing" steps. For the simulations discussed in this paper, two- and three-dimensional fields from the GCM were extracted at two-hour intervals. These fields included the three-dimensional winds, temperature (both air and subsurface), pressure, water vapor amount, dust amount for both particle sizes. The two-dimensional fields include surface ice (water and CO_2) amount, surface temperature, and surface pressure. All of the above-mentioned variables are used for initial conditions; only the three-dimensional fields are necessary for boundary conditions.

"Preprocessing" consists of three steps. The first is interpolating the GCM output to constant pressure levels. Then this output is trimmed to the horizontal extent of the mesoscale model domain to be used, and the coarser GCM output is interpolated to the higher-resolution mesoscale model grid points. The vertical coordinate used in the mesoscale model is the terrain-following sigma coordinate [e.g., *Jacobson*, 1999]. The vertical levels to be used in a given simulation are chosen at this point. Vertical interpolation from the constant pressure levels to these sigma levels is then done. Sufficient boundary conditions must be generated for the entire mesoscale model simulation at this preprocessing stage. For the GCM comparison simulations, this was done for 10 days, while for the lander comparison simulations, the amount of time chosen was five days. Since the model does not

start from rest (e.g., no winds and an isothermal temperature structure) there is no "spin-up" time necessary. However, experience shows that the first day of integration is affected by adjustment from the initial conditions to a balanced higher-resolution simulation. This time scale is roughly consistent with the radiative time scale of the Martian atmosphere.

It should be noted that tracers, such as dust and water vapor, are passed into and out of the model domain via the boundary conditions. In addition, surface sources of these materials exist. The same applies to the total air mass within the model domain. The ability to transport air across the boundaries (i.e., allowing for a net divergent wind) allows the simulation of tidal propagation, and sublimation from or condensation onto the polar caps.

3.3 Comparison with the Mars GCM

As a first test of the Mars MM5, a comparison with the GFDL Mars GCM on similar length scales was performed. The GCM has a horizontal resolution of 5 degrees in latitude and 6 degrees in longitude with the lowest layer being roughly 400 m in thickness. The GCM has 20 vertical levels between the surface and roughly 85 km. The Mars MM5 was thus run with a horizontal resolution of 5 degrees in both latitude and longitude (the MM5 grid boxes are constrained to be square). As the Mars MM5 cannot be run in a truly global mode, it was attempted to make as large a domain as possible. In this case, the model domain extends a full 360° in longitude, although there is no connection between the easternmost and westernmost extreme grid points, i.e. the model does not wraparound at the edges. These edges are fed by boundary conditions from the GCM. The latitudinal extent of the mesoscale domain ranges from 60° S to 60° N. Eight vertical levels were used in the Mars MM5 simulation from the surface to roughly 40 km, with a lowest layer thickness equivalent to that of the GCM.

The Mars MM5 was initialized with output from the GFDL Mars GCM. After a ten

day integration, the drift between the two models was examined. There are a number of potential reasons why the two models may differ in their simulation of the circulation. These include: difference in grids (Arakawa "A" grid and rectangular boxes in the GCM, and Arakawa "B" grid and square boxes in the Mars MM5), differences in boundary layer schemes, subtle differences in numerical integration method, and the treatment of the atmosphere as hydrostatic in the GCM and as non-hydrostatic in the Mars MM5. However, the numerical framework should not significantly influence the simulation of the circulation of the atmosphere if it is an accurate model. Thus, differences between the GCM and Mars MM5 should be small and their comparison provides one way of testing the validity of the Mars MM5. Thankfully, the agreement between the two models is quite good and generally traceable to subtle differences in the strength of the Hadley cell flow between the two models.

Two comparisons between the GCM and the Mars MM5 at two dates were conducted: L_s 180 (equinoctial period) and L_s 270 (solstitial period). Figures 3.1 and 3.3 show output from the GCM and Mars MM5 as well as their differences for the L_s 180 and L_s 270 comparisons respectively. Temperature and winds are from the surface model layer, approximately 400 m in thickness. Figures 3.2 and 3.4 show latitude and height dependent output for the same simulations as zonal averages. Temperature, zonal wind, meridional wind, and vertical wind are shown.

3.3.1 Equinox

The near-surface air temperatures displayed in Figures 3.1A and 3.1B generally agree to within 5 K between the two models. This level of agreement is gratifying given the over 60 K amplitude of the diurnal cycle and nearly 100 K pole-to-equator temperature contrast. The largest differences are over the Tharsis region and near the cap edge. The latter are mostly due to slight differences in representation of the location of the cap edge, related

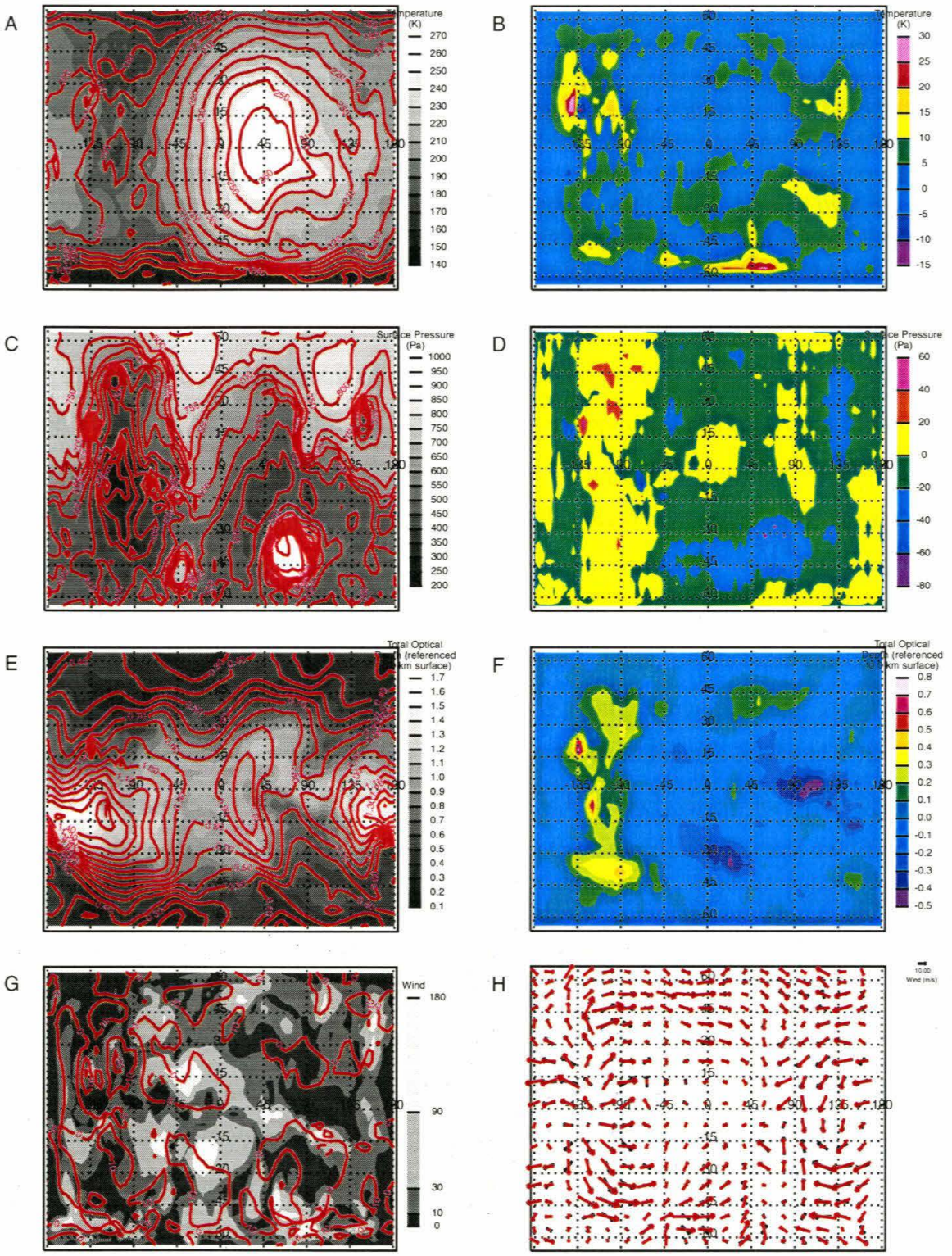
A
Temperature (K)
270
260
250
240
230
220
210
200
190
180
170
160
150
140
B
Temperature (K)
30
25
20
15
10
5
0
-5
-10
-15
C
Surface Pressure (Pa)
1000
950
900
850
800
750
700
650
600
550
500
450
400
350
300
250
200
D
Surface Pressure (Pa)
60
40
20
0
-20
-40
-60
-80
E
Total Optical
(referenced
km surface)
1.7
1.6
1.5
1.4
1.3
1.2
1.1
1.0
0.9
0.8
0.7
0.6
0.5
0.4
0.3
0.2
0.1
F
Total Optical
(referenced
km surface)
0.8
0.7
0.6
0.5
0.4
0.3
0.2
0.1
0.0
-0.1
-0.2
-0.3
-0.4
-0.5
G
Wind
180
90
30
10
0
H
10.00
Wind (m/s)

Figure 3.1: [p. 40] Map projections of model output for various variables at L_s 180. For the upper 6 plots, the left-hand column is GCM and Mars MM5 output plotted on top of each other, with the GCM output in the background as a gray shading and the Mars MM5 over-plotted as contours. The right-hand column is the difference of the output, Mars MM5 output minus GCM output. **A & B:** Temperature. **C & D:** Surface pressure. **E & F:** Total optical depth (referenced to the 0 km surface). **G:** The absolute difference in wind direction, in degrees, is plotted in the background as a gray shading, with ranges labeled by the scale bar at the right. The red contours represent the difference in wind speed between the two models (Mars MM5 minus GCM). **H:** Wind vectors for the GCM (plotted in black) and the Mars MM5 (plotted in red). Scale bar for wind speed is at the upper right of the figure.

to the difference in the placement of grid points between the two models. The circulation around Tharsis is inherently difficult to simulate on synoptic scales (hundreds of kilometers) due to the large variability of and large gradients in topography on these scales. Thus, small differences in simulating the circulation over this region between the two models is not particularly surprising.

Differences in surface pressure are rather small, within ± 20 Pa over most of the globe. Largest differences occur over regions of large topography (i.e., Hellas basin and Tharsis), which again is likely related to the difference in grid point positioning along topographic gradients. The modeled surface pressure outputs are shown in Figures 3.1C and 3.1D.

The distribution of dust is the most difficult field to accurately simulate. This is because the distribution of dust is both sensitively dependent upon the circulation and modifies the distribution of radiative heating, which in turn modifies the circulation. Thus this field provides a very sensitive test of the coupled radiative-dynamical behavior of the two models. Figures 3.1E and 3.1F show the modeled optical depth normalized to the 0 km reference surface. As discussed in Section 3.2, dust is passed into the mesoscale model domain by the boundary conditions and is also injected from the surface within the mesoscale model domain using a surface/air temperature contrast criterion. Agreement is to within ± 0.2 for roughly three quarters of the modeled domain, and the biggest differences occur in the regions where the gradient in optical depth is largest. Generally the GCM has more dust, and

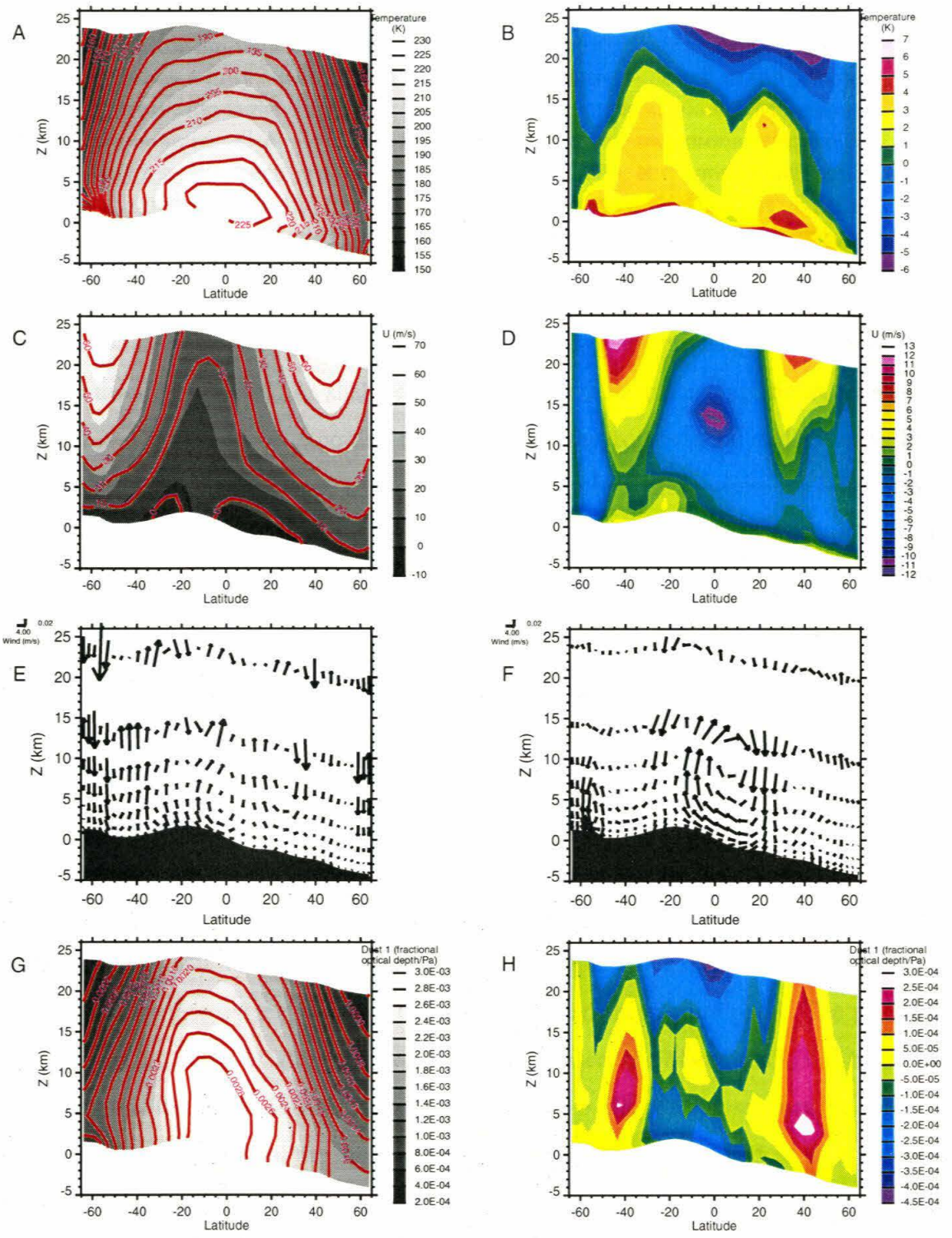
A
B
C
D
E
F
G
H
Z (km)
Latitude
Temperature (K)
U (m/s)
Wind (m/s)
Dust 1 (fractional optical depth/Pa)

Figure 3.2: [p. 42] Zonal averages of model output, plotted as latitude versus height, for L_s 180. Except for the wind vector figures, the left-hand column represents GCM data in the background as a gray shading with Mars MM5 data over-plotted in red contours, and the right-hand column is the difference between the two models, Mars MM5 minus GCM. **A & B:** Temperature. **C & D:** Zonal wind. **E & F:** Mean meridional circulation. The vertical velocities have been exaggerated by a factor of 200, and appropriate vector scale bars are at the upper left of the figures. **E:** GCM. **F:** Mars MM5. **G & H:** Dust amount. The units of dust used here are fractional optical depth over the grid box horizontal area per unit thickness of the grid box in pressure.

it is more equatorially confined. The Mars MM5 has a slightly smoother distribution with more dust towards the poles. As shall be discussed when the zonal average fields are examined, the Mars MM5 may be exporting more dust from the tropics to the midlatitudes. The most significant discrepancies are along the western edge of Tharsis, where the Mars MM5 has temperatures and surface pressures larger than the GCM. The larger dust amounts in this region result from a more active boundary layer driven by the higher temperatures and from the ability of the atmosphere to hold more dust due to the higher pressure.

The synoptic scale flow patterns are similar in the two models as shown in Figures 3.1G and 3.1H. The surface wind patterns in both models (Fig. 3.1H) are dominated by the tidal flow as modified by topography, with convergence lagging the daily temperature maxima and divergence roughly 180° out of phase. The largest differences occur again at the regions of large topography, Hellas basin and Tharsis. On the whole directional agreement between the mesoscale model and the GCM is within 30° and agreement in speed is within 10 m/s.

Figures 3.2A and 3.2B show the zonal average temperatures for the two models. As with the near-surface air temperature, the general agreement is quite good. The primary difference occurs at the upper levels over the equator. Here the Mars MM5 is as much as 6 K cooler than the GCM. Examining Figures 3.2G and 3.2H, one can see that the amount of dust at the upper levels of the model domain are less in the Mars MM5 as compared to the GCM. Thus the primary explanation for the large temperature differences at high levels is due to differences in solar heating due to absorption by dust.

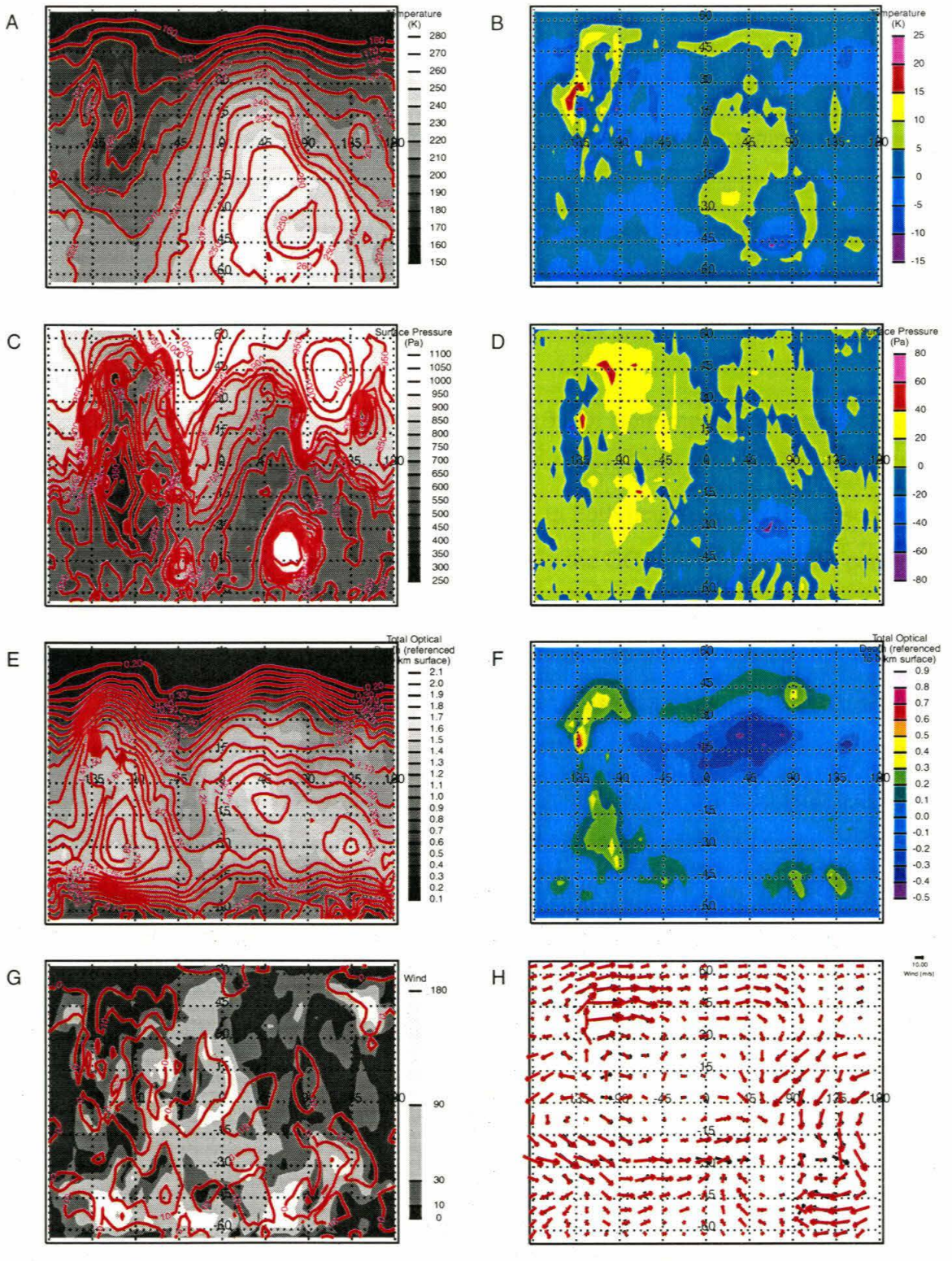
A
Temperature (K)
280
270
260
250
240
230
220
210
200
190
180
170
160
150
B
Temperature (K)
25
20
15
10
5
0
-5
-10
-15
C
Surface Pressure (Pa)
1100
1050
1000
950
900
850
800
750
700
650
600
550
500
450
400
350
300
250
D
Surface Pressure (Pa)
80
60
40
20
0
-20
-40
-60
-80
E
Total Optical
(referenced
km surface)
2.1
2.0
1.9
1.8
1.7
1.6
1.5
1.4
1.3
1.2
1.1
1.0
0.9
0.8
0.7
0.6
0.5
0.4
0.3
0.2
0.1
F
Total Optical
(referenced
km surface)
0.9
0.8
0.7
0.6
0.5
0.4
0.3
0.2
0.1
0.0
-0.1
-0.2
-0.3
-0.4
-0.5
G
Wind
180
90
30
10
0
H
10.00
Wind (m/s)

Figure 3.3: [p. 44] Same as Figure 3.1, except for L_s 270.

Referring back to Figure 3.2B, a less than 5 K temperature warming at midlatitudes from the surface to roughly 15 km is found. The existence of these temperature deviations results from two factors. One, the presence (see Figure 3.2F) of a more confined and stronger lower level Hadley circulation (as compared to the GCM) results in adiabatic descent and warming at the midlatitudes. Two, as mentioned in the optical depth discussion, the existence of more dust in the Mars MM5 at mid and high latitudes results in direct radiative heating.

The zonal winds are shown in Figures 3.2C and 3.2D. Both models maintain a strong polar jet, and only small differences in the width of the jets yield differences ($\leq$ 15%) in zonal wind speed. The Mars MM5 has broader jets in both hemispheres. In the southern hemisphere, the jet is weaker in the Mars MM5 than in the GCM. However, in the northern hemisphere the jet in the Mars MM5 is both broader and stronger. The increased width of the jets suggest a somewhat stronger meridional momentum mixing process in the Mars MM5. This mixing near the model top appears to be associated with the proximity of the rigid (though free-slip) lid. Note that the Mars MM5 model top is significantly lower than that of the GCM (40 km vs. 85 km). When the simulation is repeated with a domain of higher vertical extent, the widths of the Mars MM5 jets are observed to decrease (not shown). In fact, in this case, the jets become slightly more confined than in the GCM.

Figures 3.2C and 3.2D also show a zonal wind deficit in the Mars MM5 at midlevels (approximately 15 km) over the equator. The occurrence of this deceleration of the westerlies (by up to 10 m/s) is consistent with the vertical transport and deposition of momentum by a shallower upwelling branch of the Hadley cell.

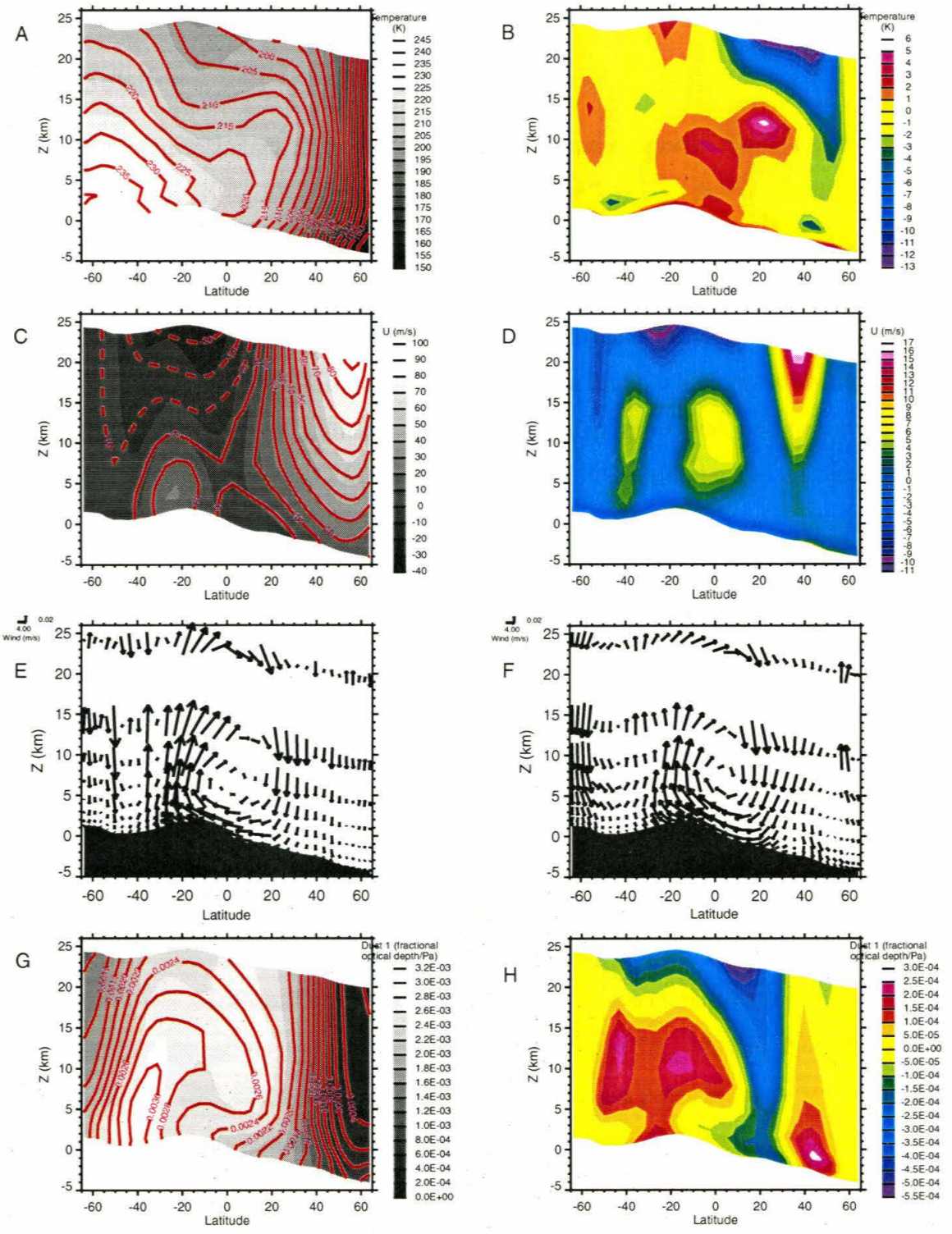
A
B
C
D
E
F
G
H
Z (km)
Latitude
Temperature (K)
U (m/s)
Wind (m/s)
Dust 1 (fractional optical depth/Pa)

Figure 3.4: [p. 46] Same as Figure 3.2, except for L_s 270.

3.3.2 Solstice

Most of the comments made about the surface and column integrated characteristics of the fields at equinox apply equally well at the solstice (Figure 3.3), e.g., the surface temperature and pressure differences between the models. A slight difference from equinox is in Arabia Terra, where the Mars MM5 shows more dust at the northern edge of this area and less dust in the interior. The excess dust on the northern edge of Arabia Terra occurs at the location of greatest gradient in optical depth at the edge of polar night, which probably represents a slight difference in the latitudinal location of the polar vortex wall and hence a slight poleward expansion of the dusty extra-tropical airmass. The difference in dust amount in the interior region of Arabia Terra appears to be due to the inability of the Hadley cell circulation to deliver dust to this northern subtropical region, as discussed below.

The solstice mean meridional circulation (Figure 3.4) is dominated by a much stronger and latitudinally more extensive Hadley cell than during equinox, but the circulation is still more confined in the Mars MM5 as compared to the GCM, due to the presence of a rigid lid. Examples of this can be seen in the mean meridional circulation (Figure 3.4E and 3.4F), where the upwelling at about 20° S is weaker in the Mars MM5, especially at the top layer. This is also reflected in the zonal average temperature pattern where there are higher temperatures in the upwelling branch of the Mars MM5 due to decreased adiabatic cooling, and cooler temperatures at upper levels in the descending branch. However, the signal is most clear in the meridional transport of dust, where dust accumulates in the upwelling branch and is depleted relative to the GCM in the downwelling branch. Note the small excess at high north latitudes and low levels due to a slight poleward flow at low levels, which accumulates the dust that does make it down the downwelling branch.

As seen in Figure 3.4C and 3.4D, the polar jet is wider in the Mars MM5 as compared to the GCM for the same reasons discussed in the equinox case. The westerly excess at

mid-levels over the equator as compared to the GCM now results from weaker upward momentum transport in contrast to the equinoctial case.

In summary, after 10 days of integration, the level of agreement is pleasing. The minor differences that do exist are easily explained by the intrinsic design of the mesoscale model as a limited area model (in the horizontal and vertical), leading to a more confined Hadley circulation. This is not a major difficulty, so long as these factors are borne in mind when designing numerical experiments with the model. Most of the studies to be undertaken with the model will relate to near-surface flow phenomena. Within this region of the atmosphere, the circulation is dominated by the surface and by tidal flow, and thus the details of the upper level Hadley flow are less important [*Wilson and Hamilton*, 1996; *Joshi et al.*, 1997]. However, in cases where deeper atmospheric circulation phenomena are to be studied (e.g., modeling the polar vortex), attention must be paid to creating a model domain with sufficient depth.

3.4 Model Validation Against Meteorological Stations

As a further test of the validity of the model, simulations were performed to compare the Mars MM5 model output with meteorological observations from the near-surface of Mars. These data are provided by the meteorological instruments on the three successful landers on Mars: Mars Pathfinder, Viking Lander 1, and Viking Lander 2. These comparisons take advantage of the particular strengths of the mesoscale model, allowing for simulations using high vertical and horizontal resolution.

Simulations were performed at one specific time of year at each landing site. The Mars Pathfinder and Viking Lander 1 simulations were performed during northern summer (L_s 147 and L_s 111, respectively), while Viking Lander 2 simulations were carried out during both the northern summer (L_s 130) and, for a more stringent test of the model, the northern winter period (L_s 334). All of the simulations were designed with the same grid

point structure, a 31 by 31 grid with 18 vertical levels. The horizontal resolution was 1/16 of a degree (approximately 4 km) in the horizontal, resulting in a square domain of length 120 km to a side (roughly 2°). The lowest vertical layer had a thickness of approximately 4 m, allowing for direct comparison with height of the meteorological instruments without having to scale for height. As noted in Section 3.2, in contrast to the GCM, the mesoscale model is not "spun-up" from rest. Consequently, the adjustment period is roughly the one day that is required for the slight relaxation from the initial conditions that were generated from the low-resolution GCM output. Integrations were performed for five days, and two-day averages of the mesoscale and GCM model output were compared with two-day averages of the lander observations. The averaging was undertaken to reduce the effect of day-to-day variability associated with "weather." Such weather was particularly severe in both the model output and the data at the Viking Lander 2 site during winter. For each of the landing sites, one or more further simulations were performed varying a parameter to determine that parameter's effect on the simulation. The results of these tests, as well as the standard cases, will be described below.

For each landing site, a subset of the meteorological variables pressure, temperature, and wind velocity (speed and direction) will be compared with model output. Different landing sites, during different periods, have different availability of these variables. In all cases, the output from the Mars MM5 simulations are the data from the lowest layer, approximately 2 m from the surface.

3.4.1 Mars Pathfinder Site

Choice of the period of simulation of the Pathfinder site was heavily constrained by the short length of the mission. A period early on during the mission (the second week) was chosen since a full 24 hours of data (pressure, temperature and wind direction) were collected. A deficiency of the dataset, in comparison with the Viking Lander datasets, is the

lack of retrieval of wind speeds from the wind sensors. However, in terms of temporal resolution and precision, the quality of the other Pathfinder relative to the Viking Lander data is higher.

In varying the amount of dust in the lander simulations, uniform dust amounts were used, and not the interactive dust used in the GCM comparisons and described above, since the domain is so small that the total amount of dust is essentially uniform. In all cases, the optical depth at each location determined from the use of interactive dust is essentially the same as the "best" uniform optical depth chosen for that location and time.

Figure 3.5 shows the data and modeled surface pressures for a 24-hour time series. The fit is exceptionally good, as gauged by the magnitude and phase of the diurnal and semi-diurnal tidal components. Errors, especially in the phase, appear at higher frequencies where the amplitude is close to zero. Also shown in this figure is the pressure as simulated by the GCM. It is important to note that the Mars MM5 does not significantly modify the tide as driven by the GCM. Given that the tides are a global wave system, it is not surprising that simulation of a very small domain at high resolution does not significantly alter the surface pressure response. It is, however, encouraging that the Mars MM5 is so readily able to propagate the GCM global tidal system through the model domain.

Air temperature is the variable in the Mars MM5 most sensitive to optical depth amount. Shown in Figure 3.6 is the data and model output for a variety of optical depth cases. Using the spacecraft-derived thermal inertia and albedo values, the model is able to generate a diurnal cycle of temperature to within 5 K for the best case (τ is between 0.5 and 1.0). The total range of observed temperatures is about 60 K. Nighttime temperatures are consistently underpredicted by about 5 K. This may be due to errors in the thermal inertia (but see below), or in the parameterization of the subsurface heat diffusion. An inability to capture the nighttime lowest temperatures and the timing of post-dawn increase in temperatures has been noted before in a 1-D planetary boundary layer model by *Wilson and Joshi* [1999]. The daytime temperatures can be fit by varying the optical depth, but the observed temper-

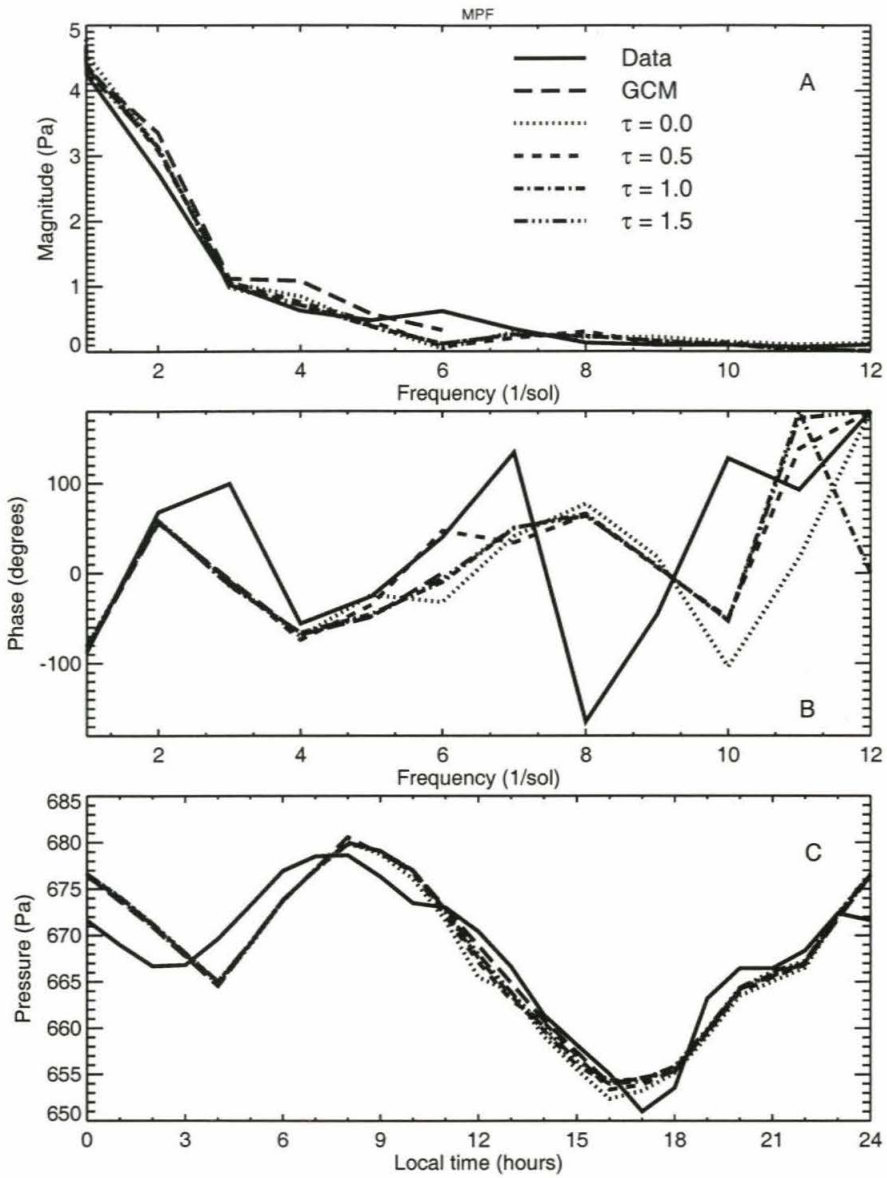

Figure 3.5: Comparison of pressure at the Mars Pathfinder site. **A:** Amplitude of the diurnal, semi-diurnal, and higher order terms of the pressure as a function of frequency in 1/sol, where 1 sol is one Martian day. Amplitudes were obtained by taking the Fourier transform of the output from the model simulations (both GCM and Mars MM5) and of the lander measurements. Lander measurements come from sol 9 of the Pathfinder mission, approximately L_s 147. **B:** Same as **A** except the phase is plotted. **C:** Plot of the diurnal cycle of pressure of the model simulations and the data as a function of local time in Martian hours, where 1 Martian hour is 1/24 of a Martian day.

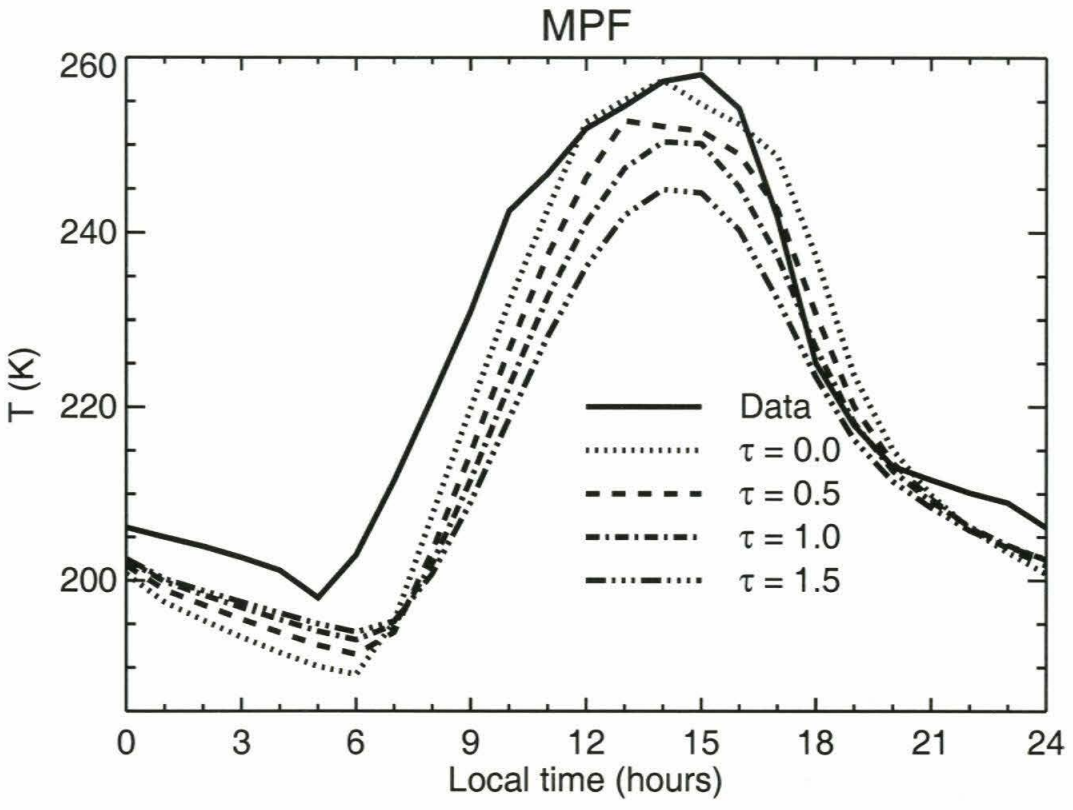

Figure 3.6: Diurnal temperature cycle comparison at the Mars Pathfinder site. Temperature of the air at approximately 2 m from the surface is plotted versus local time in Martian hours. Data is from sol 9 of the Pathfinder mission, approximately L_s 146.

ature maximum is only attained with the absence of dust. The best fit is with the $\tau = 0.5$ to 1.0 cases because of the fit to the total range of temperature with the view that the model cycle is simply shifted colder by 5 K.

In order to examine the effects of albedo and thermal inertia on the diurnal temperature cycle, three more simulations were run by modifying the best fit case. The values of thermal inertia and albedo in a 10 km by 10 km box (9 out of the 961 total grid points) centered on the landing site were varied. In one case, the albedo was reduced to half its value, in the second thermal inertia was decreased to one-fourth its original value, and in the third both changes were made. These results are shown in Figure 3.7. Unsurprisingly, changing the

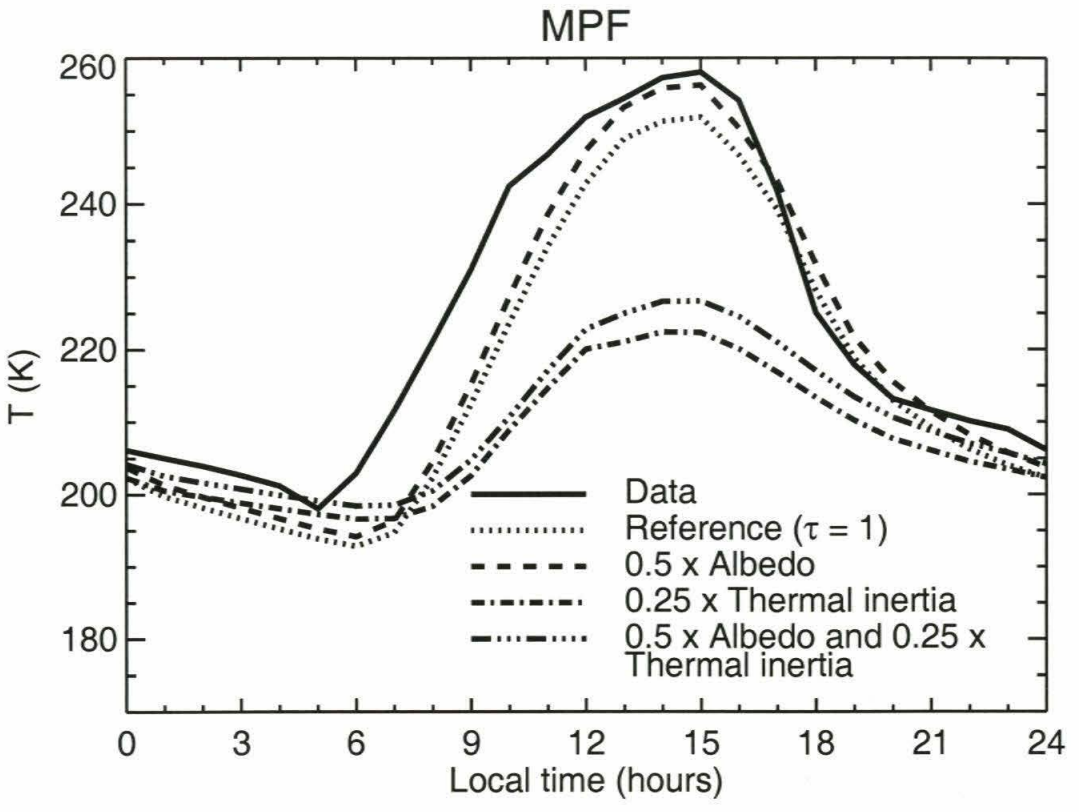

Figure 3.7: Diurnal temperature cycle comparison at the Mars Pathfinder site. Data is compared with the reference case using an optical depth of 1.0. The reference case is then modified in a 3 point by 3 point box in the domain around the landing site. First the albedo is reduced by half, then the thermal inertia is reduced to a quarter of its original value, and then the third case is a combination of the first two.

albedo has very little effect on nighttime temperatures. The effect is primarily to change daytime maximum temperatures. Changing thermal inertia does in fact change nighttime temperatures, i.e., a decrease in thermal inertia produces a temperature increase. And indeed the nighttime minimum temperature from the data is matched. However, daytime temperatures are drastically reduced. Decreasing the albedo does not make up for this drop in daytime peak temperatures. Probably equally importantly, the increase in temperatures after dawn is delayed by over an hour. This only exacerbates the pre-existing mismatch in the best case, where the post-dawn daytime increase in temperature is already late by about

one hour. These results tend to rule out the effect of thermal inertia and albedo in the misfit to measured data. It thus appears more likely that either a slope effect exists or that there are slight errors in the parameterization of either subsurface or boundary layer heat diffusion. A sloping surface changes the amount of radiation absorbed at a given local time, and thus an eastward sloping surface at the Pathfinder site would tend to have an earlier rise in surface temperatures, and hence near-surface air temperature. The Pathfinder site does indeed have an eastward slope [*Kirk et al.*, 1999].

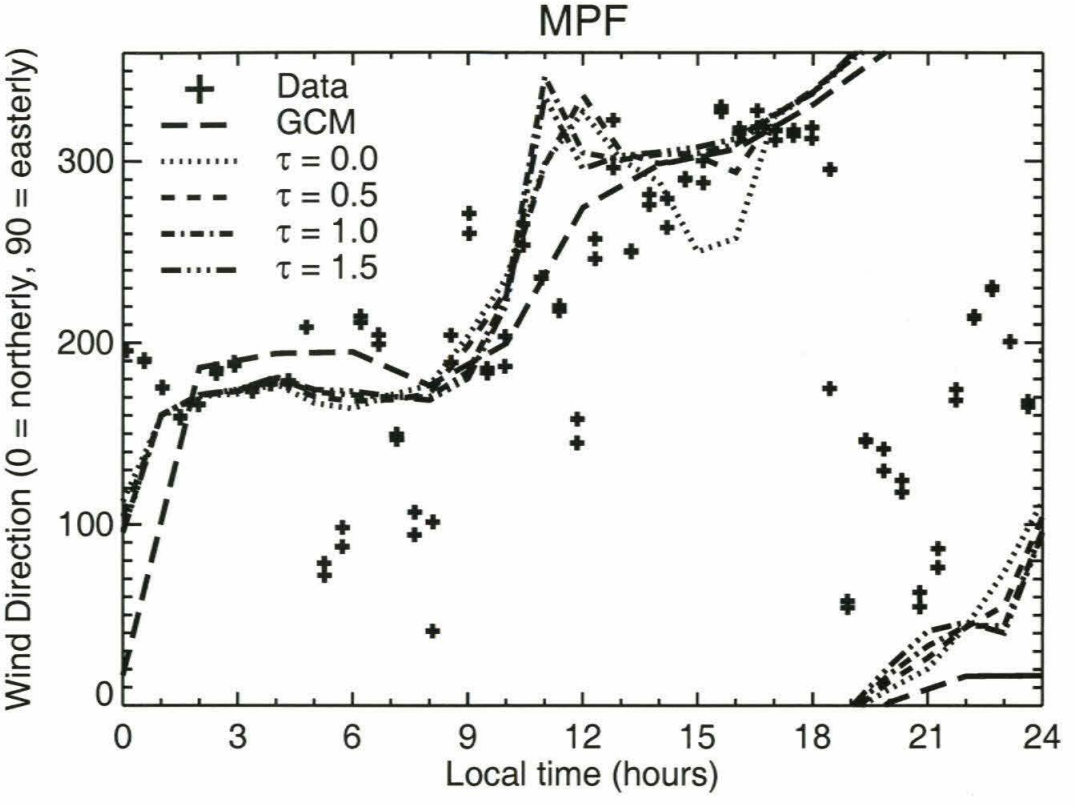

Figure 3.8: Wind directions at the Mars Pathfinder site. Data measured by the lander on sol 9 are plotted as crosses, and the output from the GCM and the various Mars MM5 simulations are plotted as lines. Direction is defined as 0 for a northerly (toward the south) wind, 90 for easterly, 180 for westerly, and 270 for southerly winds. Model output winds are for a height approximately 2 m from the surface

Observed and simulated wind direction data are shown in Figure 3.8. A single day's

worth of lander observations are shown, but agree with longer baseline averages shown in *Schofield et al.* [1997]. Data for the various opacity cases and the GCM are also shown. Fits in all cases are quite good. Note that there is very little variation either among the different opacity cases or between the GCM and the Mars MM5. This suggests that the global tidal patterns and/or wind patterns generated by slopes resolvable by the GCM are more important in determining the wind directions than local slope effects resolvable only by the mesoscale model. This subject will be returned to when considering the other lander sites.

3.4.2 Viking Lander 1 Site

The Viking Lander 1 meteorological data also extends only over a brief period. Thus the choice of season was limited. The Pathfinder data were limited to a late summer period, and so with the Viking Lander 1 data, a period as close to the summer solstice as possible was chosen to be examined. This turns out to be equivalent to looking at data as early in the Viking Lander 1 mission as possible. The chosen season was L_s 111.

The pressure data along with Mars MM5 output at various optical depths and the GCM output are shown in Figure 3.9. As with the Pathfinder site, the Mars MM5 pressure output follows the GCM output very closely. In this case, however, it would appear that the diurnal and semi-diurnal amplitudes are overpredicted. A significant difficulty in making this determination is that the Viking Lander 1 pressure data at this season are poorly resolved with some data gaps. Thus, concerns about the pressure data limited the ability to determine how well the data was matched. In choosing this period tradeoffs were made among the quality and availability of the various Viking Lander 1 measurements. Good quality in one variable tended not to be correlated with good quality in the others. The determining factor in choosing this period was the availability of good wind measurements, not pressure.

Near-surface air temperatures are plotted in Figure 3.10. The observations are shown

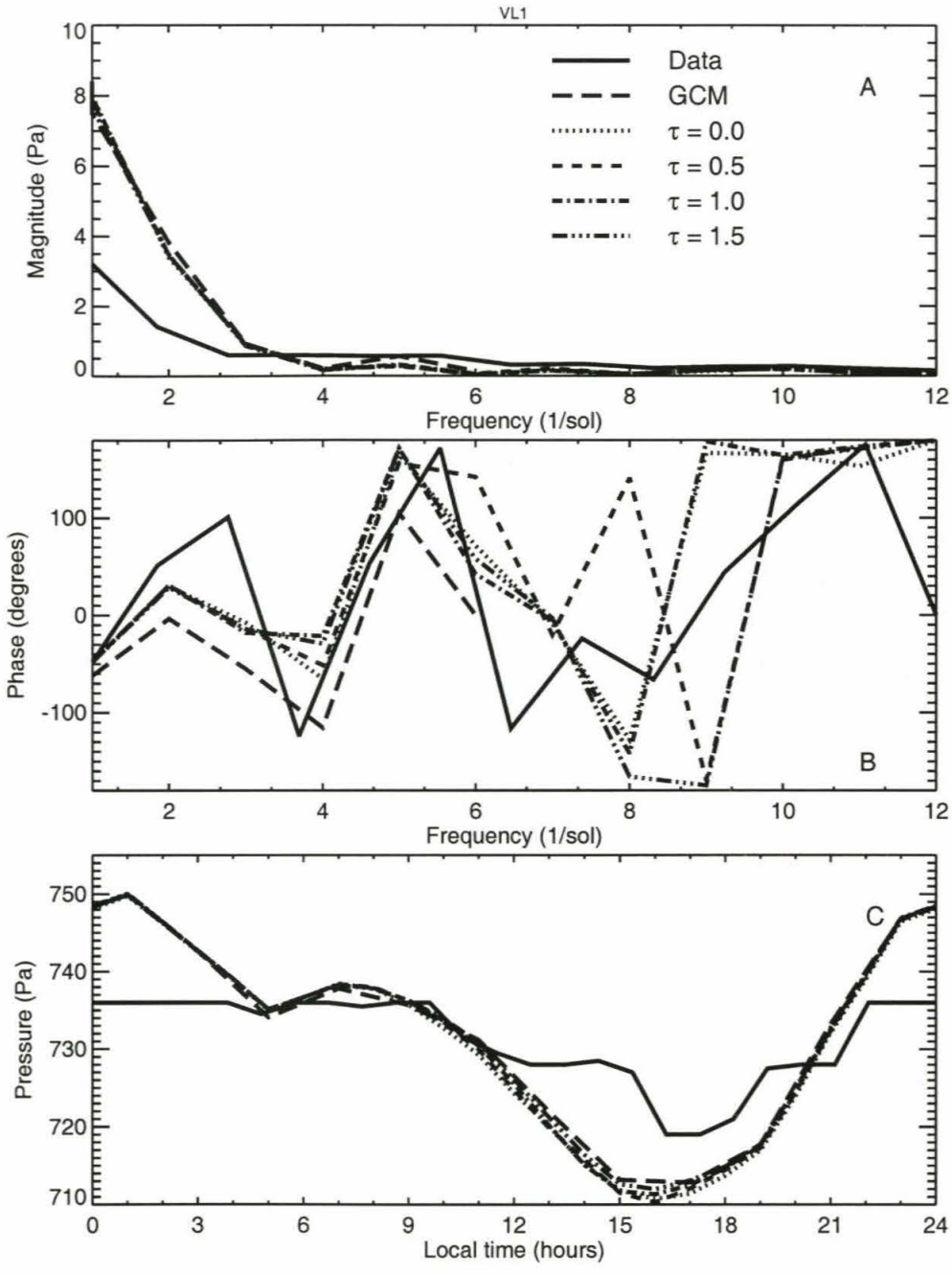

Figure 3.9: Same as Figure 3.5, except for the Viking Lander 1 site. Time of year is L_s 111.

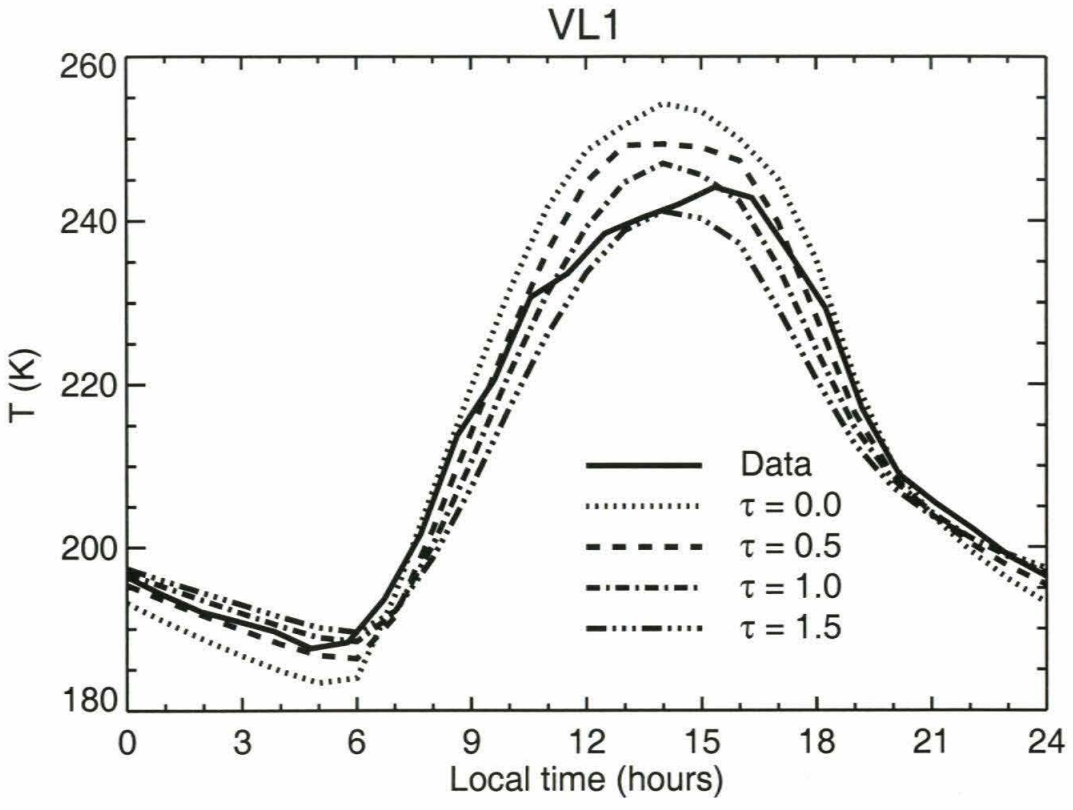

Figure 3.10: Same as Figure 3.6, except for the Viking Lander 1 site.

along with the Mars MM5 output for various optical depths. For most cases the fit is exceptionally good. In particular, the nighttime temperatures and the timing of increase in temperature (post-dawn) are captured in contrast to the Pathfinder simulations. The various optical depth cases serve to generate a spread in daytime peak temperatures, and the best fit appears to be about $\tau = 0.5$.

Wind directions for the Viking Lander 1 site are shown in Figure 3.11 including the lander data, the GCM and the Mars MM5 for the best fit dust case. All models agree pretty well with the data between 7 PM and 7 AM. In the daytime period the GCM exhibits a strong rotation between 11 AM and 1 PM which is at variance with the observations. The Mars MM5 is also at variance with observations although the pattern is less straightforward.

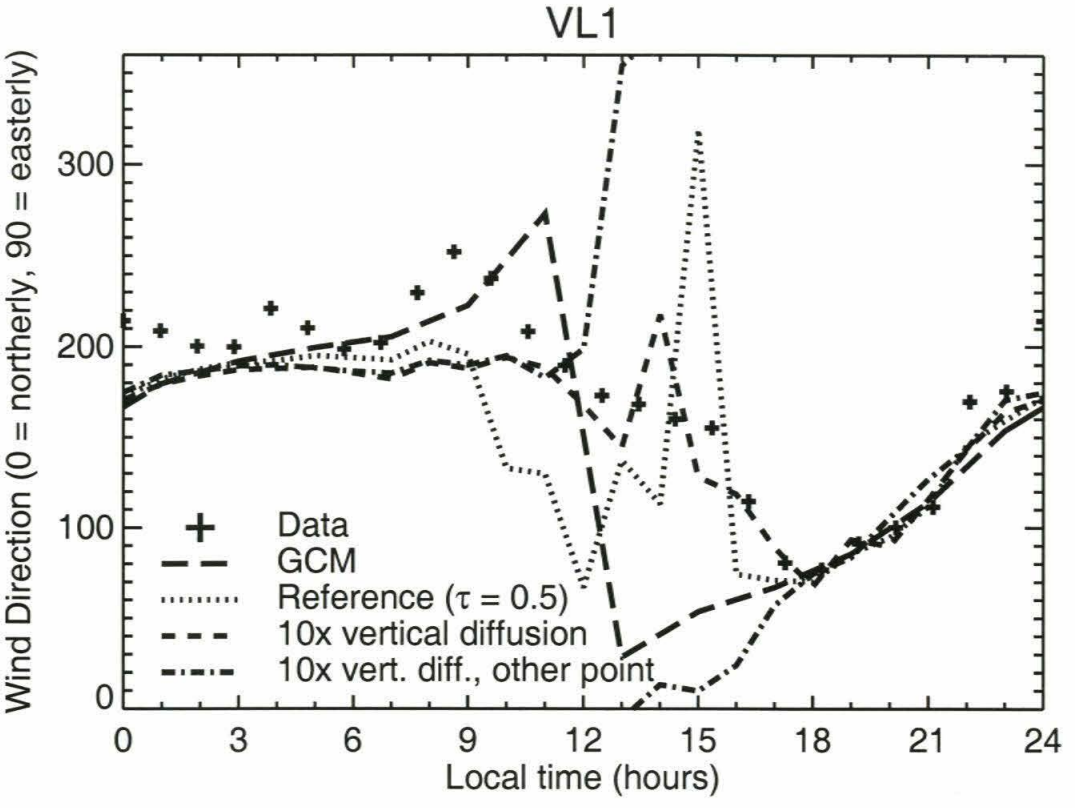

Figure 3.11: Same as Figure 3.8, except for the Viking Lander 1 site. The reference case is for an optical depth of 0.5, and the location of the other sample point is about 27 km to the northeast of the reported landing site.

The other dust scenarios are roughly equivalent to the best case in terms of being good fits at night, and having a similar amount of variability and lack of fit, although with a different trend, during the day.

The hodograph for the lander data and the best fit dust case are shown in Figure 3.12. The magnitudes of the wind are quite low compared to the lander data even at times when the model was correctly predicting direction. The problem of underprediction of wind speeds is common to all lander simulations that were undertaken (see also Section 3.4.3). To address this, the vertical structure of the wind as a function of local time was examined, as shown in Figure 3.13. This figure shows that the wind increases away from the surface

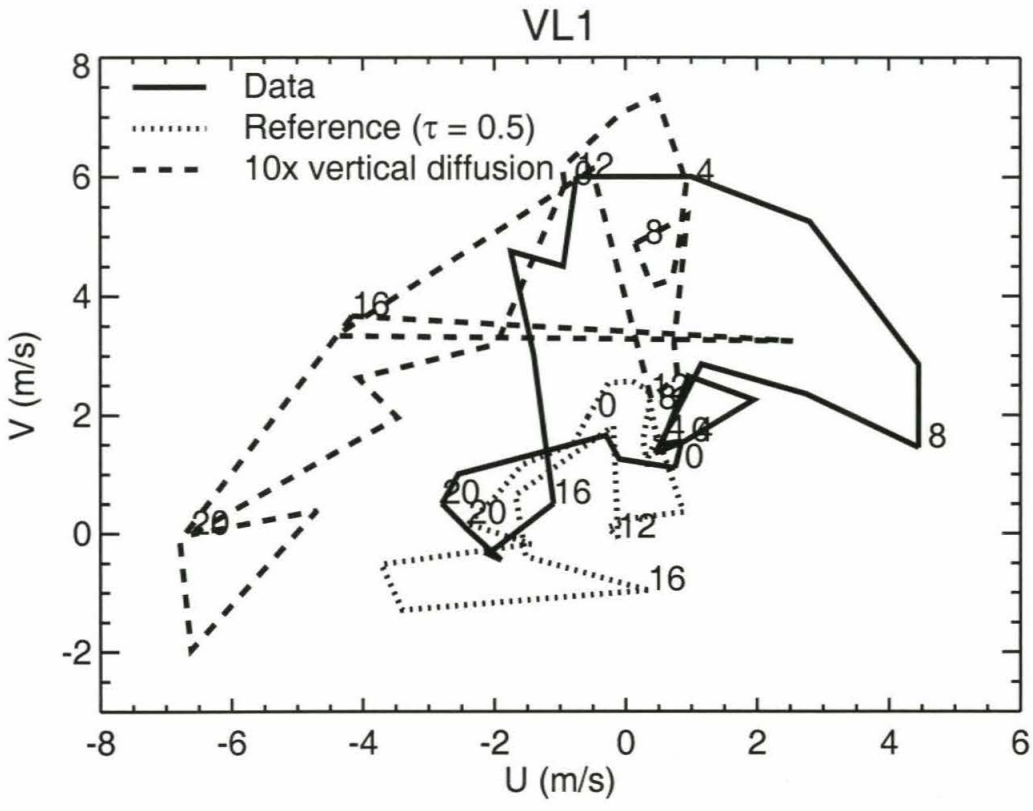

Figure 3.12: Hodograph of the wind velocity vectors at the Viking Lander 1 site. The numbers next to the lines indicate the local hour to which the wind vector is appropriate. The reference case and the location of the other point are the same as in Figure 3.11

as would be expected on the basis of boundary layer theory. Consequently, experiments were conducted where the vertical diffusivity was increased in order to couple the lower level of the model more strongly to these upper level winds. It should be noted that the vertical diffusivities generated by the standard case were compared with those reported by *Savijärvi and Siili* [1993] in order to confirm that there was no error in the boundary layer calculation. Indeed it was found that the model calculated vertical diffusivities very similar to those reported by *Savijärvi and Siili* [1993]. The vertical diffusivity was then increased by a factor of 10 and the impact on the model was examined. This factor of 10 was also used by *Ye et al.* [1990], who derived it as an appropriate scaling factor from

terrestrially-derived vertical diffusivity values to values appropriate to Mars. The structure of the boundary layer with its higher diffusivity is shown in Figure 3.14. The wind maxima that occurred below 1 km in the reference simulation (optical depth = 0.5, without enhanced vertical diffusivity) has been moved up to about 1.5 km. The top of the boundary layer was not significantly affected by the increase in vertical diffusivity. This can be gauged either by examining the wind speed or temperature contours above about 3 km, or by examining the model predicted height of the boundary layer, which is shown as the shaded region in the figures.

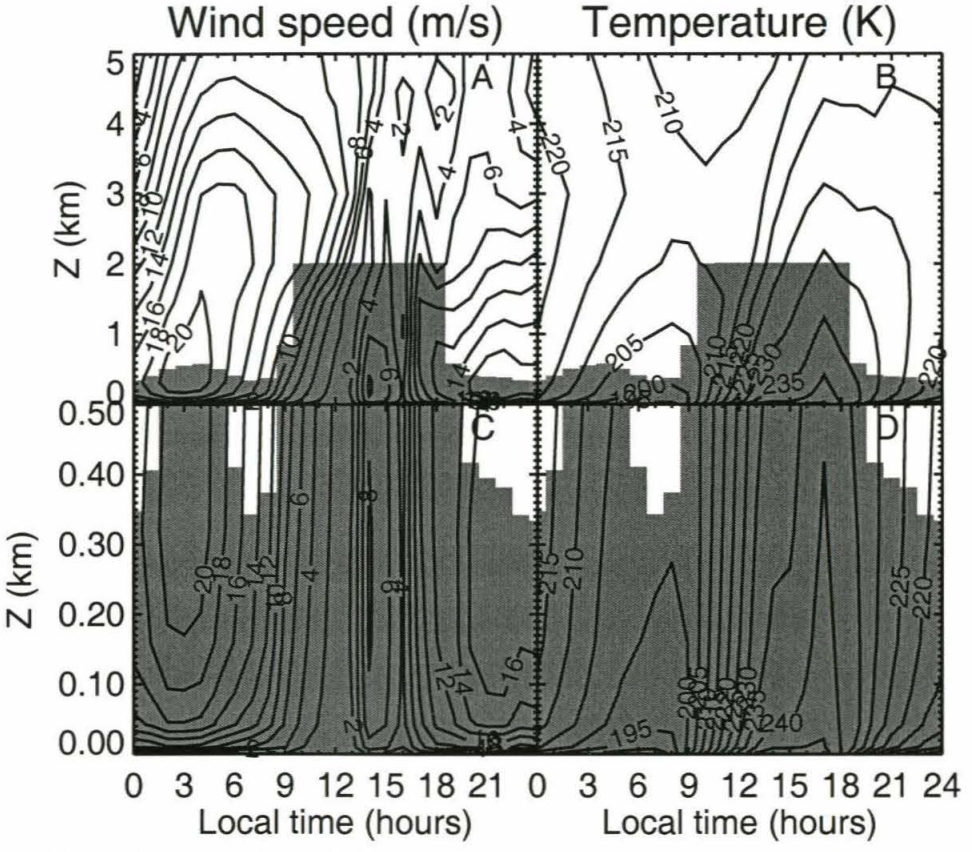

Figure 3.13: Contour plots of the boundary layer at the Viking Lander 1 site as a function of local time. **A & B** are for the range 0 to 5 km, while **C & D** zoom in to the region 0 to 0.5 km. **A & C** show wind speed in m/s as a function of height and time of day, while **B & D** show air temperature in K. The gray background indicates the model-predicted height of the the planetary boundary layer.

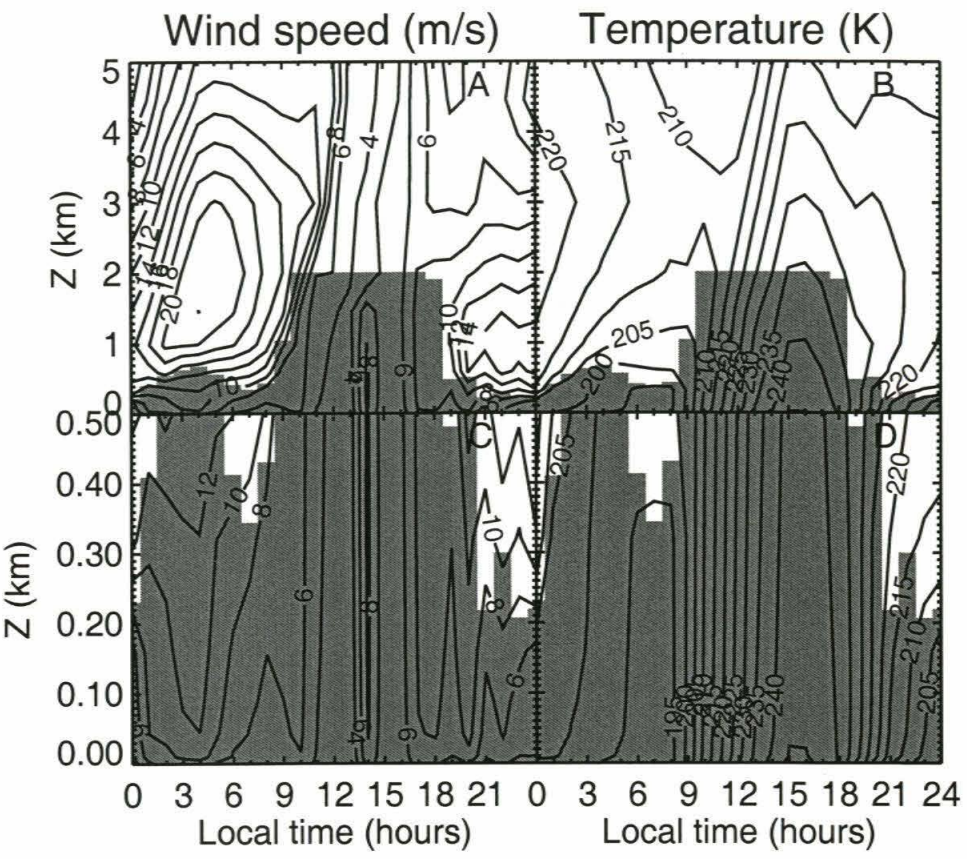

Figure 3.14: Same as Figure 3.13, except for using 10 times larger vertical diffusivities.

The impact on the near surface wind of increased vertical diffusivity is also shown in Figures 3.11 and 3.12. Note that the simulation-to-simulation differences in wind direction variability are not associated with the choice of averaging period. The same pattern of local time wind direction variability is repeated in each simulation regardless of the length of averaging period. The differences truly represent changes in in the wind direction behavior. The increased vertical diffusion significantly improves the wind directions as well as increasing the speeds to near the observed values. Unfortunately, there remains a phase shift in the relationship between the wind directions and speeds, i.e. peak winds occur at different times in the model and in the data.

In examining the wind directions at the Viking Lander 1 landing site, *Haberle et al.*

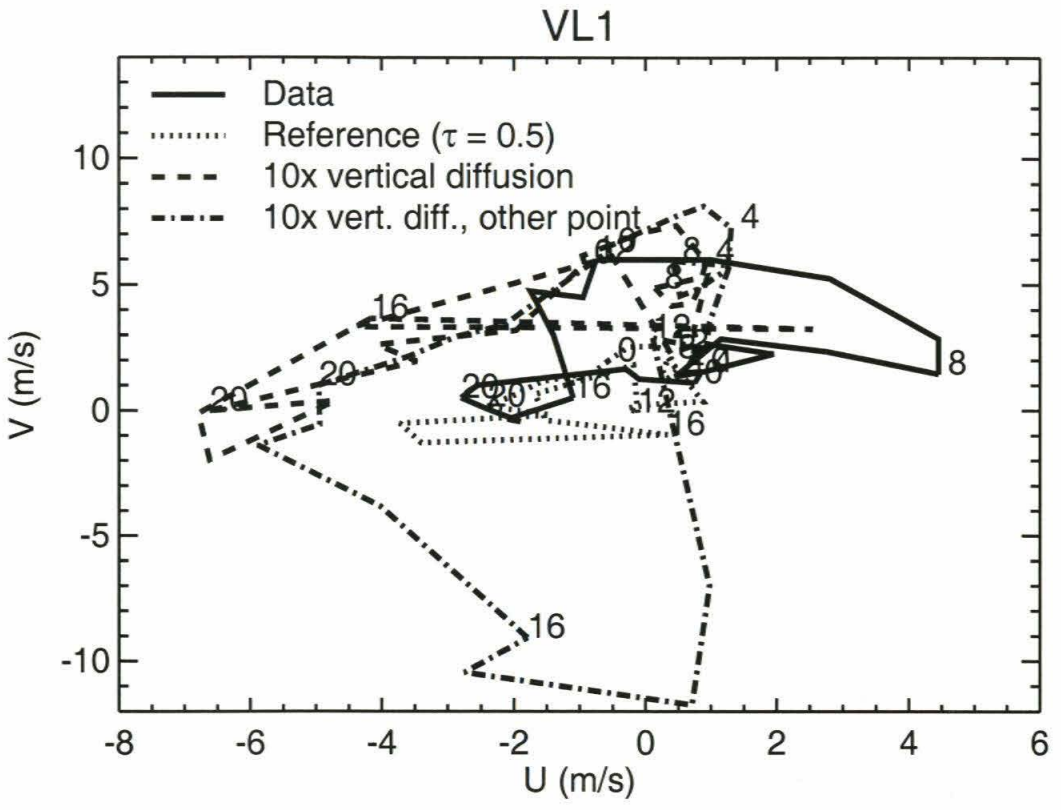

Figure 3.15: Same as Figure 3.12, except that the inclusion of velocity vectors from the other sample point mentioned in Figure 3.11.

[1993] were able to fit the wind velocities with a one-dimensional slope-wind model, but only by using a slope of different direction to that inferred from the pre-MOLA topography data. The slope direction and magnitude used by *Haberle et al.* [1993] differ from those derived from the MOLA 1/16 degree topography dataset at the reported Viking Lander 1 location. The values used by *Haberle et al.* [1993] are a slope of 0.003, downward to the northeast, while the value from the MOLA data is 0.0046, downward to the southeast. In order to examine the effect of slope, another point in the model domain with a slope direction and magnitude very similar to those used by *Haberle et al.* [1993] was chosen. The wind directions for this point are also plotted in Figure 3.11, while the hodograph is shown in Figure 3.15 (labeled in both figures as the "other point"). This point represents

a significantly worse fit to both the wind direction and hodograph of the data. The role of slope on wind velocities will be further investigated while discussing the VL2 data in the next section.

Wind velocities during the Viking Lander 1 and Viking Lander 2 entries simulated by the Mars MM5 agree with those simulated by the one-dimensional boundary layer model of *Haberle et al.* [1993]. This means that the Mars MM5 also disagrees with the magnitude and direction of rotation (with height) of winds derived from entry tracking by *Seiff* [1993].

3.4.3 Viking Lander 2 Site

At the Viking Lander 2 site, two different seasons were examined. The long baseline of observations at Viking Lander 2 afford us the opportunity to examine northern winter conditions that were unavailable at either of the other two previously discussed landing sites. Based again on the availability of data (including compromises in quality among the different variables), the period around L_s 334 was chosen for examination. For the northern summer Viking Lander 2 period, L_s 130 was chosen in order to compare the simulations with the results reported by *Haberle et al.* [1993] and *Savijärvi and Siili* [1993].

3.4.3.1 Winter

Once again, the model simulation of surface pressure demonstrates that the Mars MM5 is accurately propagating the global tidal field generated by the GCM (Figure 3.16). In this case, the semi-diurnal tide is well captured, in both magnitude and phase, but the magnitude of the diurnal tide appears to be somewhat underpredicted, although caveats regarding the quality of the data discussed in Section 3.4.2 should be borne in mind.

Near surface air temperatures are shown in Figure 3.17. At this season, dust opacity is shown to have a large effect on daytime peak air temperatures. The best fit appears to be for an optical depth of approximately 1.5. The model does not appear to fully capture

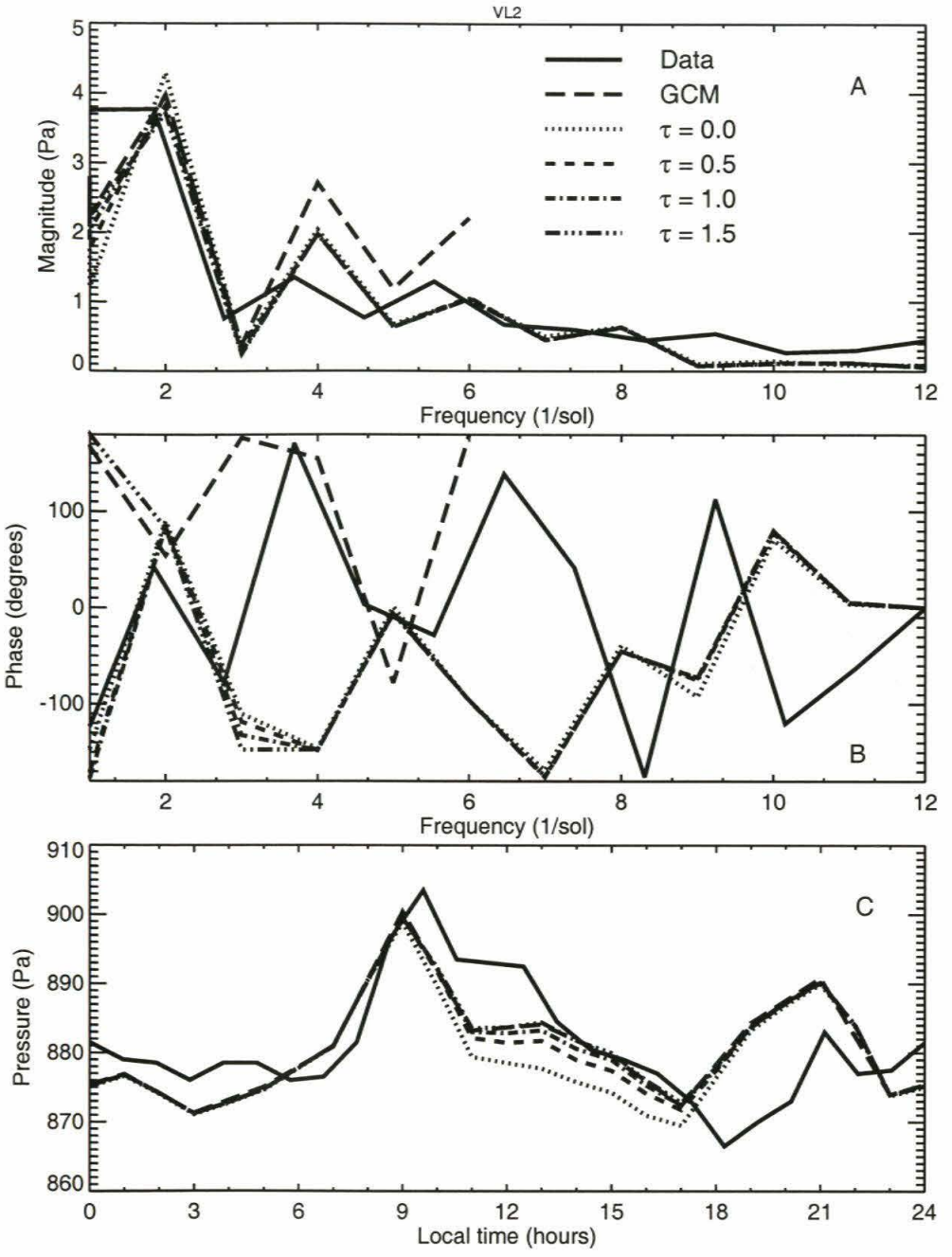

Figure 3.16: Same as Figure 3.5, except at the Viking Lander 2 site. The time of year is L_s 334.

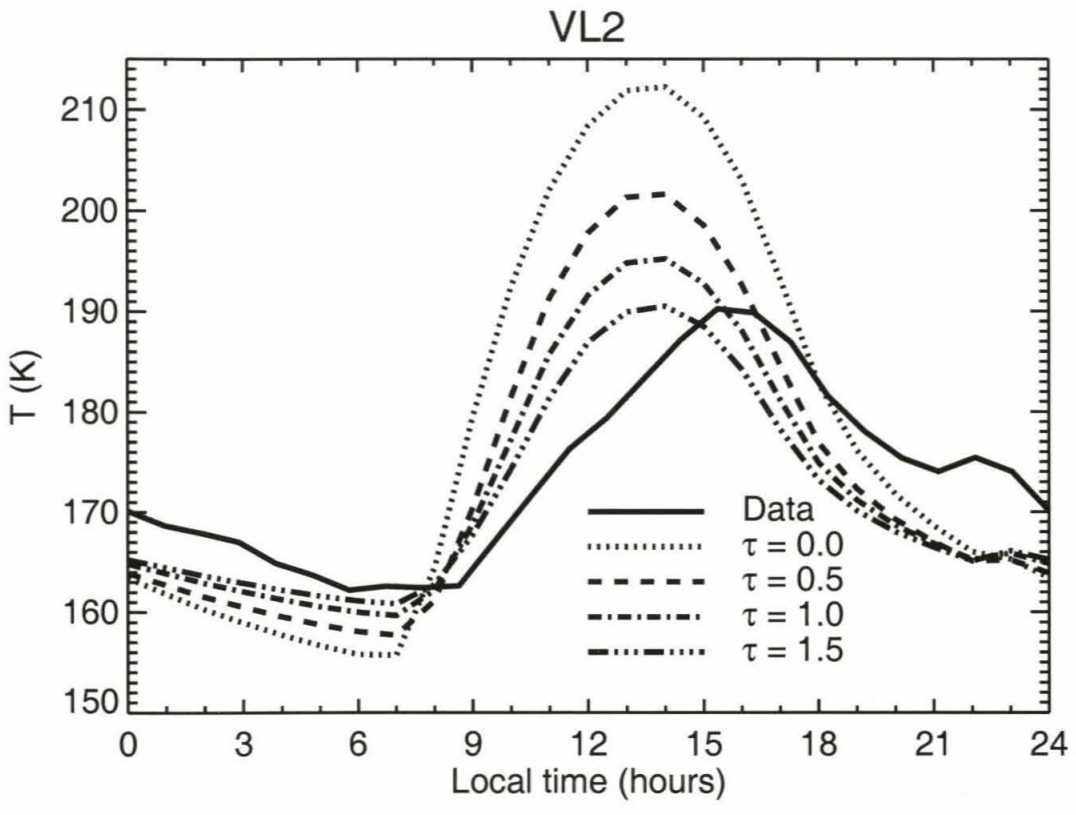

Figure 3.17: Plots of the diurnal temperature cycle at the Viking Lander 2 site during northern summer for both the measured data and the model output for various optical depth cases.

the phasing of the diurnal cycle of air temperature, being somewhat too early to heat up in the morning and too early to cool off at night. Note that this is the opposite behavior to that exhibited at the Mars Pathfinder site. Thus, there is no systematic error in the model with respect to lander observations. Instead discrepancies are landing-site specific and, therefore, more likely related to local errors such as slope, thermal inertia, or albedo. The lander observations for this period are very interesting in that they show a great deal of day-to-day variation in air temperature, on the order of 10 K or more (not shown). Thus, attempts to match the model to the observations are made somewhat difficult. The model does generate day-to-day variation in temperature associated with the passage of

baroclinic storm systems generated by the GCM. However, these systems are still quite regular compared to the data. Given all these factors, the fit to air temperature still appears to be quite good.

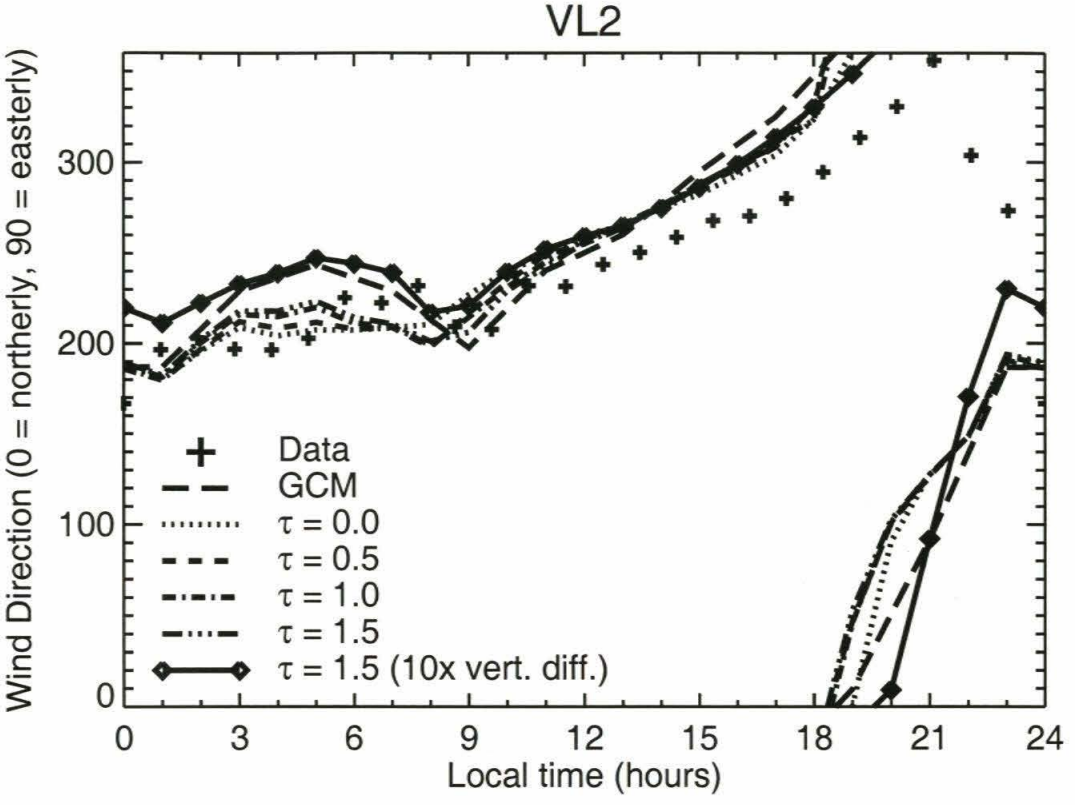

Figure 3.18: As Figure 3.8, except at the Viking Lander 2 site.

All of the Mars MM5 optical depth cases and the GCM do a good job of fitting the predominantly westerly winds throughout most of the day (Figure 3.18). Differences occur in the late evening where all of the models suggest a rotation while the data do not rotate. As with the pressure data, the day-to-day variability of the Viking Lander 2 wind data is also quite high. In an attempt to mitigate the variability due to weather, an average of two days was taken. However, even after taking an average, errors in simulating the data result from differences in phase of the weather systems, and from the failure of the joint model

system to generate truly chaotic weather. The fact that the GCM and the Mars MM5 cases agree so well with each other is indicative of the strong control of the wind regime by baroclinic and tidal processes (i.e., there does not appear to be significant modification due to local topography).

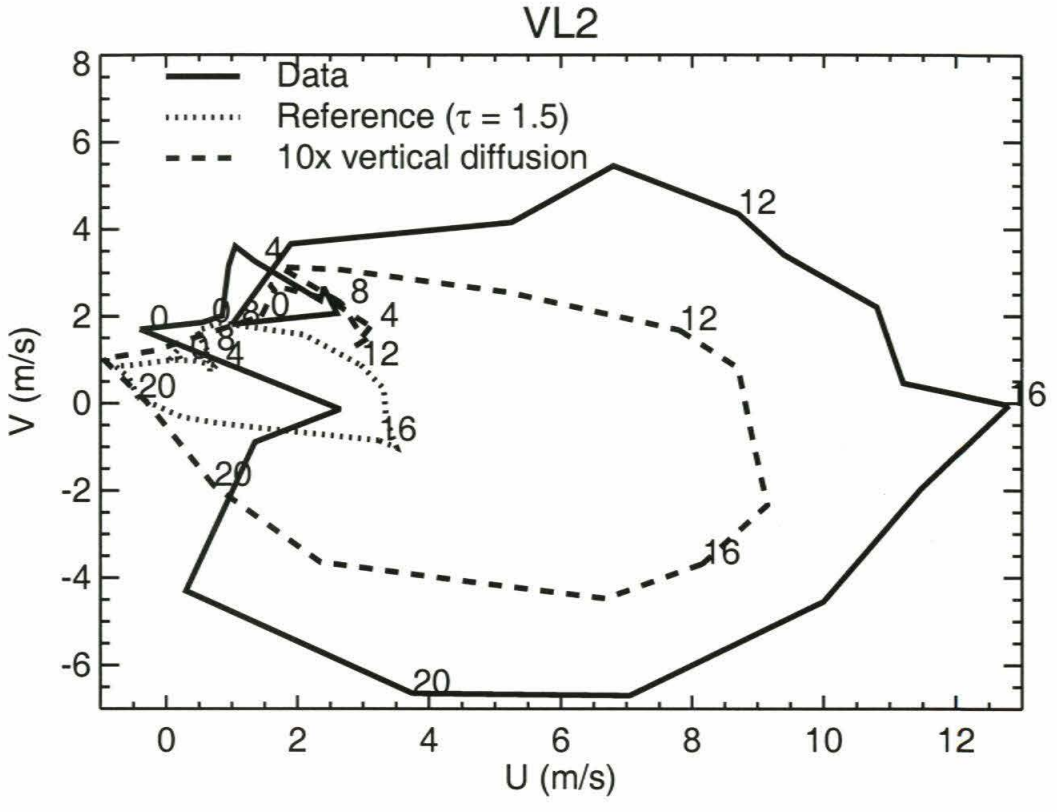

Figure 3.19: Hodograph of wind velocities at the Viking Lander 2 site during northern winter. The numbers next to the lines indicate the local hour to which the wind vector is appropriate. The standard case is for an optical depth of 1.5.

Figure 3.19 shows that the underprediction of wind speeds exhibited at the Viking Lander 1 site during summer also occurs at the Viking Lander 2 site during winter. Peak winds during the late afternoon are about a factor of 3 too slow. However, unlike the Viking Lander 1 summer case, the phasing of peak winds is correctly reproduced. In an extension of the experiment with increasing vertical diffusivity, a simulation for this period and loca-

tion was run using vertical diffusivities increased by a factor of 10. The results are shown in Figure 3.19. This simulation has significantly increased winds which only fall slightly short of reproducing the Viking Lander 2 data.

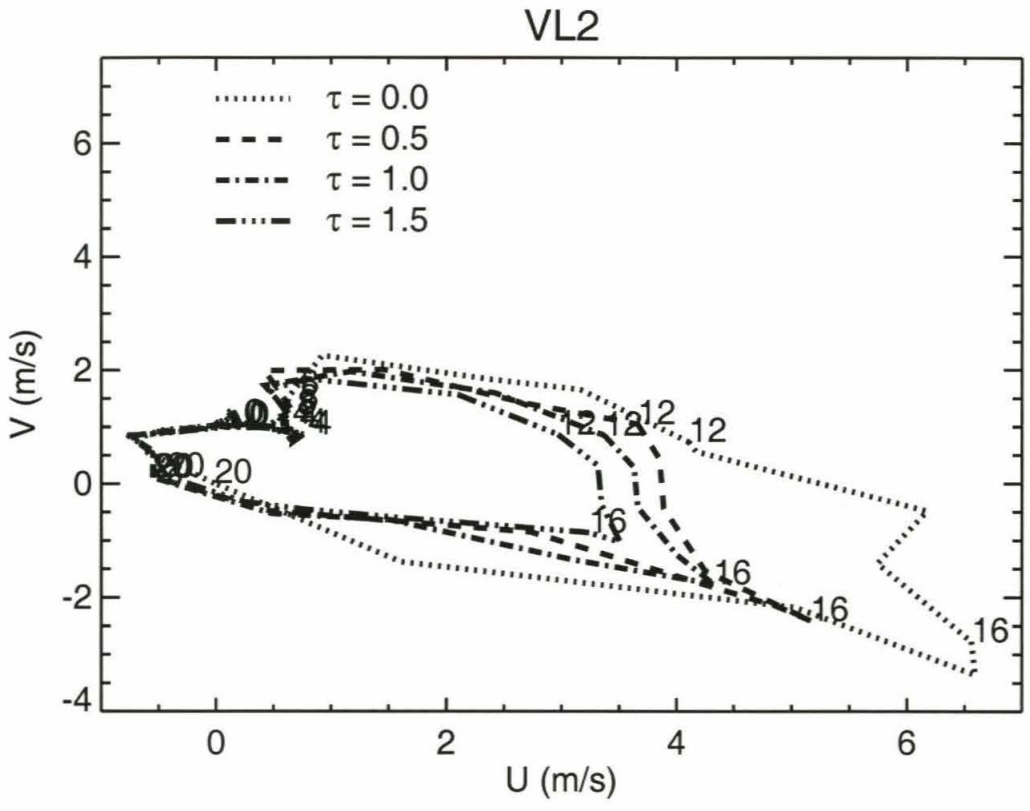

Figure 3.20: Hodograph of wind velocities at the Viking Lander 2 site during northern winter for the various optical depth cases. The numbers next to the lines indicate the local hour to which the wind vector is appropriate.

Increasing the vertical diffusivity effectively couples the lower levels of the model, equivalent to those sampled by the Viking Lander sensors, to the stronger upper level winds. An equivalent increase in vertical diffusivity occurs in the standard model as the optical depth is decreased. Here, the reduction in optical depth cools the atmosphere and warms the surface. The effect of this is to decrease the static stability, increasing the vertical mixing. Figure 3.20 shows the hodographs for the four optical depth cases and demonstrates that the

strongest daytime winds occur for the clearest atmosphere case and decrease monotonically with increasing optical depth.

3.4.3.2 Summer

A second simulation at Viking Lander 2 during northern summer (L_s 130) was run primarily to compare with previous studies [*Haberle et al.*, 1993; *Savijärvi and Siili*, 1993]. In this case the different optical depth cases are not shown, since this type of experiment was already done at the same location (in winter) and during the same period (at Viking Lander 1). Instead, shown are the best fit optical depth, 0.5, and then other parameters are varied to investigate their effect.

Any pressure comparisons for the summer period (L_s 130) are not shown as the data is so poor. The temperature data is quite good and is shown in Figure 3.21. The model fits to data for this period are reasonable, and only the best fit opacity is shown. Slight differences between the model and data include under-prediction of nighttime temperatures and slightly delayed cooling in the evening. These differences (which were similar in the winter case) suggest that the thermal inertia used in the model is too low or there are slope influences on the phasing of absorbed solar radiation.

Wind directions are shown in Figure 3.22. The Mars MM5 does a reasonable job fitting directions from late afternoon until late morning. During the middle of the day, the reference case oscillates in direction somewhat more than the data, but in the same sense. It should be noted this reference case includes the effect of 10 times vertical diffusivity. This can be seen in Figure 3.23, where the wind magnitudes are comparable to those of the data. Unfortunately, the phasing of wind maxima does not correspond to the data. The model generates peak winds during the late afternoon and early evening, while the data suggests peak winds in the mid to late morning. This again differs from studies using simple, one-dimensional slope models [*Haberle et al.*, 1993; *Savijärvi and Siili*, 1993]. Thus the effects of slope versus global tide on the wind directions was examined.

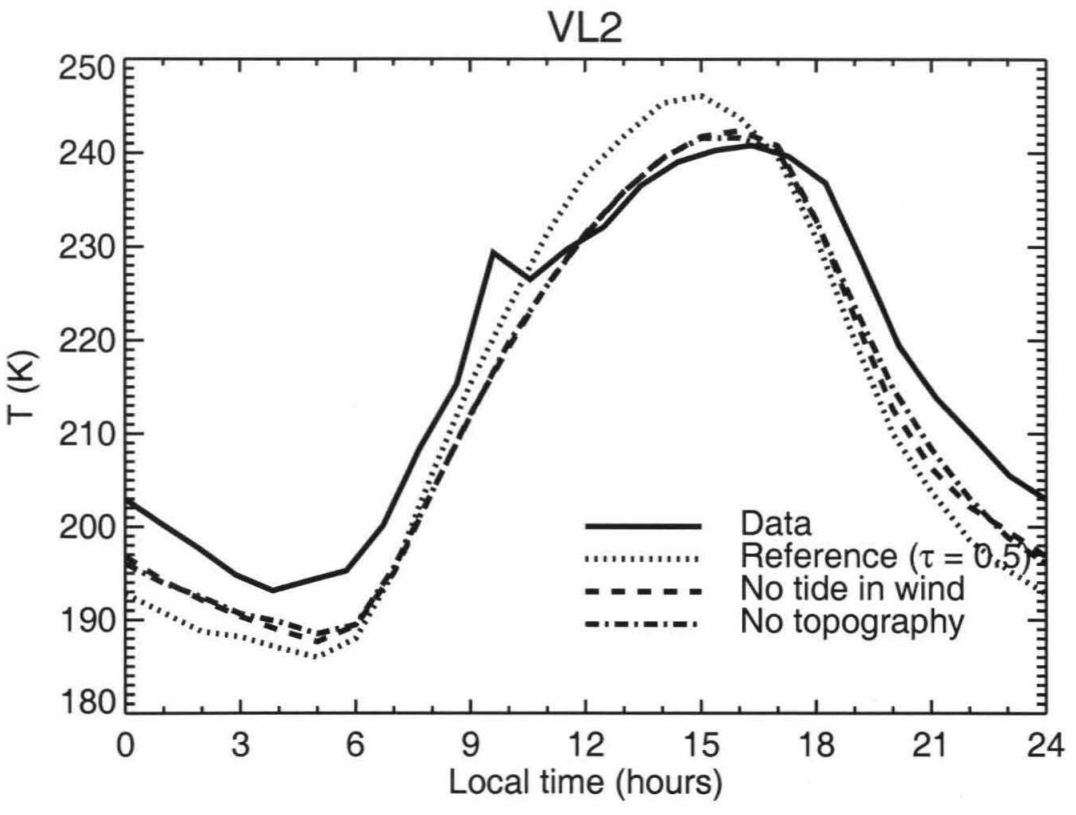

Figure 3.21: Diurnal cycle of near-surface air temperatures, from measurements and model simulations, at the Viking Lander 2 site during northern summer. The reference case is for an optical depth of 0.5. "No tide in wind" refers to the simulation where the daily average wind was used for the boundary conditions, and was invariant in time. "No topography" refers to the simulation where the model domain was initialized with a flat surface at the height of the Viking Lander 2 location.

In the first modified simulation, the effects of the global tide on the imposed wind field (i.e., the boundary and initial conditions) were removed. This is equivalent to the imposition of a uniform wind in the slope models. The results are shown in Figures 3.22 and 3.23. The quality of the fit to wind direction is significantly degraded. The directions begin to disagree just after midnight and do not agree again until late evening. Further, there is very little variation in direction (less than 90°) during the entire day. This can also be seen in the hodograph. Although the conditions now mimic those used in slope wind

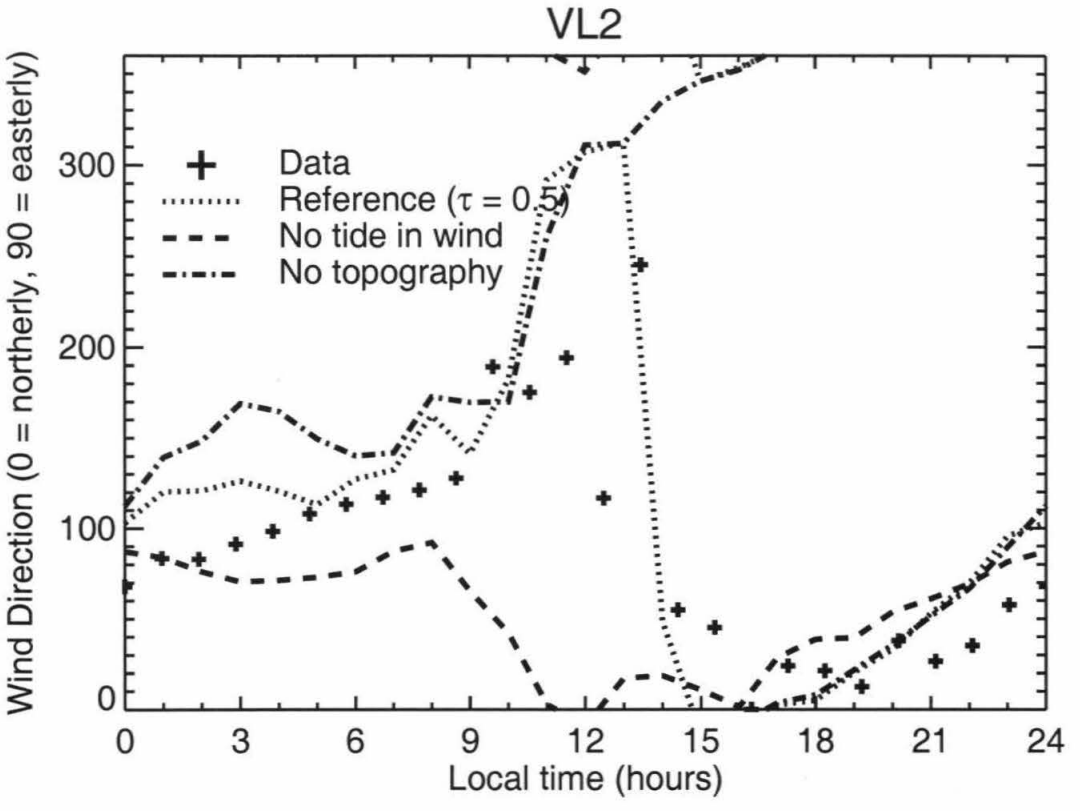

Figure 3.22: Wind directions as a function of local time for the Viking Lander 2 location during norther summer. The different cases are the same as described in Figure 3.21.

models, the Mars MM5 does not generate the observed velocities.

Next, the topography was removed to investigate the effect of global tides in isolation from slope effects. These results can also be seen in Figures 3.22 and 3.23. The fit to directions again is relatively poor, except in the late afternoon and evening. However, in this case, a full 360° rotation occurs and the simulation is somewhat similar to the standard simulation for the first half of the day. The hodograph for this case is quite simple, with a smooth circular rotation, peak winds occurring in the late afternoon and exceeding the peak observed values by about a factor of 2.

The combination of these results suggests that both tides and slopes contribute. This is also supported by the Viking Lander 1 result where a different location within the model

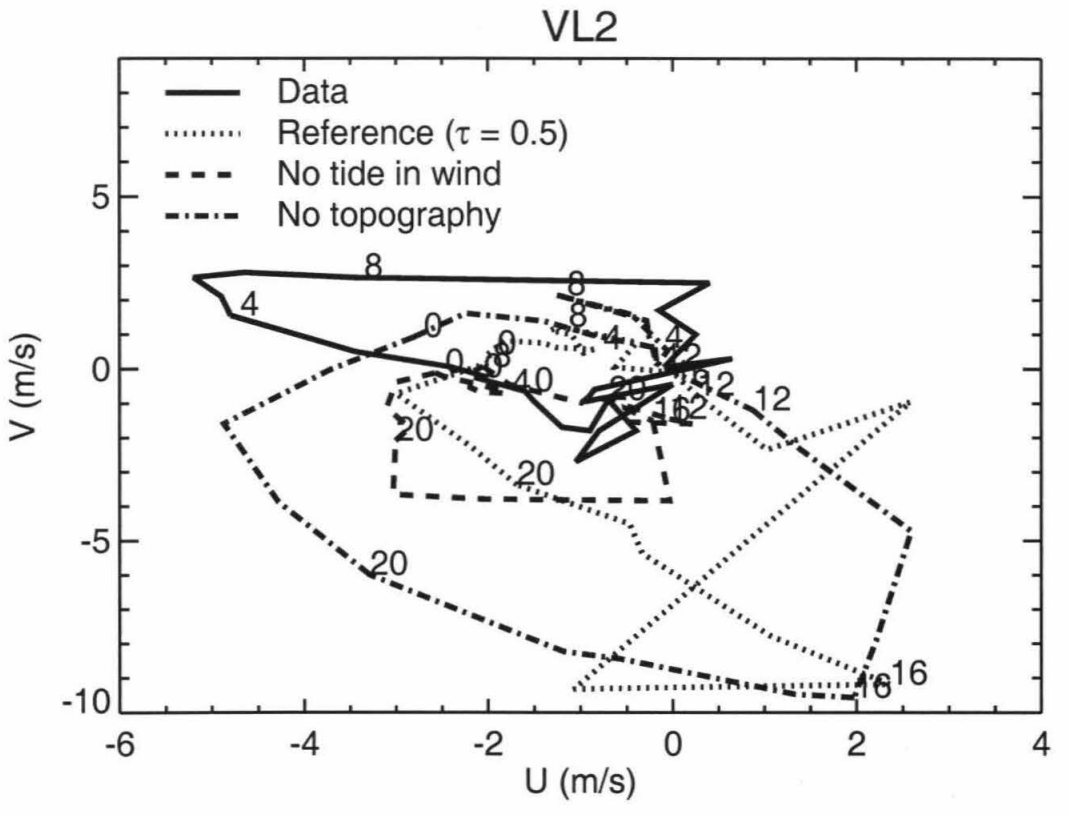

Figure 3.23: Hodograph of the wind velocity vectors for the measured data and for the model simulations at the Viking Lander 2 site during northern summer. The numbers next to the lines indicate the local hour to which the wind vector is appropriate. The different cases are the same as described in Figure 3.21.

domain with a different slope generated a rather different hodograph than the standard simulation (Figure 3.15). Thus, this experiment was repeated with the Viking Lander 2 summer simulation. Three more locations within the model domain with slope directions that were approximately 90° apart were explicitly selected. The Viking Lander 2 site within this domain has a slope of 0.006, downward to the northwest. Locations near the center of the domain were chosen, with slopes of: (point 2) 0.011, downward to the southeast; (point 3) 0.011, downward to the southwest; (point 4) 0.003, downward to the northeast. In this case the hodographs appear largely insensitive to local slope direction, as can be seen

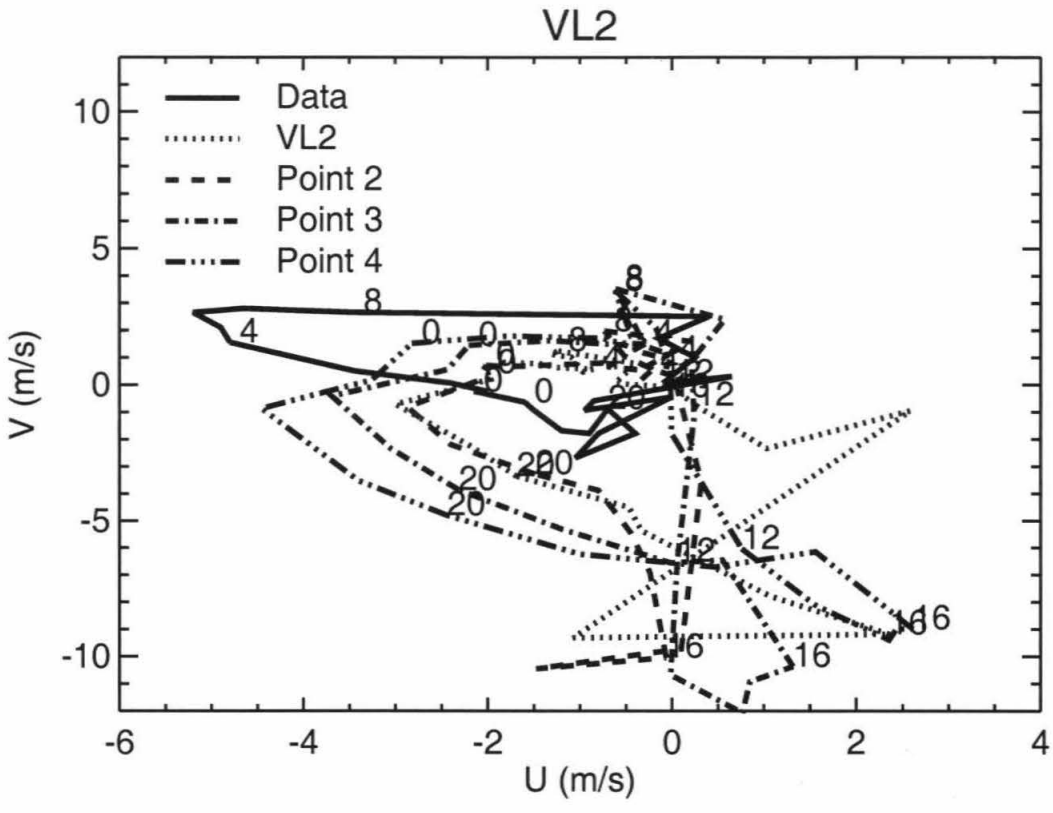

Figure 3.24: Hodograph of the wind velocity vectors from the reference model simulation for four different locations in the model domain, plotted along with the wind velocities measured at Viking Lander 2 during northern summer. The four different points have slopes about 90° from each other, and magnitude of the largest slope is within a factor of 4 of the smallest. The numbers next to the lines indicate the local hour to which the wind vector is appropriate.

in Figure 3.24. This is consistent with examination of time series maps of wind direction, where the direction is fairly uniform across the entire domain (approximately 120 km; not shown). This is again different from the case of Viking Lander 1. Apparently, local slopes (on the scale of a few to a few tens of kilometers) are not particularly important in determining wind direction at the Viking Lander 2 site. The finding that the elimination of slope does affect wind direction suggests the important scale of slope forcing is between the scale resolvable by the GCM and that of the mesoscale model domain.

Although not shown, the effect of horizontal resolution on the quality of fits at the Viking Lander 2 site was also examined. Experiments were conducted with a horizontal resolution of 4 km (the default for all of the previous lander simulations), 16 km and 60 km. There was no noticeable difference between the simulations, in any of the variables, which is consistent with the results described in the previous paragraph. That topography of a scale smaller than roughly 100 km does not markedly influence the simulations is not a general result, as indicated by the Viking Lander 1 simulations. The landing sites were preselected to be relatively flat and this appears to be particularly the case at Viking Lander 2. However, in regions where topography is large on small horizontal scales (e.g., craters, canyons, channels, chaotic terrain, etc.), the circulation is expected to exhibit sensitivity.

3.5 Summary

The Earth PSU/NCAR Mesoscale Model Version 5 (MM5) was fully converted to Mars using the Mars-specific parameterizations of the GFDL Mars GCM. Output from the GFDL Mars GCM was used to initialize and drive (i.e., provide time-evolving boundary conditions for) the Mars MM5.

In comparing to the GCM, the biggest limitation is imposed by the finite model height and the rigid lid. This has the effect in the global simulations of confining the Hadley circulation. As a result, the zonal wind field and the distribution of dust particles are modified from those in the GCM. This suggests that careful attention must be paid to the design of mesoscale model domains for experiments where simulation of the Hadley flow is important, and a sufficiently high model top must be selected. For simulations of near-surface flow phenomena, this is less important as near-surface flow on Mars appears to be strongly controlled by topography. Some attention must also be given to the horizontal extent of the domain and the location and scale of the processes to be examined, e.g., making sure that the domain has sufficient latitudinal extent to fully capture the width of baroclinic storm

systems.

The Mars MM5 is found to accurately capture most of the structures generated in the GCM when the Mars MM5 domain is essentially global. This fidelity extends even to the reasonable simulation of the three-dimensional distribution of dust, which involves detailed radiative and dynamical feedback systems. The one caveat is again the limitation of Hadley flow imposed by the model top.

Near-surface air temperatures measured by the two Viking Landers and Mars Pathfinder are relatively well-simulated for all seasons examined. This suggests that both the subsurface heat diffusion code and the surface layer parameterization are good. Some errors in phasing of the diurnal temperature cycle are found especially at Viking Lander 2 during winter. Other than possible errors in the lander data, these errors suggest either small errors in the thermal inertia used, or the lack of treatment of slopes in the calculation of absorbed insolation.

The Mars MM5 faithfully reproduces the variations in surface pressure generated by the GCM. As most of these pressure variations result from large to global scale dynamical systems (e.g., the global tide or baroclinic storm systems), it is not surprising that the Mars MM5 does not significantly alter them. Indeed, the fact that they are reproduced so faithfully suggests that the coupling of the Mars MM5 to the GCM through the time-evolving boundary conditions is well-implemented.

Wind directions for all the landing sites and for all seasons are relatively wellreproduced. In most cases, the Mars MM5 variation in wind directions is not greatly different from that generated by the GCM. This suggests that control of wind directions is provided by the global tide as modified by topography on a scale greater than a few hundred kilometers. However, locations in the Mars MM5 model domain that are more proximate to large local topography exhibit significant deviations from the large scale (GCM-predicted) flow (not shown). Wind directions provided by the GCM are reported for a height of roughly 200 m above the surface, and that consequently there appears to be little rotation in the

lower boundary layer. In general, the prediction of wind directions appears to be quite good.

Unfortunately, the peak wind speeds at all locations and all seasons are systematically underpredicted. Furthermore, the phasing of wind speed as a function of local time is not well-reproduced for any landing site, except for Viking Lander 2 in winter. In order to generate daily variations in wind speed comparable to those observed, the vertical diffusivity was increased by a factor of 10, as suggested by *Ye et al.* [1990]. However, this increase did not correct the phasing problem. Therefore, further work needs to be done to examine the behavior of wind in the lower boundary layer. Specifically a detailed study of the applicability of the terrestrial planetary boundary layer parameterizations to Mars and their use in Martian numerical models needs to be undertaken. However, such a large study is beyond the scope of this paper. Given that wind speeds are underpredicted, and that the wind speeds and their phasing at approximately 200 m agree with the GCM, the Mars MM5 represents a conservative tool for the investigation of processes such as dust lifting where wind speed is important. It should be noted that wind speeds generated by the mesoscale model near the 5 m level for the Mars Pathfinder site and season agree quite well with those generated by the NASA Ames Mars GCM [*Haberle et al.*, 1999], which includes a "level 2" *Mellor and Yamada* [1982] scheme. Thus, there would not appear to be a major difference between these two model boundary layer schemes. The one-dimensional boundary layer model of *Haberle et al.* [1993] is able to fit the observed wind speeds despite neglecting what this study suggests should be important dynamics, i.e. global tides. However, the fits result from tuning the slope magnitude and direction and a mixing depth parameter. The two-dimensional model of *Savijärvi and Siili* [1993] does not produce significantly better fits to the landing site winds than the Mars MM5. Clearly the mix of processes controlling surface level winds is not yet understood.

A significant result in relation to previous studies of the diurnal cycle of winds relates to their driving mechanism. In one-dimensional boundary layer models it has been common

to apply uniform upper level winds and allow the diurnal cycle of wind to be generated by slope forcing [*Haberle et al.*, 1993; *Savijärvi and Siili*, 1993]. Results suggest that the global tide is at least as important as local slope in generating the variability of winds. Indeed, at Mars Pathfinder and Viking Lander 2, slopes on a scale smaller than that of the GCM grid spacing (a few hundred kilometers) are not particularly important. Future work needs to be done focusing on wind speed phasing that will require a detailed study of the tides generated in the GCM and passed to the Mars MM5, the interaction of these tides with topography, and the sensitivity of the tides to the three-dimensional distribution of dust. The importance of sub-GCM scale topography in generating slope winds which interact with the global tidal systems requires that such a study be undertaken with a joint GCM/Mars MM5 modeling system.

The work undertaken within this study suggests that when used in combination with a GCM, and when attention is paid to the design of the Mars MM5 experiments and model domain, the Mars MM5 promises to be a powerful tool for the investigation of processes central to the Martian climate on scales from hundreds of kilometers to tens of meters.

4 Dust Lifting and Dust Storms Near the South Pole of Mars

Abstract

Surface wind stresses and dust lifting in the south polar region of Mars are examined with a three-dimensional numerical model. Due to the availability of high quality observations from the Mars Global Surveyor (MGS) spacecraft, the focus of this study is the mid to late southern spring period. Color images from the Mars Orbiter Camera of the south polar region are presented which show frequent dust activity and 9μm dust opacities derived from Thermal Emission Spectrometer observations, which show significant accumulation of dust over the south polar cap before southern summer solstice. Mesoscale model simulations of the high southern latitudes are conducted with a domain centered on the south pole at three dates within this season (L_s 225, L_s 255, and L_s 270). On the assumption that dust injection is related to the movement of sand-sized grains or aggregates, the Mars MM5 mesoscale model predicts surface wind stresses of sufficient strength to initiate movement of sand-sized particles (approximately 100 μm), and hence dust lifting, during all three periods. The availability of dust and/or sand-sized particles is not addressed within this study. Instead, the degree to which the existence of sufficiently strong winds limit dust injection is examined. While dust lifting is observed at many locations on Mars, this study focuses on the mechanisms of cap edge dust lifting near summer solstice. By eliminating forcing elements from the model, the important dynamical modes generating the high wind stresses at the cap edge are isolated. The direct cap edge thermal contrast (and topographic slopes in some locations) provides the primary drive for high surface wind stresses at the cap edge at this season. Sublimation flow is not found to be

particularly important, at least at southern summer solstice. Simulations in which dust is injected into the lowest model layer when wind stresses exceed a threshold show similar patterns of atmospheric dust to those seen in the MGS observations. Comparison between these simulations and those with inactive dust injection show no signs of consistent positive or negative feedback due to dust clouds on the surface wind stress fields during the late spring season examined here. It is noted that there are significant areas that are removed from the polar cap where surface wind stresses exceed the chosen threshold for movement of sand-sized particles. These are found to be related to large scale circulations. Undoubtedly there are many mechanisms for injecting dust into the atmosphere of which high wind stress at the polar cap edge is one.

4.1 Introduction

The mechanisms by which dust is lifted from the surface and injected into the Martian atmosphere are currently not well understood. Numerous suggestions have been advanced based either on observations or on theory. These fall into essentially two categories: free (thermal) convection and large-scale winds (forced convection). The former category includes small scale convective activity (such as dust devils) [*Gierasch and Goody*, 1973; *Thomas and Gierasch*, 1985; *Metzger et al.*, 1999; *Renno et al.*, 2000], while the latter category includes winds associated with baroclinic storm systems, slopes, etc. [*Leovy et al.*, 1973; *Peterfreund and Kieffer*, 1979; *James et al.*, 1999].

However, three-dimensional numerical models to date have not been successful in generating winds (and specifically surface wind stresses, the force per unit area imposed by wind drag on the surface) of sufficient strength to initiate significant dust lifting via saltation of sand if laboratory estimates of the threshold wind stress are accepted [*Anderson et al.*, 1999; *Murphy*, 1999]. Sand-sized particles (of approximately 100 μm diameter) are the first particles to be mobilized on the surface. Saltation of sand has the effect of "kicking" dust into the atmosphere as the sand-sized particles impact the dust [*Greeley and*

Iversen, 1985]. Alternatively, aggregates of dust that have cohered into sand-sized particles can be mobilized with similar wind stresses and collisionally disintegrate back into dust [*Greeley*, 1979]. Since sand-sized particles require the lowest threshold wind stress for mobilization, this has been a favored mechanism for dust injection in the literature. Direct lofting of dust-sized particles requires much higher surface stresses [*Greeley et al.*, 1992]. However, dust-lifting via mobilization of sand-sized particles requires the presence of either sand-sized aggregates or both dust and sand particles. In this study the availability of sand-sized particles is not addressed. Instead, it is assumed either their availability or significant reductions in the required threshold stress to initiate direct injection of dust (i.e., differences between laboratory conditions and Martian conditions, such as low static stability and electrostatic forces [*Greeley et al.*, 1992]). In any case, it is assumed that sufficient wind stress for sand saltation is the limiting factor (which will not always be true) and specifically examine the dynamical processes involved in generating high wind stresses.

One particular area of interest with respect to dust lifting has been the polar cap edge region, in which strong thermal contrasts exist which are expected to generate strong winds in analogy to terrestrial sea breeze circulations. These winds may be augmented by flow due to the sublimation of CO_2 and by the presence of steep slopes in the vicinity of the polar layered terrain, the residual cap, or the seasonal cap edge [*Burk*, 1976; *Haberle et al.*, 1979; *Siili et al.*, 1997, 1999]. The interest in the polar cap edge emerges not only from theoretical considerations, but also from observations of dust activity in these regions [*Kahn et al.*, 1992].

Even in the strongly forced polar regions, general circulation models have been unable to generate significant areas where the laboratory-measured wind stress threshold for mobilization of sand-sized particles is exceeded [*Anderson et al.*, 1999; *Murphy*, 1999]. There are three potential reasons for this. First, global scale models may not possess sufficient horizontal resolution to properly simulate the important circulation systems. Second, while higher resolution mesoscale models have been applied to cap edge and slope winds, these

models have been two-dimensional and have not included all the dynamical processes of potential importance [*Siili et al.*, 1997, 1999]. Third, the laboratory-measured wind stress thresholds may be unrealistically high for the true Martian environment (due to not accounting for unstable atmospheric conditions and electrostatic forces).

The study of dust lifting by a variety of processes and at a variety of locations must be undertaken to fully understand the dust cycle on Mars and how dust is injected into the atmosphere. However, this is too large a question to attack in one study alone. Thus, as a first step towards answering this question, focus was placed on both a particular mechanism favored in the literature and a particular location of known dust activity. In this study, focus was placed on the development of cap edge storms along the retreating edge of the southern spring polar cap. It is assumed that dust lifting is controlled by mobilization of sand-sized particles, that the threshold for mobilization is as derived in laboratory observations, and that sand-size particles and/or dust are infinitely available. Hence it is assumed that dust lifting is limited only by the ability of the atmosphere to generate wind of sufficient strength to initiate mobilization of sand-sized particles, and the dynamical processes leading to high wind stresses are examined. While it is evident that the availability of sand-sized particles will provide an important constraint on dust lifting in the aforementioned scenario, examination of that constraint is deferred to other studies in order to isolate dynamical constraints on dust lifting by mobilization of sand-sized particles. It is also apparent that dust lifting can occur by other mechanisms, e.g., dust devils. These mechanisms should also be examined and would be complementary to this study.

The focus of this study on cap edge dust lifting along the retreating edge of the southern spring polar cap is motivated by examination of newly acquired Mars Global Surveyor (MGS) Mars Orbiter Camera (MOC) color images and Thermal Emission Spectrometer (TES) 9 μm dust optical depth measurements demonstrating dust activity near the south pole [*Malin et al.*, 1992; *Christensen et al.*, 1992]. The Mars mesoscale model (Mars MM5) / Geophysical Fluid Dynamics Laboratory (GFDL) Mars General Circulation Model

(GCM) modeling system (Chapter 3) is employed to address a number of significant questions relating to the lifting of dust near the south polar cap. These are:

- Can the critical saltation-initiating stress threshold be exceeded?
- What scales of motion are important?
- What conditions create winds that exceed threshold (local time, cap temperature contrast, etc.)?
- Is there any dust feedback on lifting once dust is lofted?

Descriptions of the models (Section 4.2) are provided and then some examples of cap edge dust storm systems observed by MGS (Section 4.3) are shown. The behavior of the standard model is examined at three different seasonal dates with the specific goal of determining whether the surface wind stress threshold is exceeded (Section 4.4). In Section 4.5, circulation components most important for causing high surface stresses are isolated, specifically bt examining the model simulation at southern summer solstice. In Section 4.6, dust injection is coupled to those locations where stress thresholds are exceeded in order to examine whether radiative/dynamical feedbacks associated with lofted dust enhance or diminish surface stresses. Finally, in Section 4.7 conclusions are summarized.

4.2 Model description

In this study both the Mars Mesoscale Model (Mars MM5), presented in Chapter 3, and the GFDL Mars GCM [*Wilson and Hamilton*, 1996] are used. These models are briefly described here.

The GFDL Mars GCM is based upon the well-known GFDL "Skyhi" troposphere-stratosphere-mesosphere terrestrial model. The Mars GCM includes radiative heating due

to CO_2 gas and atmospheric dust. Dust is treated within the model as a transportable (by model-resolved winds and diffusion) trace species leading to radiatively and dynamically self-consistent circulations. Two dust-particle sizes are considered, roughly 0.6 and 2.5 μm in radius. The background level of dust opacity is maintained by a dust injection scheme which triggers injection of dust if the surface temperature to lowest layer air temperature difference is above a critical value. The model also includes full CO_2 and water cycles (the exchange of CO_2 and water between the atmosphere and surface) [*Richardson*, 1999]. As used in this study, the model has a resolution of 5° in latitude and 6° in longitude with 20 vertical levels between the surface and roughly 85 km. The model is forced by a diurnal and seasonal cycle of incident solar radiation.

The Mars Mesoscale Model is based upon the widely-used Pennsylvania State University/National Center for Atmospheric Research Fifth Generation Mesoscale Model (MM5). The Mars MM5 includes the same Martian-specific physical parameterizations as included in the GFDL Mars GCM, including the use of dust as an injected, transported, and radiatively active species. Being a limited-area model, the Mars MM5 requires specification of time-evolving boundary conditions which are provided in the simulations discussed in this paper by output from the GCM at two-hour intervals. The resolution of the Mars MM5 is variable. The resolution used in specific simulations in this study will be mentioned in the description of those simulations.

4.3 Mars Global Surveyor Observations of South Polar Cap Edge Dust Storms

The Mars Global Surveyor spacecraft has provided systematic sun-synchronous mapping of the Martian atmosphere and surface. This study utilizes the color MOC wide-angle global map swathes [*Malin et al.*, 1992], which can be mosaicked together to provide daily

global maps showing dust activity, and the TES spectra [*Christensen et al.*, 1992], which can be used to derive 9 μm dust opacities. The combination of these two datasets provides a systematic and regular record of dust activity in the south polar region of Mars during spring and summer.

Daily MOC images of the south polar region for southern spring and summer [Wang and Ingersoll, in preparation] were created and examined. Selected examples showing dust activity are presented in Figure 4.1. The raw blue and red MOC images that make up these final image products were extracted from the Planetary Data System (PDS) CD-ROMs. Each image was radiometrically corrected to remove streaks and changes in the camera gain state while the image was being acquired. Then the images were photometrically corrected to remove large scale brightness variations, due to the opposition surge, limb brightening (in the blue images), limb darkening (in the red images), and low frequency camera sensitivity. The photometric corrections have the effect of equalizing the brightness across the whole image. The spacecraft ground track walks westward by 28° on each succeeding orbit and returns to the same longitudes one day later after 13 orbits. The 13 red images were polar sterographically projected and mosaicked together to make one red daily polar map, and likewise for the blue. A composite daily color polar map was made by empirically mixing the red and blue images subject to the constraint that polar caps are "white." Three daily color polar maps are shown in Figure 4.1. These images were selected as the best examples of dust activity near the cap edge while the cap was relatively large and circular (L_s 228), when the 9 μm dust optical depths were increasing (L_s 260), and at solstice (L_s 271).

The TES observations do not provide complete global coverage on a daily basis. Polar stereographic maps of TES observations are compiled in Figure 4.1 by binning and averaging over 5° of L_s, or a little over 5 Martian days at this season. L_s is the angular measure of season for Mars, where L_s 0 corresponds to northern spring equinox, L_s 90 corresponds to northern summer solstice, etc. Individual daytime TES spectra were convolved with the Viking Infrared Thermal Mapper (IRTM) channel spectral response functions, and the

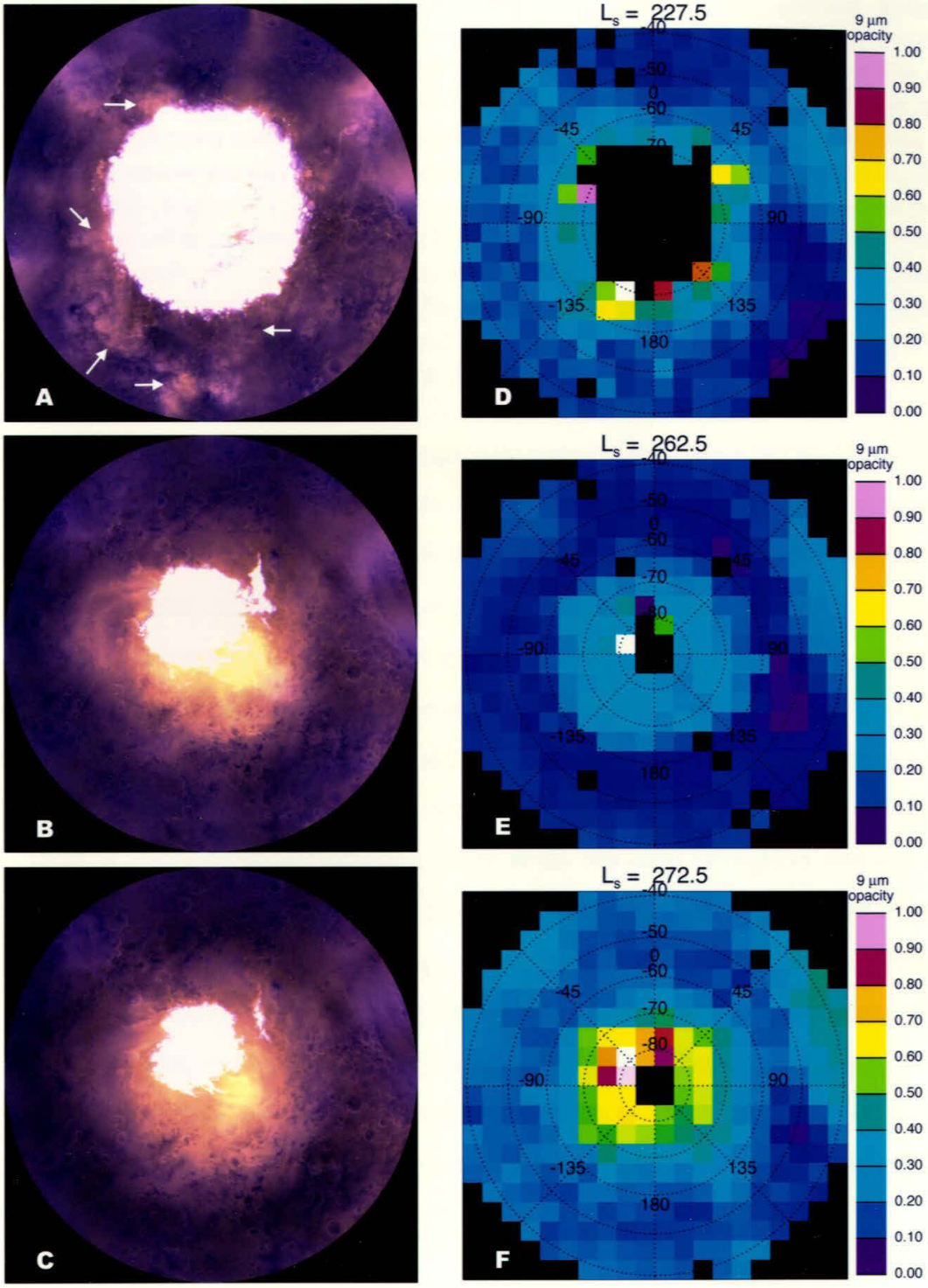
A
B
C
L_s = 227.5
L_s = 262.5
L_s = 272.5
D
E
F
9 µm opacity
1.00
0.90
0.80
0.70
0.60
0.50
0.40
0.30
0.20
0.10
0.00
-40
-50
0
-60
-45
45
-70
-80
-90
90
-135
135
180

Figure 4.1: [p. 85] **A:** MOC mosaic of the south pole at L_s 228. The outer edge of the image is at 45° S. The seasonal cap extends to about 68° S and is roughly circular. Yellow-brown dust clouds (next to the white arrows) can be seen all around the edge of the cap, and a large dust cloud (also indicated with an arrow) can be seen separate from the cap at the bottom of the map. **B:** MOC mosaic of the south pole at L_s 260. The cap is now asymmetrical, and more centered on its residual location. Diffuse dust is observed over the layered terrain region and there is less evidence for discrete "puffy" clouds seen at L_s 228. Filamentary dust clouds are observed streaming off the cap edge in the left half of the map. **C:** MOC mosaic of the south pole at L_s 271. The cap is almost back to its residual form. The dust cloud seen near the center is almost completely diffuse. There is little evidence either for discrete "puffy" clouds or for filamentary structures. **D:** Map of TES-derived 9μm opacities at L_s 227.5. Data are binned by 5° in L_s and in 5° boxes. **E:** Same as **D**, except at L_s 262.5. **F:** Same as **D**, except at L_s 272.5.

resulting channel radiances converted to brightness temperature. These IRTM-like (or synthetic IRTM) brightness temperatures are then used to calculate 9 μm optical depths following the method of *Martin* [1986], which are then directly comparable to those observed by Viking [*Martin*, 1986; *Martin and Richardson*, 1993]. The individual 9 μm optical depth measurements are binned in 240 km boxes in polar stereographic projection.

Both the MOC images and the TES opacity maps show significant dust activity near the edge of the retreating south seasonal ice cap throughout mid and late southern spring. By late southern spring and summer solstice, dust is concentrated within 25° of the rotational pole. There is evidence for sporadic dust lifting at the cap edge throughout mid and late spring. The L_s 228 image (Figure 4.1A) clearly shows a number of discrete well-defined dust clouds everywhere around the cap edge, especially in the lower-left quadrant. By later in the season, the images and the TES data show evidence for accumulation of dust. While the background dust away from this polar accumulation has characteristic 9μm optical depth of between 0.1 and 0.2, inside of the polar region the opacity can be in excess of 0.5. Combined, these data suggest the capability of cap related wind systems to lift significant amounts of dust during these seasons.

4.4 Occurrence and Location of Surface Stresses Sufficient to Initiate Dust Lifting

The spacecraft observations of dust lifting in the polar regions, combined with theoretical arguments which suggest that surface winds should be elevated near the cap edge, provide strong motivation for the study of cap edge dust lifting in a three-dimensional numerical model. The importance of various factors that influence the circulation (and generation of high wind stresses) such as the CO_2 sublimation flow, topography, and the strong thermal contrast created by the cap edge, should also be tested.

The first step in determining whether the model can reproduce observed dust activity near the south polar cap is to check whether the model can produce surface wind stresses of enough strength to initiate dust lifting by the criteria discussed in Section 4.1. To this end, an experiment using Mars MM5 was conducted to simulate surface wind stresses in the south polar region at various points in the mid and late southern spring season. The highest-resolution topography [*Smith et al.*, 1999], thermal inertia [*Vasavada et al.*, 2000], and albedo [*Vasavada et al.*, 2000] datasets available, and output from the GFDL Mars GCM which was tuned to match the observations of atmospheric temperature were employed in the model. The model domain was chosen to be centered on the south pole and extend out to 50° S, with a horizontal resolution of 40 km between grid points. For the simulation at summer solstice, the cap was sufficiently small to warrant embedding another, higher resolution domain, also centered on the south pole, with a horizontal resolution of approximately 13 km and extending out to 76° S. In both domains, there were 12 vertical levels from the surface to 40 km height, with the lowest layer centered at a height of 50 m. The south polar cap used in the L_s 225 simulation is the Mars GCM-predicted cap. However, for the L_s 255, and L_s 270 simulations, the cap is small enough that the latitudinal resolution of the GCM (approximately 300 km) is too large to allow for accurate modeling of the cap shape. In these Mars MM5 simulations, the GCM-predicted cap is overwritten

with a cap defined by Viking images of the south polar cap.

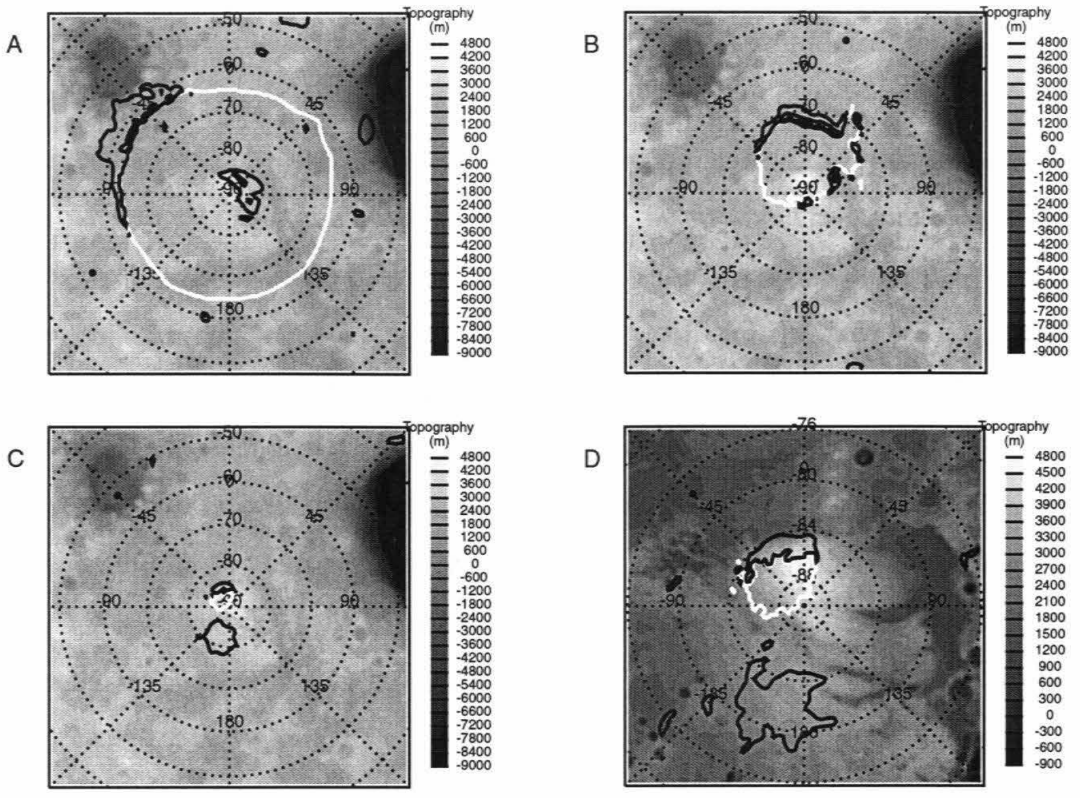

Figure 4.2: Maps of the south polar region used in the mesoscale simulations. Topography is shown by the gray shading in the background. The extent of the seasonal cap is shown by the white line. Surface wind stress is contoured by the thick black lines in intervals of 0.032 Pa. The small black circle is the longitude of local noon. **A:** L_s 225. Local noon is at -120° E. **B:** L_s 255. Local noon is at 15° E. **C & D:** L_s 270 (large and small domains used). Local noon is at -45° E.

The wind stress maps for the three simulations (L_s 225, L_s 255, and L_s 270) are shown in Figure 4.2. In each case, times of day when high wind stresses covered the greatest area were selected. The figures show areas of the surface for which the stress exceeds a value of 0.032 Pa. This value was chosen to be the dynamic stress threshold based on the laboratory assessment of 0.04 Pa as the static stress threshold for saltation. The value corresponds to those used in some studies [*Iversen et al.*, 1976; *Anderson et al.*, 1999], as well as being in

the midrange of values derived from others [*White*, 1979; *Greeley et al.*, 1980]. The static threshold is the stress required to initiate motion of sand-sized particles. The dynamic threshold is the stress necessary to sustain motion after it has been initiated. The dynamic threshold is roughly 80% of the static value based on observations [*Bagnold*, 1941]. The dynamic threshold was chosen for use on the assumption that sub-grid scale winds will exceed the static threshold in grid boxes where the dynamic threshold is exceeded (and that if the static threshold is exceeded by gusts in a grid box whose average wind stress does not exceed the dynamic value, any dust lifted will quickly dissipate). In three seasonal cases examined, significant areas of the model domain exceed the chosen threshold. In fact, if 0.04 Pa had been chosen, much of these areas would still have exceeded threshold.

The three seasonal dates for which simulations were conducted, L_s 225, L_s 255, and L_s 270, were chosen for two primary reasons. First, the different dates correspond to different extents of the seasonal ice cap, from extensive and nearly circular at L_s 225, to approximately the residual extent at L_s 270. Second, the observations show that in the midspring season, there was significant discrete cap edge storm behavior, while a build-up of dust in the polar regions occurred after L_s 255. Thus the observations suggest that this set of simulations should provide a range of polar dust lifting behavior. In the following paragraphs the results of the simulations are described in seasonal order. Given that the simulations exhibit a great deal of time variability, it is not possible to capture this range of behavior in figures. This variability is mostly with respect to variations in local time; day-to-day variations (throughout the extent of the model run) in location and extent of regions of high wind stress are negligible. However, to provide some idea of the occurrence and behavior of dust lifting Figure 4.2 shows representative time snapshots of the simulations. Note that the term "lifting" will be used in this section to denote occurrences of surface wind stresses exceeding the dynamic threshold.

For L_s 225, the simulation shows a great deal of lifting along the cap edge (Figure 4.2A). Lifting occurs at all longitudes at some point during the day. Right at the cap

edge, lifting is roughly in phase with the sun, with significant cap edge lifting occurring generally between the local times of approximately noon and 6 PM. In these cases lifting occurs right at the very edge of the cap. However, significant lifting also occurs during the night and morning in certain longitude regions. Specifically, significant non-afternoon lifting occurs in the region between -30° E and -60° E within 10° of the cap edge, and in the region between 45° E and 90° E between 2° and 10° from the cap edge. Between 90° E and 135° E significant lifting occurs right at the cap edge and extending out by over 15° beginning at 6 AM local time and continuing to approximately 7 PM.

A major qualitative change in the behavior of dust lifting occurs between the L_s 225 and L_s 255 simulations (Figure 4.2B). Lifting no longer occurs at every longitude at least once during the day. Lifting is now present primarily at the immediate cap edge between 60° E and -90° E. This may be related to the fact that the cap is no longer circular. Lifting occurs between the local times of 7 AM and 10 PM, with maximal extent during the early afternoon. Small areas of additional lifting occur on the polar layered terrains, centered at 180° E between 7 PM and midnight, and in a "bay" of defrosted ground surrounded by seasonal ice cap on three sides, at 60° E and 82° S, with lifting occurring at all times during the day. In addition, a small but persistent region of dust lifting is in Chasma Australe in predawn morning (approximate 4 AM). This dust lifting is likely associated with nighttime drainage flow off the seasonal cap.

By L_s 270 the region of cap edge lifting has shrunk to between 0° E and -45° E (Figures 4.2C and 4.2D). The cap in this simulation is essentially the residual cap. Lifting occurs centered on the afternoon hours, as in the earlier seasonal date simulations, but for a small range of local times, between 10 AM and 5 PM. Strongest stresses during this period occur around local noon. However, a secondary lifting period occurs during the night, between the hours of 8 PM and 5 AM. Combined, these two periods constitute more than two-thirds of the day during which stresses are above threshold. During this period, another location of lifting occurs over the polar layered terrains, centered on 180° E and

extending from -135° E to 135° E. Lifting occurs during the early morning predawn hours of approximately 2 AM to 6 AM. This region is slightly larger than was active in the L_s 255 period. This region was covered by the seasonal cap during the L_s 225 simulation, and was therefore inactive.

4.5 Causes of High Surface Wind Stresses

Having determined that the critical stress is exceeded, experiments designed to examine which components of the dynamical system (slopes, thermal contrast, thermal tides, etc.) are dominant in generating the high wind stresses were conducted. In order to isolate dynamical forcings, simulations were designed in which the CO_2 sublimation flow was deactivated, the thermal effects of the cap were removed (i.e., ice and differences in thermal inertia and albedo), the topography of the south polar region was flattened, and finally a simulation in which both the topography was flattened and the thermal effects of the cap were removed. Because of the large number of simulations required to elucidate dynamical processes, these simulations were undertaken at only one seasonal date. As the midspring simulation is likely dominated by the great areal extent of the seasonal cap and the thermal effects of the cap edge, we decided to concentrate on the solstitial period where the effect of topography should be greatest. Again, in this section, the term "lifting" will be used to denote occurrences of surface wind stresses exceeding the dynamic threshold.

For the simulation in which the CO_2 sublimation flow (the flow of air away from the polar cap due to sublimation of the CO_2 ice) was deactivated, essentially no change in the occurrences and areal extent of regions of dust lifting were observed. This can be seen by comparing Figures 4.3A and 4.3B. At this season it would appear that the condensation flow is not particularly important in generating large surface winds.

The effect of the thermal contrast between the cold, bright cap and the warmer, darker, defrosted surrounding terrain should give rise to a "sea breeze" circulation at the cap edge.

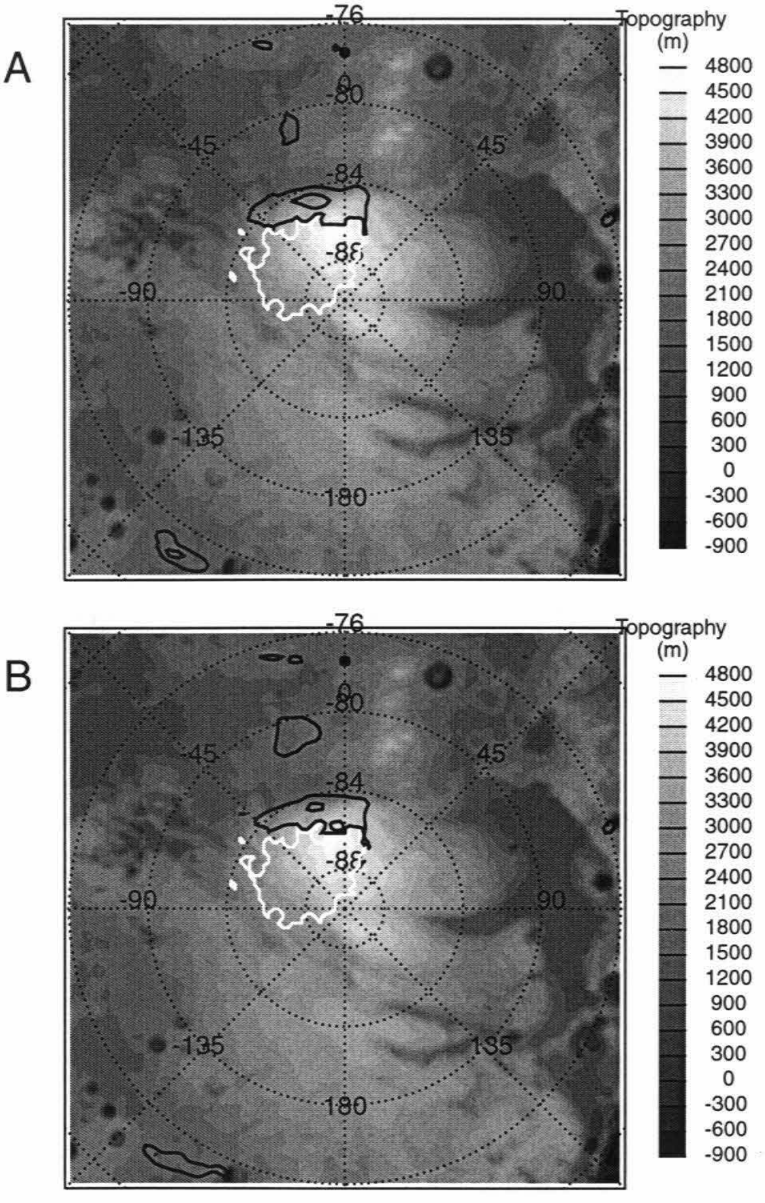

Figure 4.3: Wind stresses in the south polar region at L_s 270. Topography is shown by the gray shading in the background. The extent of the seasonal cap is shown by the white line. Surface wind stress is contoured by the thick black lines in intervals of 0.032 Pa. The small black circle is the longitude of local noon, in this case, 0° E. **A:** "Base" simulation. **B:** Simulation where the surface covering of CO_2 ice has been removed

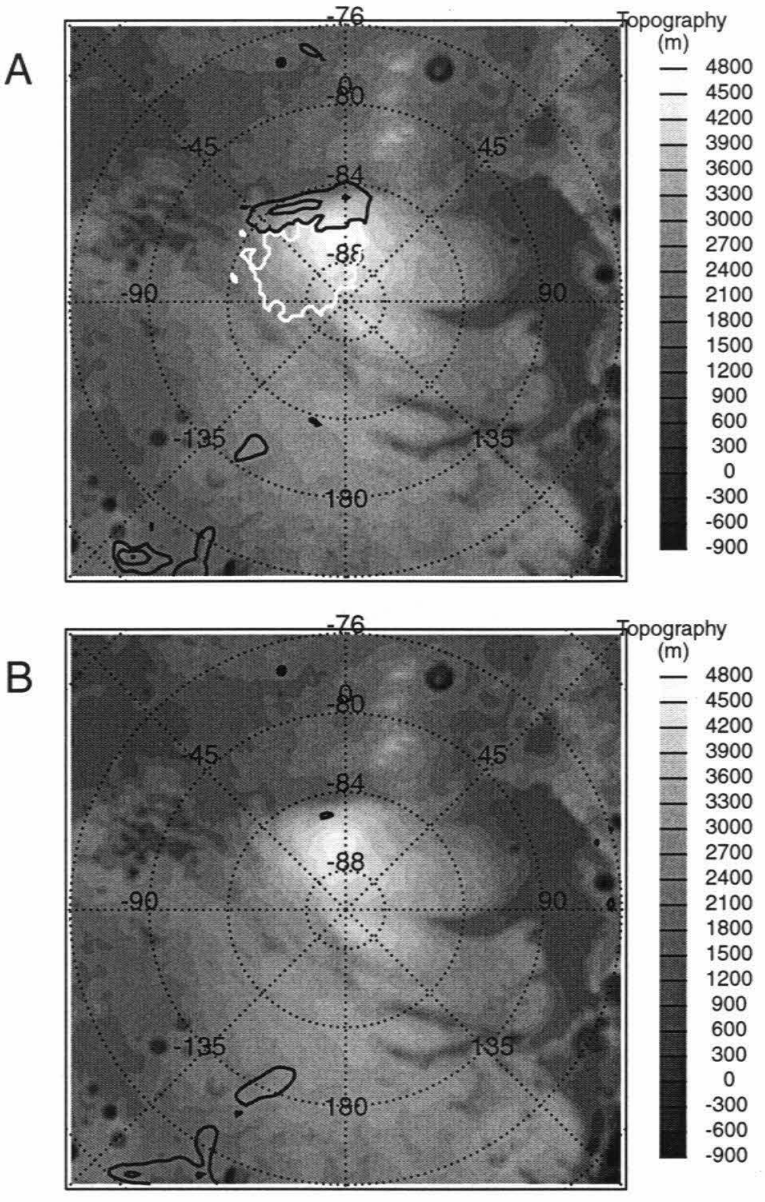

Figure 4.4: Wind stresses in the south polar region at L_s 270. Topography is shown by the gray shading in the background. The extent of the seasonal cap is shown by the white line. Surface wind stress is contoured by the thick black lines in intervals of 0.032 Pa. The small black circle is the longitude of local noon, in this case, -15° E. **A:** "Base" simulation. **B:** Simulation where the thermal effects of the residual cap (i.e., CO_2 ice, thermal inertia and albedo signature) have been removed.

The importance of this direct thermal contrast is examined by eliminating the cap thermal signature. This was accomplished by first removing the surface CO_2 ice and second, replacing the polar cap thermal inertia and albedo values with the average of the surrounding terrain. A snapshot of the results are shown in Figure 4.4 in comparison with the "base" case. Cap edge lifting is almost entirely eliminated (although note that there is still some lifting in regions well removed from the cap edge), reinforcing the idea that these winds are directly related to the thermal contrast. One very slight exception is provided by the region of strongest slope on the edge of the layered deposits between 0° E and -45° E. At approximately local noon a short period (approximately 2 hours) of lifting occurs, likely associated with strong upslope winds. Winds away from the immediate vicinity of the cap are largely unaffected by the removal of the cap thermal signature. This suggests that the high wind speeds and wind stresses are being controlled by a forcing different than thermal contrast.

A further simulation was conducted whereby the topography was flattened uniformly in the south polar region to a height of 0 km (the MOLA reference elevation). The thermal effects of the cap were present in this simulation along with spatial variations in albedo and thermal inertia throughout the model domain. Figure 4.5 shows the comparison between this simulation and the "base" case. The cap edge lifting occurring at the region of maximum slope now disappears (Figures 4.5A and 4.5B). A new location of cap edge lifting occurs between 0° E and 45° E, during the period between 9 AM and 2 PM (Figures 4.5C and 4.5D). Surprisingly, the region of lifting over the polar layered terrains is still present. Inspection of the wind field at this time shows that the high stresses may be due to constructive interference of a wind generated by the diurnal tide and winds circulating around a quasi-stationary cell centered between Hellas Basin and the polar cap (Figure 4.6). This suggests that these stresses are not associated with the general regional slope of the layered deposits, but rather represent the long-range effect of the Hellas Basin.

Finally, in order to determine whether the peak stresses over the layered deposits are

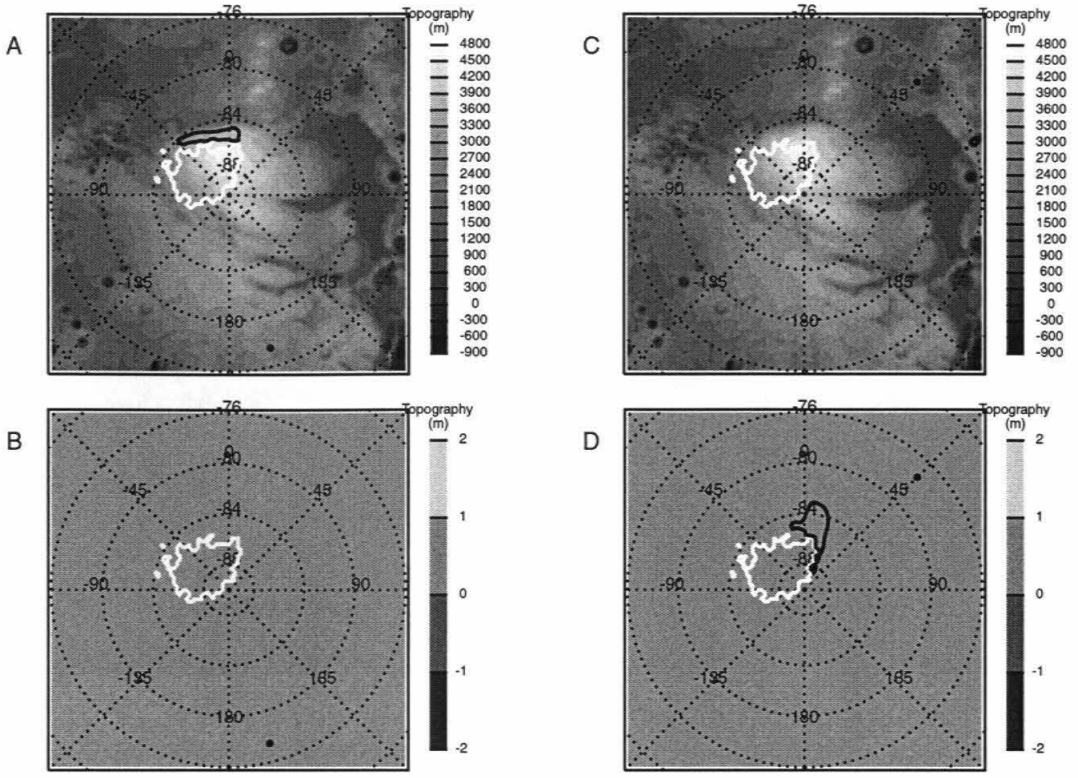

Figure 4.5: Wind stresses in the south polar region at L_s 270. Topography is shown by the gray shading in the background. The extent of the seasonal cap is shown by the white line. Surface wind stress is contoured by the thick black lines in intervals of 0.032 Pa. The small black circle is the longitude of local noon. **A:** "Base" simulation. Local noon is at 165° E. **B:** Simulation with no topography, highlighting the loss of cap edge lifting between 0° E and -45° E at the same instant of time as **A**. **C:** "Base" simulation. Local noon is at 45° E. **D:** Simulation with no topography, highlighting the new area of cap edge lifting between 0° E and 45° E that is not seen at the same instant of time as **C**.

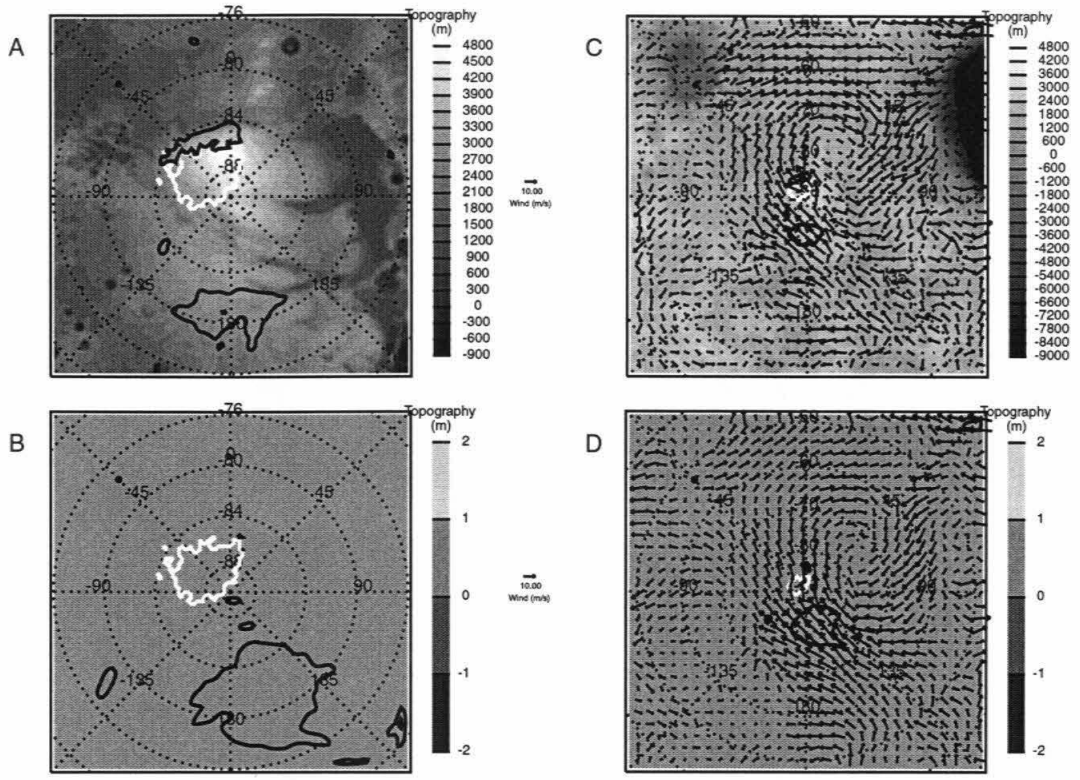

Figure 4.6: Wind stresses in the south polar region at L_s 270. Topography is shown by the gray shading in the background. The extent of the seasonal cap is shown by the white line. Surface wind stress is contoured by the thick black lines in intervals of 0.032 Pa. The small black circle is the longitude of local noon, in this case, -45° E. **A:** "Base" simulation. **B:** Simulation with no topography, showing the persistence of lifting over the polar layered terrain, even though the region slope associated with this terrain is now absent. **C:** "Base" simulation showing the wind vectors at the instant of time shown in **A** & **B**. A stationary eddy centered at 75° S and 30° E can be seen. **D:** Simulation with no topography showing the wind vectors at the same instant of time as **A** & **B**. The stationary eddy still remains, although the wind vectors are smoother in directional coherence due to the lack of modification by topography. Even though the topography is flat, the influence of Hellas is still being felt through the GCM-derived boundary conditions, which were generated from a GCM simulation without flattened terrain.

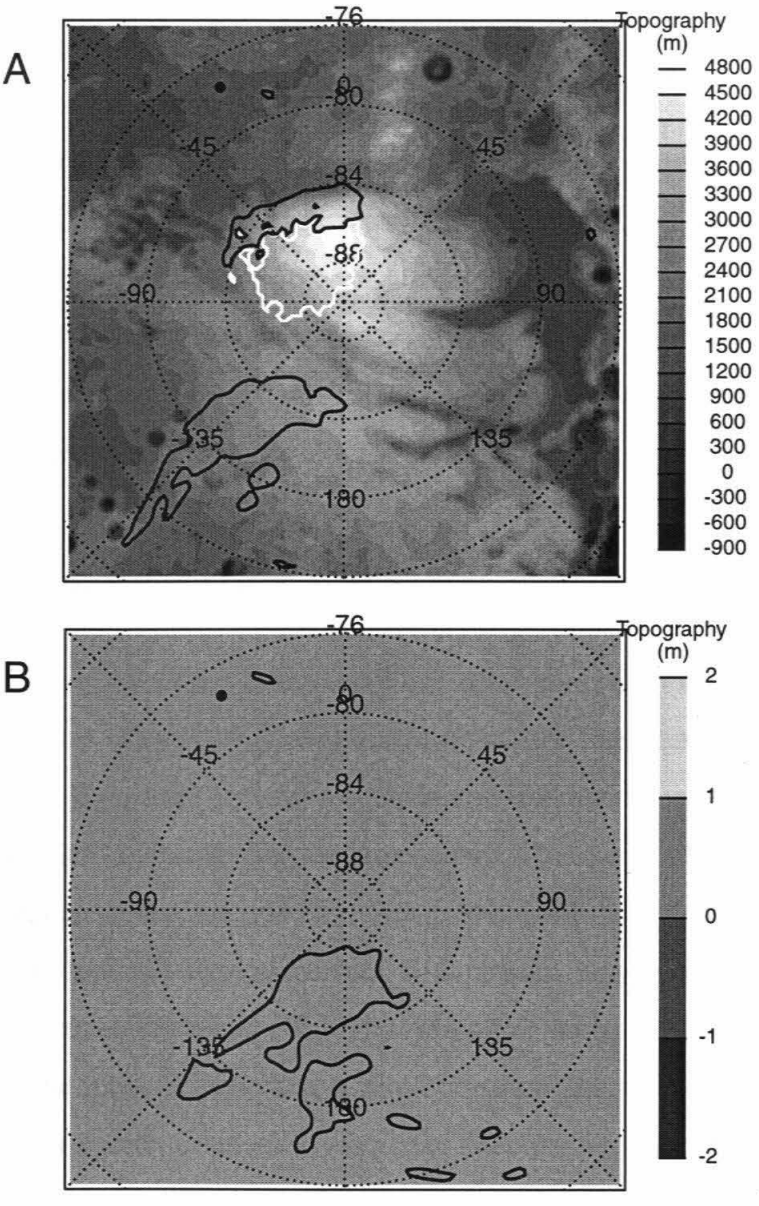

Figure 4.7: Wind stresses in the south polar region at L_s 270. Topography is shown by the gray shading in the background. The extent of the seasonal cap is shown by the white line. Surface wind stress is contoured by the thick black lines in intervals of 0.032 Pa. The small black circle is the longitude of local noon, in this case, -30° E. **A:** "Base" simulation. **B:** Simulation with no topography and no thermal effects of the cap (CO_2 ice, thermal inertia or albedo signature). Cap edge lifting is gone, but other areas remain, as discussed in the text.

truly unrelated to local forcing (from the cap thermal contrast and the slope of the polar layered terrain), a simulation was run in which the values of local topography, albedo and thermal inertia throughout the domain were set to uniform values. The only remaining source of zonal asymmetry comes from the boundary conditions supplied from the GCM (which included large scale variations in topography, thermal inertia, and albedo). In this simulation the only remaining region of lifting occurs in the region between -135° E and -180° E, and north of 76° S (Figure 4.7). The wind pattern at this location is very similar to that in the previous simulation. Clearly, this lifting is unassociated with the polar cap or high polar latitudes, and appears to be more closely related to the large scale topography.

4.6 Dust Feedback on Dust Lifting

So far, surface wind stresses have been examined in isolation from any potential feedback between the radiative effects of lofted dust and the surface winds. The question of whether dust lifting events involve significant positive feedback is an important one within the context of dust storm generation. In this section the atmospheric injection of dust in the model is coupled to the prediction of surface wind stresses in excess of the dynamic threshold. Atmospheric heating due to dust is already included in the model. Any impact of the lofted dust on the surface stresses is examined. The prescription of dust injection is relatively simple: if the surface wind stress in a grid box is above threshold, a surface-to-lowest-level dust flux is augmented. In a given simulation, the rate of injection while the stress is above threshold is constant. This is likely not what happens in reality, i.e., higher stresses inject more dust, but this relation was chosen a simple first approximation. As mentioned in Section 4.2, the GFDL Mars GCM and the Mars MM5 prescribe a background dust injection rate in order to maintain a background distribution of dust necessary to match observations of air temperatures. In the Mars MM5 simulations described in this section, when the threshold is exceeded, dust is injected at a rate of between 100 and 1000 (depending upon

the simulation) times this background rate. If the injection rate was too high, the entire domain filled with dust, up to optical depths of 10 or more, producing obviously unphysical situations (the optical depths observed were less than 1 in the 9 μm region, corresponding to visible values of 2 to 2.5). Only in these extreme simulations, was any positive feedback on dust lifting observed.

Figure 4.8 shows snapshots of simulations at L_s 225 both without and with dust injection. The background gray shading shows the optical depth of the atmosphere, and the black lines show regions where the wind stress exceeds 0.032 Pa. The regions of high stress are the sites where small dust clouds develop in Figure 4.8B. Wisps of dust trail away from these locations and filamentary dust clouds from previous injection events abound within the domain. Some amount of the injected dust is blown over the seasonal ice cap. While the very fine structure of the clouds observed in the MOC image (Figure 4.1A) is not apparent, this primarily results from the limitations of resolution. Dust is seen at most longitudes around the cap, as seen in the MOC image (Figure 4.1A). The presence of the thick dust clouds does not significantly alter the peak values or areal extent of the regions of high wind stress.

The dominant pattern of dust injection and transport at L_s 255 (Figure 4.9B, compared to Figure 4.9A) is that of the daily injection of dust along the cap edge between 60° E and -90° E. These daily bands of dust are advected by the circulation resulting in concentric filamentary structures. There is some evidence in the MOC image (Figure 4.1B) for such multiply banded filamentary structures. However, the accumulation of dust in the 120° E to 180° E region over the polar layered terrain does not develop, as was observed in the MOC image. Again, the presence of the thick dust clouds does not significantly alter the peak values or areal extent of the regions of high wind stress.

The extent of regions of dust lifting has shrunk by L_s 270. In the simulation with dust injection, more dust is seen over the polar region (Figures 4.10C and 4.10D) than in the simulation without (Figures 4.10A and 4.10B), while the regions away from the cap

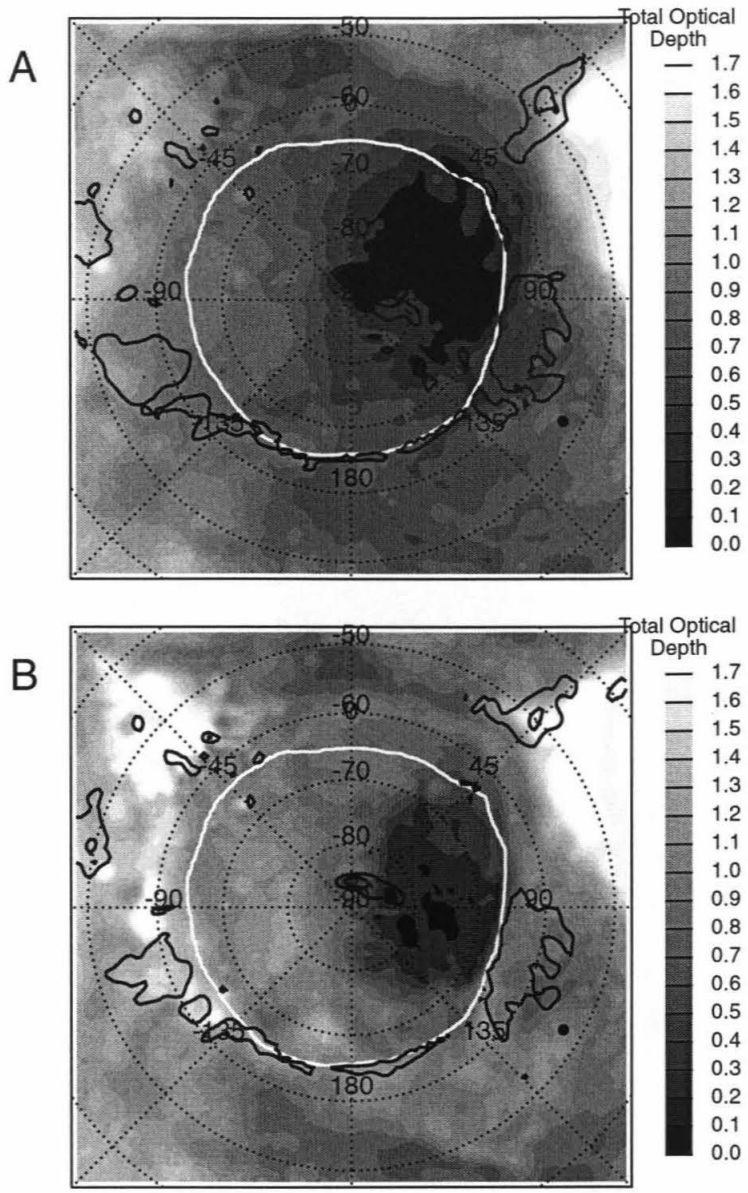

Figure 4.8: Wind stresses and optical depth in the south polar region at L_s 225. Optical depth is shown by the gray shading in the background. The extent of the seasonal cap is shown by the white line. Surface wind stress is contoured by the thick black lines in intervals of 0.032 Pa. The small black circle is the longitude of local noon, in this case, 120° E. **A:** "Base" simulation. **B:** Simulation with dust feedback. Small dust clouds (of high optical depth) can be seen near the cap edge. The large dusty areas to the upper left and upper right of the figure are Argyre and Hellas Basins being filled with dust.

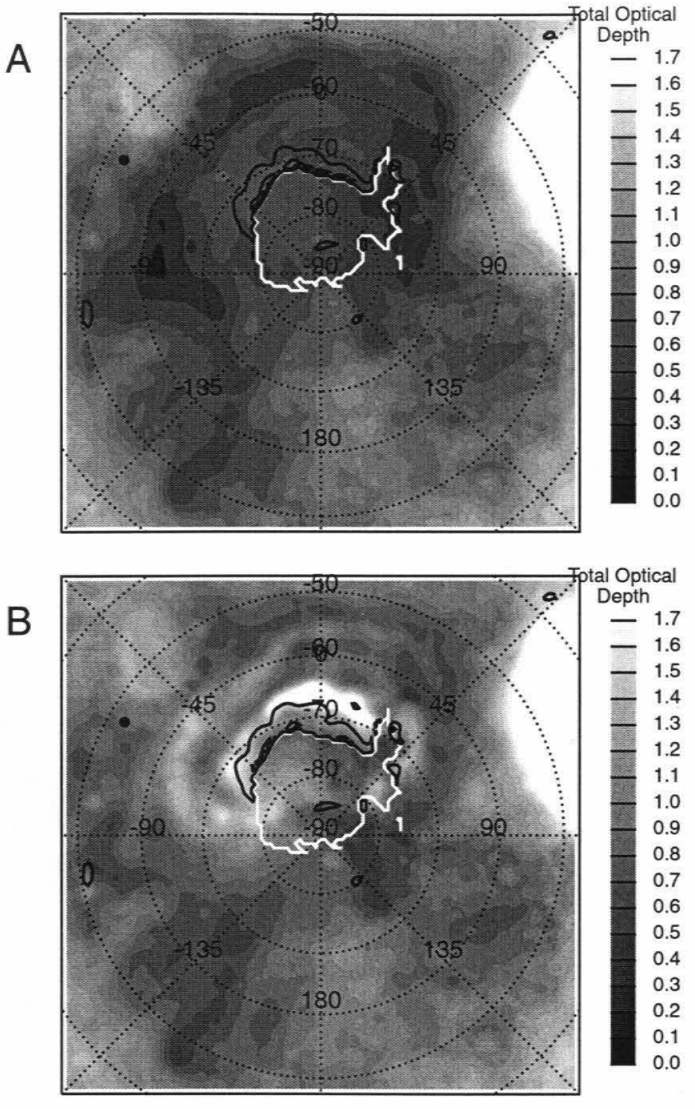

Figure 4.9: Wind stresses and optical depth in the south polar region at L_s 255. Optical depth is shown by the gray shading in the background. The extent of the seasonal cap is shown by the white line. Surface wind stress is contoured by the thick black lines in intervals of 0.032 Pa. The small black circle is the longitude of local noon, in this case, -60° E. **A:** "Base" simulation. **B:** Simulation with dust feedback. Dust clouds of high optical depth are being created at the edge of the cap, and the previous day's cloud can be seen slightly northward of the cap, although being less optically thick. Typically only two "filaments" of dust clouds like this are seen at one time; they are created once every day, and the decay of the cloud back to background levels of optical depth takes about one day.

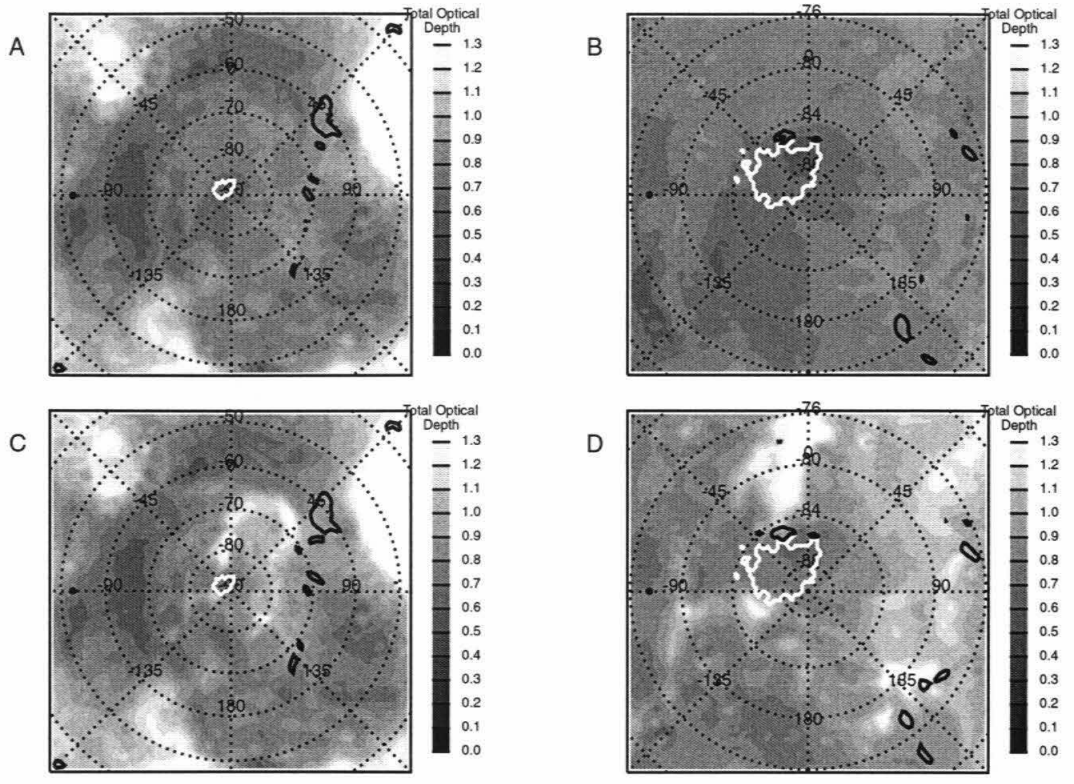

Figure 4.10: Wind stresses and optical depth in the south polar region at L_s 270. Optical depth is shown by the gray shading in the background. The extent of the seasonal cap is shown by the white line. Surface wind stress is contoured by the thick black lines in intervals of 0.032 Pa. The small black circle is the longitude of local noon, in this case, -90° E. **A & B:** "Base" simulations, the large and smaller, nested domains respectively. **C & D:** Simulation with dust feedback, for the large and smaller, nested domains respectively. Dust clouds of high optical depth are being created at the edge of the cap between 0° E and -45° E, being advected northward, and getting entrained in the stationary eddy. Previous days' dust clouds can be seen roughly forming a circle between the cap and 60° S, and between 0° E and 45° E. Comparing **A** to **B**, and **C** to **D**, shows that the areas of high wind stress are not affected by the dust feedback.

(north of about 70° S) show about the same amount of dust. Using the same dust injection rate as used in the L_s 255 simulation discussed above, fewer and smaller dust clouds are generated as compared to that period. Dust is primarily injected at the cap edge and over the polar layered terrain. Dust clouds move away from the cap after generation, but are mostly caught in the stationary low pressure eddy between Hellas Basin and the cap, where they circulate and eventually dissipate during the model simulation (Figure 4.10C). Dust clouds decay to the background level of optical depth in about one day.

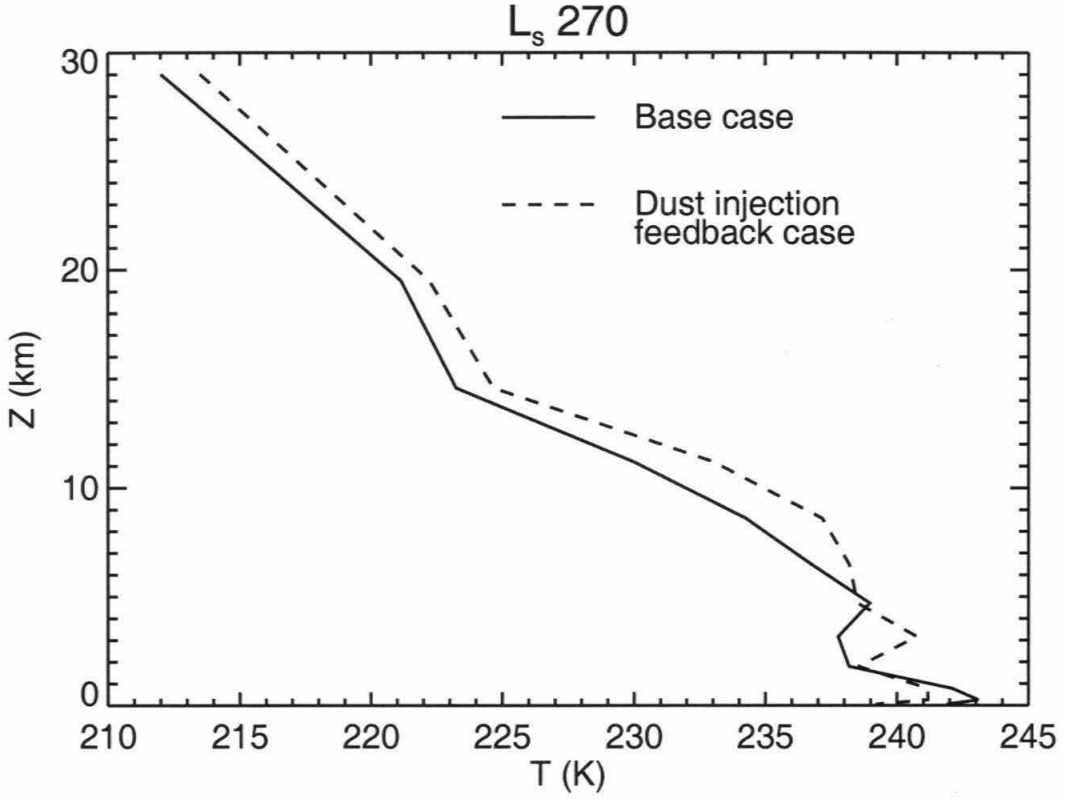

Figure 4.11: Graph of air temperature at the same physical location (78.1° S and -5.8° E) and same instant of time as a function of height for the L_s 270 simulations. The base case is shown as the solid line, and the case where large amounts of dust are injected in high wind stress areas is shown by the dashed line. The large dust cloud in the dust feedback simulation modifies the vertical temperature structure and increases the temperature by a few K above 2 km, while decreasing temperature below that height.

In all of the seasonal cases described above, there is no consistent evidence for positive feed back on dust lifting, as gauged by examination of the areal extent of the regions of high wind stress. The simulations were carried out for 10 Mars days, and at the end of that period, the dust injection simulations produced nearly identical surface wind stress patterns to those in the "base" cases. The similarity of surface wind stress patterns between the "base" cases and the "feedback" simulations can be seen in Figures 4.8, 4.9, and 4.10. The fact that the extra injected dust is indeed modifying the atmospheric thermal structure, while leaving the surface wind stresses alone is shown in Figure 4.11. The presence of the dust is having a radiative effect, but this does not affect the dynamical structure with respect to altering the surface wind stresses. Thus it would appear for the case of dust lifting near the south polar cap during the late spring season, which primarily results from cap thermal contrasts and slope winds, that radiative dynamical feedbacks are not particularly important in the maintenance and generation of local dust storms.

4.7 Conclusions

Mesoscale atmospheric simulations of the Martian high-latitude southern hemisphere during late spring have shown the occurrence of surface wind stresses in excess of the critical saltation-initiating value at a variety of locations and local times. The late southern spring period was focused on because of the availability of high quality observations from the Mars Global Surveyor spacecraft, both from MOC images and from 9 μm dust opacities derived from TES observations. These data show dust activity near and over the cap, and at the cap edge during this season.

The mesoscale simulations readily generate surface wind stresses that exceed minimum saltation threshold in the regions where dust activity is observed in the MGS data during similar seasonal dates. Many, but not all, of these regions correspond to the immediate cap edge region. In this paper cap edge wind systems are specifically examined. During

the L_s 225 simulation, high wind stresses are observed all around the cap edge during local afternoon hours. The L_s 255 and L_s 270 simulations show high wind stresses more restricted in physical location, although peak wind stresses still occur during the local afternoon hours. The L_s 270 simulation also begins to show significant nighttime high wind stresses, in the same location that was active during afternoon hours in the L_s 255 and L_s 270 simulations.

By eliminating forcing elements from the model, the important dynamical modes generating the high wind stresses at this season were isolated. The cap edge thermal contrast with ice-free bare ground provides the primary drive for high surface wind stresses in the cap edge region. In some locations topographic slopes augment these cap edge winds. Sublimation flow due to the seasonal shrinking of the cap does not appear to play an important role, at least during late southern spring. The presence of high wind stresses over the polar layered terrain at certain local times is still observed even when the topography of the south polar region is completely removed. Thus, local slope winds cannot be the primary cause of generating the wind stresses during this season. Further examination shows that the high wind stresses are due to a constructive interference of winds generated by the solar thermal tide and winds circulating around a stationary eddy sitting between Hellas Basin and the polar cap. The extent and persistence of these high wind stress events strongly suggest that such regional scale wind systems should be examined for a variety of seasons in future studies.

Further simulations in which the presence of high wind stresses are linked causally to the injection of large dust loads produce similar dust activity and dust cloud morphology to that observed in the MGS data at similar seasonal dates. No evidence for consistent positive or negative feedback from the radiative effects of dust clouds thus created is observed on the surface wind stress fields in the simulations during this season.

4.8 Speculations

This paper has shown that dust lifting by mobilization of sand-sized particles will adequately model the observed cap edge storms. The issue of whether sand is available is really beyond the scope of this paper. However, since the winds at a given location, especially at the south polar cap edge examined in this paper, are generally blowing in the same direction during periods of high wind stress, it seems to rule out the notion that the sand blows back and forth to be available wherever new dust is derived by atmospheric settling. It is possible that a supply of sand was created in a different regime in the past, and that therefore the process observed today will eventually stop. It is also possible that during devolitilization sand-sized clots form from the dust.

It is interesting to consider direct lofting of fine particles. Higher stresses are needed to loft the smaller particles [*Greeley et al.*, 1992]. In the same way that the use of the dynamic threshold for particle mobilization (i.e., stronger wind gusts within the grid box already having surpassed the static threshold) was justified, it is possible that stronger wind stresses can occur within the grid box and can locally initiate the mobilization of dust-sized particles.

However, due to the high wind stresses necessary to directly mobilized dust-sized particles, five different mechanisms have been suggested which may help to inject dust into the atmosphere [*Greeley et al.*, 1992]:

1. the presence of triggering particles, i.e., saltation of sand-sized particles;

2. clumping of fine grains to produce particles of sand size, which then break back into dust size upon impact with each other or other obstacles;

3. lessening the threshold wind stress necessary to mobilize any given particle due to effects such as unstable atmospheric conditions (due to interparticle or electrostatic forces on the particles);

4. small convective vortices (i.e., "dust devils"), which have strong winds and large pressure gradients which allow for the dust to be mobilized directly;

5. "fountaining" of dust particles due to devolitilization of $CO_2$and water in or on the surface.

The first two mechanisms have been encompassed within the scope of this paper. The third mechanism, reduction of threshold stress, could also be encompassed, but primarily enlarges the range of particle sizes that can be mobilized for a given stress. Threshold stresses can be reduced by the presence of other forces giving extra lift to particles. Unstable atmospheric conditions, where the environmental temperature decreases with height faster than the adiabatic lapse rate (g/c_p), produces thermal turbulence in addition to the mechanical turbulence normally associated with the near-surface boundary layer. This thermally-derived turbulence provides extra lift to the particle that is not measured in the thermally stable atmospheric environment of the laboratory wind tunnel experiments. The work of *White and Greeley* [1989] suggests that unstable atmospheric conditions reduce the threshold stress value by 40 to 65%. This would allow mobilization of particles as small as 25 μm for the same stress threshold used in this study (0.032 Pa), as compared to particles of only approximately 100 μm without this enhancement. Using the highest stresses seen in the simulations, and applying the threshold reduction, mobilization of particles as small as 10 μm is possible. This is now at the upper edge of the airborne dust particle distribution. The presence of electrostatic forces can also reduce the threshold stresses if the repulsion between particles (or attraction to already suspended particles) is significant. Electrostatic forcing has been measured with respect to terrestrial aeolian activity [*Schmidt et al.*, 1998], and found to be of the order of gravitational forces, but laboratory measurements under Martian conditions have not been conducted. Thus the effect of electrostatic forces on the direct mobilization of dust-sized particles is difficult to quantify.

The fourth mechanism, dust devils, is clearly the work of a future separate study. There

exists much observational evidence of dust devils on Mars [*Thomas and Gierasch*, 1985; *Ryan and Lucich*, 1983; *Metzger et al.*, 1999; *Schofield et al.*, 1997], and they are seen almost everywhere on the planet. Dust devils are generated under thermally unstable atmospheric conditions, but the necessary conditions for producing Martian dust devils is not known. Deriving a threshold for the generation of dust devils (either theoretically or empirically), examining where that threshold is exceeded, and then determining the forces creating the threshold condition, in a way similar to this study, would also help determine which process of dust lifting is more dominant at a given location and time.

The final mechanism, ejection of dust particles from the sublimation or explosive eruption of surface volatiles [*Johnson et al.*, 1975; *Huguenin et al.*, 1979; *Greeley and Leach*, 1979], may also operate, especially near the retreating cap edge where there is a large available quantity of volatile material. This mechanism may also operate in connection with second mechanism, where during the process of devolitilization, sand-sized clots are formed from dust particles.

These are merely speculations on alternative mechanisms. The first two have been examined in this work, and the role of the third can be considered in conjunction with the first two. However, the final two are entirely different areas of investigation which would require large separate studies which are outside the scope of this paper. It is possible, and indeed likely, that all of these mechanisms are acting to generate dust lifting near the south polar cap in late southern spring and southern summer solstice.

5 Summary

Presented below is a summary of the conclusions from the major chapters.

5.1 Seasonal Variation of Aerosols

Rederivations of the 9 μm optical depths from the Viking Infrared Thermal Mapper data are compared with measurements of visible opacity from the Viking Landers. The ratio of visible to infrared opacity, which is typically assumed to be constant, varies significantly with season. Both the visible and infrared opacities are usually assumed to relate only to the dust amount in the atmosphere. Two potential explanations for the opacity ratio variations involve only variations in the dust properties. The first argues that variations in dust particle sizes affect the ratio, but this can only explain less than half the range in the derived opacity ratios, and even these variations do not appear to be reasonable based on Mars Global Surveyor (MGS) Thermal Emission Spectrometer (TES) observations, while such high ratios of visible-to-infrared dust opacity would result in an unrealistic atmospheric temperature structure and circulation. The second potential explanation argues that if dust is confined low in the atmosphere, the true infrared dust opacity would be underestimated. In this case the true opacity ratio would remain constant, but would appear to vary due to errors in the infrared opacity calculation. However, this explanation is only able to account for less than 10% of the peak opacity ratio variation, even for dust confined to an unrealistically shallow column.

The most likely explanation for variations in the opacity ratio is the previously neglected role of persistent water ice hazes and clouds during northern spring and summer. The implication here is that the Viking-derived visible and infrared optical depths are not

representative of the seasonal cycle of dust, but of the combined cycles of dust and atmospheric water ice. Thus, Mars is less dusty and more cloudy than was believed on the basis of Viking Lander (VL) observations, especially during the northern spring and summer seasons. The variations in dust and water ice opacities appear to be strongly anticorrelated. The ice amounts peak in early norther summer (with the opacities possibly peaking earlier at VL1 than at VL2), while the dust opacity is a minimum at these times. In addition, the ratio of optical depth in the infrared to the visible is likely to lie near 2.5 and that consequently, models which use this constant value are likely not in error.

5.2 A Martian Mesoscale Model

A terrestrial atmospheric mesoscale model, the Pennsylvania State University/National Center for Atmospheric Research Fifth Generation Mars Mesoscale Model (MM5), was converted for use on Mars using the Mars-specific physical parameterizations of the Geophysical Fluid Dynamics Laboratory (GFDL) Mars General Circulation Model (GCM). Output from the GFDL Mars GCM is used to initialize and drive (i.e., provide time-evolving boundary conditions for) the Mars MM5.

The Mars MM5 is found to accurately capture most of the structures generated in the GCM, when the Mars MM5 domain is essentially global. This fidelity extends even to the reasonable simulation of the three-dimensional distribution of dust, which involves detailed radiative and dynamical feedback systems. The one caveat is the limitation of Hadley flow imposed by the finite model height and the rigid lid. The finite model height and rigid lid are fundamental structures of the model, and therefore cannot be removed, but their effect can be taken into consideration when designing experiments where the Hadley flow is important.

Near-surface air temperatures measured by the two Viking Landers and Mars Pathfinder are relatively well-simulated for all seasons examined. Small differences in comparison

suggest either small errors in the thermal inertia used, or the lack of treatment of slopes in the calculation of absorbed insolation.

The Mars MM5 faithfully reproduces the variations in surface pressure generated by the GCM, and the fact that they are reproduced so faithfully suggests that the coupling of the Mars MM5 to the GCM through the time-evolving boundary conditions is well-implemented.

Wind directions for all the landing sites and for all seasons are relatively wellreproduced. In most cases, the Mars MM5 variation in wind directions is not greatly different from that generated by the GCM. This suggests that control of wind directions is provided by the global tide as modified by topography on a scale greater than a few hundred kilometers. The wind directions provided by the GCM are reported for a height of roughly 200 m above the surface, and that consequently there appears to be little rotation in the lower boundary layer.

Peak wind speeds at all locations and all seasons are systematically underpredicted. Furthermore, the phasing of wind speed as a function of local time is not well-reproduced for any landing site, except for Viking Lander 2 in winter. In order to generate daily variations in wind speed comparable to those observed, the vertical diffusivity was increased by a factor of 10 over the empirically (and terrestrially) derived value used in the model. However, there is precedent in previous work for vertical diffusivities on Mars being of order 10 times larger than on the Earth [*Ye et al.*, 1990].

A significant result is the suggestion that the global tide is at least as important as local slope in generating the variability of winds. Indeed, at Mars Pathfinder and Viking Lander 2, slopes on a scale smaller than that of the GCM grid spacing (a few hundred kilometers) are not particularly important. A more detailed study of the tides generated in the GCM and passed to the Mars MM5, the interaction of these tides with topography, and the sensitivity of the tides to the three-dimensional distribution of dust needs to be undertaken to investigate and confirm this result.

The Mars MM5 promises to be a powerful tool for the investigation of processes central to the Martian climate on scales from hundreds of kilometers to tens of meters.

5.3 Dust Lifting at the South Pole of Mars

Mesoscale atmospheric simulations of the Martian high-latitude southern hemisphere during late spring have shown the occurrence of surface wind stresses in excess of the critical saltation-initiating value at a variety of locations and local times. High quality observations from the Mars Global Surveyor spacecraft, both from Mars Orbiter Camera images and from 9 μm dust opacities derived from TES observations, show dust activity near and over the cap, and at the cap edge during this season.

Under the assumption that dust injection is related to the movement of sand-sized grains or aggregates, the generation of surface winds stresses of sufficient strength to mobilize sand-sized particles is investigated. The mesoscale simulations readily generate surface wind stresses that exceed minimum saltation threshold in the regions where dust activity is observed in the MGS data at similar dates. Many, but not all, of these regions correspond to the immediate cap edge region. During the L_s 225 simulation, high wind stresses are observed all around the cap edge during local afternoon hours. The L_s 255 and L_s 270 simulations show high wind stresses more restricted in physical location, although peak wind stresses still occur during the local afternoon hours. The L_s 270 simulation also begins to show significant nighttime high wind stresses, in the same location that was active during afternoon hours in the L_s 255 and L_s 270 simulations.

By eliminating forcing elements from the model, the important dynamical modes generating the high wind stresses at this season were isolated. The cap edge thermal contrast with ice-free bare ground provides the primary drive for high surface wind stresses in the cap edge region. In some locations topographic slopes augment these cap edge winds. Sublimation flow due to the seasonal shrinking of the cap does not appear to play an important

role, at least during late southern spring. The presence of high wind stresses over the polar layered terrain at certain local times is still observed even when the topography of the south polar region is completely removed. Thus, local slope winds cannot be the primary cause of generating these wind stresses during this season.

Further simulations, in which the presence of high wind stresses are linked causally to the injection of large dust loads, produce similar dust activity and dust cloud morphology to that observed in the MGS data at similar seasonal dates. No evidence for consistent positive or negative feedback from the radiative effects of dust clouds thus created is observed on the surface wind stress fields in the simulations during this season.

5.4 Future work

The Viking mission provided unique combination of tracking the optical depth of the Martian atmosphere for a several years at two wavelengths. Since that time, the Mars Pathfinder lander has provided measurements of visible optical depth, but the relative short length of the mission (less than one season) prevents it from being useful as a measure of the annual cycle of dust. The Mars Global Surveyor Thermal Emission Spectrometer has provided global mapping of infrared dust opacity for at least an entire Mars year, but there is no corresponding measurement of visible optical depth. It will take a combination of an orbiter with an infrared instrument with a lander with a visible camera to determine the interannual variation (or lack thereof) of the aerosol cycle.

The greatest potential for future work comes from the application of the Mars MM5 to a variety of atmospheric investigations. A more detailed analysis of the Martian boundary layer, ideally in comparison with high vertical resolution lander data, is important for better understanding the interplay between the atmosphere and the surface. Better understanding of the boundary layer would also be important for defining the conditions under which dust lifting (either by high wind stress or by dust devils) are met.

Further investigations of dust lifting at different locations and different times are also important. Simulation of the south polar region throughout the whole year should help determine if the thermal contrast of the polar cap always plays a significant role, or if other forces are dominant in other seasons. Simulations of dust lifting in other locations should also provide insight into which forcing mechanisms are important for generating high wind stresses in those locations.

Investigation of dust lifting by other processes, especially by dust devils, is another large avenue of future research. High-resolution simulations, where dust devils are actually resolved, present opportunities to define their triggering conditions as well as their dust lifting potential. Using this information, studies similar to Chapter 4 can be undertaken where the locations and occurrences of dust devils are examined.

The modeling of local dust storms, both by proscribing a pre-existing local dust storm and investigating its evolution, as well as trying to model the creation of local dust storms, is a ripe area of investigation. Understanding how a local dust storm grows into a regional or global storm can be aided by the combination of mesoscale and general circulation models.

While these are only general outlines of avenues of research, they present a clear picture of the wide range of possible future investigations. The problems described above would obviously have to be more narrowly defined, and some projects divided into smaller, answerable parts, before they could ask the questions capable of being answered. However, it is clear that the beginning of a better understanding of the dust cycle is possible, both with the rosy prospect of many near-future missions to Mars, as well as the availability of tools with which to analyze their data.

Appendix: Detailed Description of Model Conversion

A.1 Introduction

This appendix describes changes of the MM5 modeling system in order to apply the model to Mars (the Mars MM5). The PSU/NCAR Fifth-Generation Mars Mesoscale Model (MM5) is extensively documented in *A Description of the Fifth-Generation Penn State/NCAR Mesoscale Model (MM5)* [*Grell et al.*, 1994], *A Description of the Fifth-Generation Penn State/NCAR Mesoscale Model (MM5)* [*Haagenson et al.*, 1994] and *PSU/NCAR Mesoscale Modeling System Tutorial Class Notes and User's Guide: MM5 Modeling System Version 3* [*NCAR*, 2000]. At the time of writing, all of these documents, and additional descriptions, as well as the source code, are available at the website: *http://www.mmm.ucar.edu/mm5/mm5-home.html*. Here only the changes from the terrestrial version of the model as presented in those documents is described.

The model consists of two major portions:

- the "preprocessing" packages which are responsible for the definition of the experimental domain, as well as the generation of boundary and initial conditions;
- the numerical model integration of the fluid dynamic and ancillary equations.

The preprocessing step consists of several individual programs that progressively generate the necessary information. The entire modeling system is schematically shown in Figure A1, including in this case the general circulation model (GCM), which provides the context into which the Mars MM5 is embedded, and is responsible for generation of

boundary and initial conditions.

In the following sections changes to the modeling system as compared to the terrestrial version are described in the order in which the individual components are executed. One should compare Figure A1 with Figure 1-1 of *PSU/NCAR Mesoscale Modeling System Tutorial Class Notes and User's Guide: MM5 Modeling System Version 3* [*NCAR*, 2000].

A.2 TERRAIN

This is the first step to be executed in both the Martian and terrestrial versions. In the terrestrial version, the code is responsible for the definition of a number of basic domain properties. Initially the code defines the structure of the domains, including the number of grid points in both X and Y horizontal directions, the map projection and orientation of the domains (which provides the definition of X and Y previously mentioned, which need not be strictly latitude and longitude), and the grid point spacing (and hence model domain area). At this point in the processing only the two-dimensional surface definitions are constructed.

Next input maps of topography are interpolated to the newly defined model domains, as well as assignment of categorization of land use type (this specifies for each land use category a thermal inertia and albedo of the soil, soil moisture availability, and surface roughness length) for every grid point. In the Martian version of program all of the above processing is done, but the values will be overwritten with those generated in the next processing step (`MARSTERRAIN`).

Because there is no restriction on the placement of grid points, and the fact that the Coriolis parameter is dependent on latitude, the Coriolis parameter at each grid point needs to be calculated, and is done at this step. In the Martian version of this program, the value of the radius and the rotation rate of Mars are used instead of the terrestrial values. Martian values are taken from *Kieffer et al.* [1992].

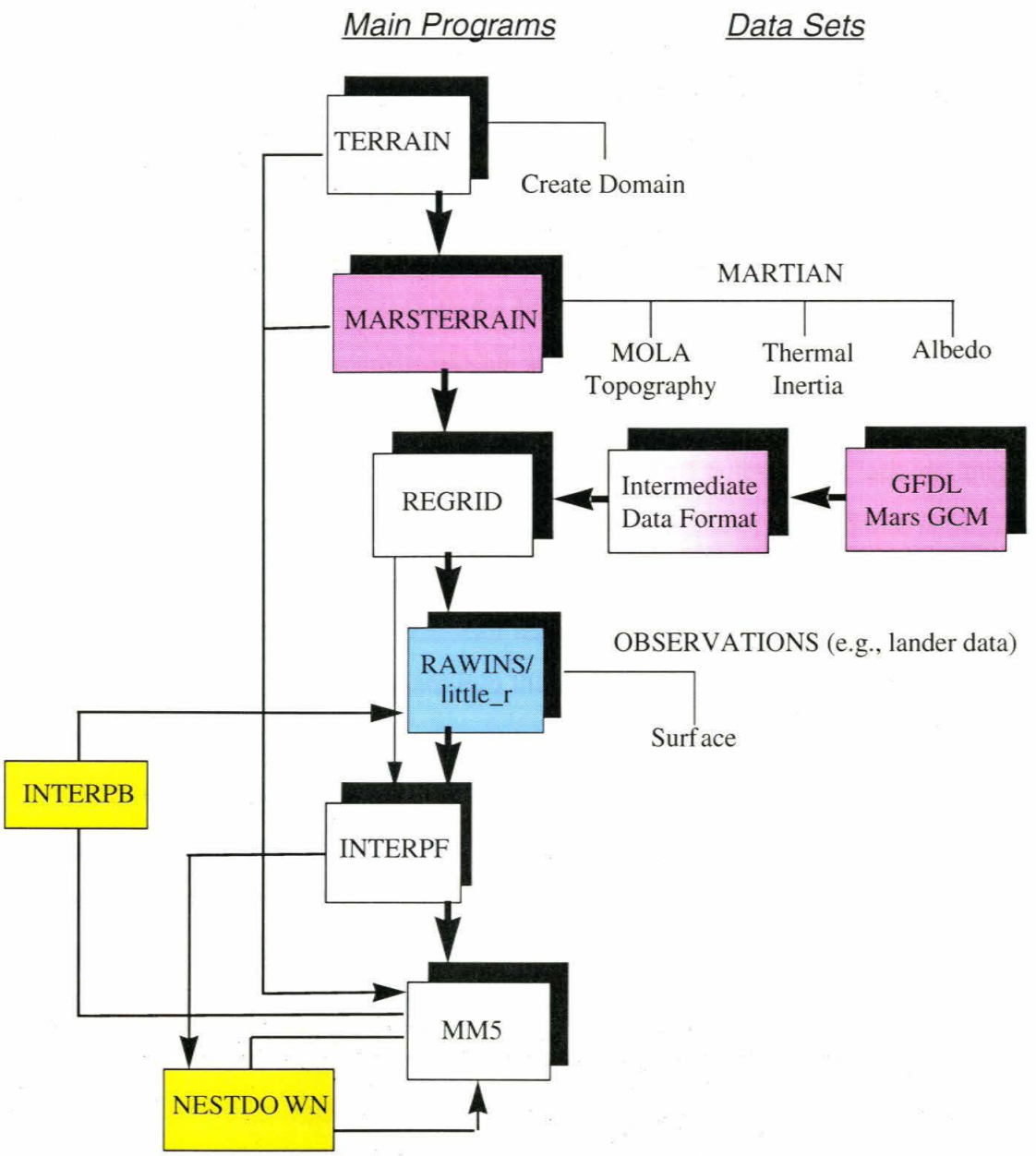

Figure A1: Flow chart of the MM5 modeling system. The white boxes represent original elements of the terrestrial MM5 system that are retained with modifications. Red boxes represent new additions to the Martian version. Blue boxes represent elements not used in the current Mars MM5 system. Yellow boxes represent unimplemented data manipulation packages. This figure is comparable to Figure 1-1 of *PSU/NCAR Mesoscale Modeling System Tutorial Class Notes and User's Guide: MM5 Modeling System Version 3* [*NCAR*, 2000].

A.3 MARSTERRAIN

The MARSTERRAIN program provides the definition of surface properties appropriate for Mars instead of those defined for the Earth in the previous preprocessing step. The need for an independent MARSTERRAIN program arises from the fact that the use of "land use categories" is inappropriate for Mars. There exist high resolution gridded maps of topography, albedo, and thermal inertia for Mars. It was deemed easier and more robust to avoid use of the intermediate terrestrial data archive format, which necessitated the writing of an interpolation scheme.

The topography dataset used in this work was the full pole-to-pole latitude-longitude gridded 1/16°map produced by the Mars Orbiter Laser Altimeter team [*Smith et al.*, 1999]. In the polar regions, a polar stereographic projection of the topography dataset, also provided by the Mars Orbiter Laser Altimeter team [*Smith et al.*, 1999], was used. In both of these cases, ingestion of this datasets into the model only required interpolation onto the chosen model domain.

For the albedo and thermal inertia fields, no single global map existed. In both of these cases, separate equatorial-to-mid-latitude maps (60° S to 60° N) existed from Viking data [*Palluconi and Kieffer*, 1981; *Pleskot and Miner*, 1981]. In addition, in the polar regions, maps of albedo and thermal inertia were taken from *Vasavada et al.* [2000]. Recently an equatorial-to-mid-latitude map of thermal inertia provided by the Thermal Emission Spectrometer [*Mellon et al.*, 2000] was added. For both albedo and thermal inertia, depending upon the definition and extent of the domain, some combination of the polar and/or equatorially-centered maps is used. Particular attention was paid to the merging of the datasets to reduce edging effects. In all cases, there has been an attempt to correct for atmospheric effects.

A.4 REGRID

The MM5 is an embedded model, which means by definition it requires forcing by boundary conditions and a specification of initial conditions. In the terrestrial version, this is provided by assimilated gridded objective analyses (such as National Centers for Environmental Prediction (NCEP) and European Centre for Medium Range Weather Forecasting (ECMWF) reanalyses), which result from the ingestion of radiosonde and satellite data into assimilation models. Obviously, such datasets are not available for Mars. Instead, output from the Geophysical Fluid Dynamics Laboratory (GFDL) Mars General Circulation Model (GCM) is used. `REGRID` requires global fields to be ingested in a specific data format. This format is specified in terms of the inclusion of header information, tags, and the actual meteorological field data. A further requirement is that the three-dimensional input meteorological field data must be on constant pressure surfaces. This is done in the terrestrial version by a ancillary program called `PREGRID`, which needs to be run only once for any given global dataset, and takes the global reanalyses and puts them on constant pressure surfaces, and writes the output in the intermediate data format needed by `REGRID`. `PREGRID` is not useful for the Martian version, since it is hardwired for specific terrestrial datasets. Instead, a new piece of code (`GCM2MM5`) was written to convert the GCM output into the `REGRID` intermediate data format. For the Martian version, this code also passes along the subsurface temperature fields, as well as surficial ice (both water and CO_2) amounts.

`REGRID` is primarily responsible for taking the global datasets, cropping them to the size of the model domain, and horizontally interpolating the atmospheric variables to the domain grid points. This horizontal interpolation is done on the constant pressure surfaces. In the Martian version, the three-dimensional fields interpolated are temperature, winds, specific humidity, and dust tracer amounts. The two-dimensional surface fields defined in the previous preprocessing steps are passed along without modification. New

two-dimensional surface fields (surface temperature, surface pressure, surface ice amounts, and the subsurface temperatures at twelve different layers) are generated in this step by the interpolation of the GCM fields.

This code is only slightly modified from the terrestrial version. The biggest modification is in the definition of the calendar, which is specified in the terrestrial version by the format "`YYYY-MM-DD_HH:MM:SS.ffff`." This was form was unsuitable for the Martian version, and was replaced with the format "`YY-DDD_HH:MM:SS.ffffffff`." This definition of calendar time is used throughout the rest of the modeling system from this point on. The only other modification was that pressure levels in the terrestrial version were required to be specified as integer values in Pa. At high levels in the Martian atmosphere, such a definition is unsuitable, and so real values of pressure were allowed.

A.5 RAWINS/little_r

An optional preprocessing step included in the terrestrial version is `RAWINS/little_r`. This program allows inclusion of radiosonde data for assimilation into the model integration. This preprocessing is not necessary for the generation of model initial or boundary conditions, but the ability to assimilate observations is a useful capability. In the Martian version, this step is skipped, but could conceivably be used in the future to assimilate surface weather station or orbiter data.

A.6 INTERPF

The MM5 model uses a terrain-following sigma coordinate in the vertical. Sigma is defined as

$$\sigma = \frac{P(z) - P_{top}}{P_{surf} - P_{top}} \tag{A.1}$$

where P is the pressure at the given location in the atmosphere, P_{top} is the specified pressure of the model top, and P_{surf} is the pressure of the surface at the given location. INTERPF is used for vertical interpolation of the three-dimensional meteorological fields from the constant pressure levels to these sigma levels. Interpolation is done by converting both the constant pressure levels and the sigma levels to a height grid, and then interpolating with respect to height. Upon completion of this program, boundary conditions and initial conditions are generated, and written to file. The initial conditions populate a domain identical to that of the model while the boundary conditions only populate the model walls.

Modification of INTERPF from the terrestrial version was the most extensive of all the preprocessing steps. It essentially required modification of definitions and physical constants. Specific definition and physical constant changes include:

- R, the atmospheric gas constant, is changed to 192 J K^{-1} kg^{-1} [*Zurek et al.*, 1992].
- g, the value of gravitational acceleration at the surface, is changed to 3.711 m s^{-2} [*Kieffer et al.*, 1992].
- c_p, the heat capacity of the atmosphere at constant pressure, is changed to 770 J K^{-1} kg^{-1} [*Touloukian and Makita*, 1970].
- P_0, the reference surface pressure (i.e., mean pressure at 0 m altitude), is changed to the average GCM equatorial surface pressure. This is because the definition of the MOLA 0 m altitude surface is the mean of the equatorial altitudes [*Smith et al.*, 1999]. This value is primarily used in the calculation of potential temperature necessary for vertical interpolation schemes.

An additional modification not implemented in the terrestrial version was the adjustment of surface pressure. The input topography is generally at much higher resolution than the GCM input fields. As such, the surface pressure may be appropriate to a height different

from the elevation at the given mesoscale model grid point. Therefore, the GCM derived surface pressure is interpolated to the actual elevation of the mesoscale model grid point.

A.7 INTERPB and NESTDOWN

The programs INTERPB and NESTDOWN are used to create boundary and initial conditions for the MM5 from previous MM5 simulations, including generation of embedded higher-resolution domains ("nests"). These codes are documented in the tutorial but have not been used to date for the Mars MM5. It is not anticipated that these codes would require any modification for use with the Mars MM5 system.

A.8 MM5

The MM5 is the core of the mesoscale modeling system. It contains the machinery to numerically integrate the fluid dynamical equations and ancillary equations. The model is extensively described in *A Description of the Fifth-Generation Penn State/NCAR Mesoscale Model (MM5)* [*Grell et al.*, 1994], *A Description of the Fifth-Generation Penn State/NCAR Mesoscale Model (MM5)* [*Haagenson et al.*, 1994], and *Dudhia* [1993]. It is this component of the system that has been most heavily modified.

Flow charts showing the organization of the model are provided in Figures A1, A2, and A3 of *A Description of the Fifth-Generation Penn State/NCAR Mesoscale Model (MM5)* [*Haagenson et al.*, 1994]. Briefly, it consists of initialization procedures, a time-integration section that drives the physical parameterizations, and procedures that handle output.

A significant difference between the Martian and terrestrial versions of the model is in differences in the length of day. This has two implications: one, the diurnal cycle of solar forcing must be driven in cycles of a Martian day (88775.2 s [*Kieffer et al.*, 1992]), and two, "hourly" sampling of the model for output must be generated at intervals of 3699 s

rather than 3600 s. Philosophically, there are two approaches that could be taken with respect to the model clock. First, the definition of a second could be changed to be 1/86400 of a Martian day. However, this is problematic, because all fluxes (and anything dependent upon time) are calculated as rates of change in SI-defined seconds. This could be resolved by changing physical constant definitions to use a "Martian second," but this seemed excessively complicated, prone to error, and would require conversion of output meteorological fields back into their SI-equivalents for comparison to any other datasets. Second, the definition of length of day and fractions thereof for the purposes of output could be changed, while holding the second to its SI definition. This is vastly simpler, and was the chosen option.

Many physical constants are defined and used throughout the model. These were changed as follows:

- R, the atmospheric gas constant, is changed to 192 J K^{-1} kg^{-1} [*Zurek et al.*, 1992].
- g, the value of gravitational acceleration at the surface, is changed to 3.711 m s^{-2} [*Kieffer et al.*, 1992].
- c_p, the heat capacity of the atmosphere at constant pressure, is changed to 770 J K^{-1} kg^{-1} [*Touloukian and Makita*, 1970].
- R_{planet}, the planetary radius, is changed to 3389.92 km [*Kieffer et al.*, 1992].
- Ω, the planetary rotation rate, is changed to 7.0776×10^{-5} s^{-1} ($= 2\pi/(88775.2\text{ s})$) [*Kieffer et al.*, 1992].
- P_0, the reference surface pressure (i.e., mean pressure at 0 m altitude), is inherited from the value calculated in the program `INTERPF` described above.

The terrestrial version of MM5 possessed a description of the progression of seasons and the diurnal cycle that was hardwired to the Earth. This was replaced by a generalized

orbital code that provides a time-evolving description of the intensity of solar insolation and the diurnal cycle of sun angles for each grid point. The orbital parameters (obliquity, eccentricity, argument of perihelion) appropriate to Mars were included to produce a description of the Martian year and day. The code is as implemented in the GFDL Mars GCM [*Wilson and Hamilton*, 1996]. As with most of the Martian physical parameterizations used in the Mars MM5, the fact that the Mars MM5 subroutines are directly derived from routines in the GFDL Mars GCM guarantees consistency in the representation of physical processes that assists in compatibility of the Mars MM5 simulations with the GFDL Mars GCM forcing.

The workhorse of the model is provided by the forecast routine, `SOLVE`. This subroutine embeds all of the physical parameterizations, and the numerical integration. This is the component of the MM5 that has been most heavily modified. The governing equations and the numerical approach to their integration are exhaustively documented in Chapter 2 of *A Description of the Fifth-Generation Penn State/NCAR Mesoscale Model (MM5)* [*Grell et al.*, 1994, pp. 1–15]. These fundamental routines that deal essentially fluid dynamics and discretization have not been modified.

`SOLVE` is the main driver for the physical parameterizations within the model. The implementation and ordering of the physical parameterization subroutines is illustrated in Figure A2. In the following section, the modified subroutines will be described in the order shown in this figure. The figure also shows subroutines that have been switched off because they provide either data assimilation (not currently used) or representation of physical processes inappropriate to Mars (i.e., cumulus parameterizations). These will not be discussed.

The presence of dust tracers in the model required the modification of subroutines dealing with advection, diffusion, and radiation. For advection and diffusion, the implemented routines to treat water transport (in its various phases) were extended to include transport of dust. Additionally, some parameters relating to total dust amount and dust injection rate

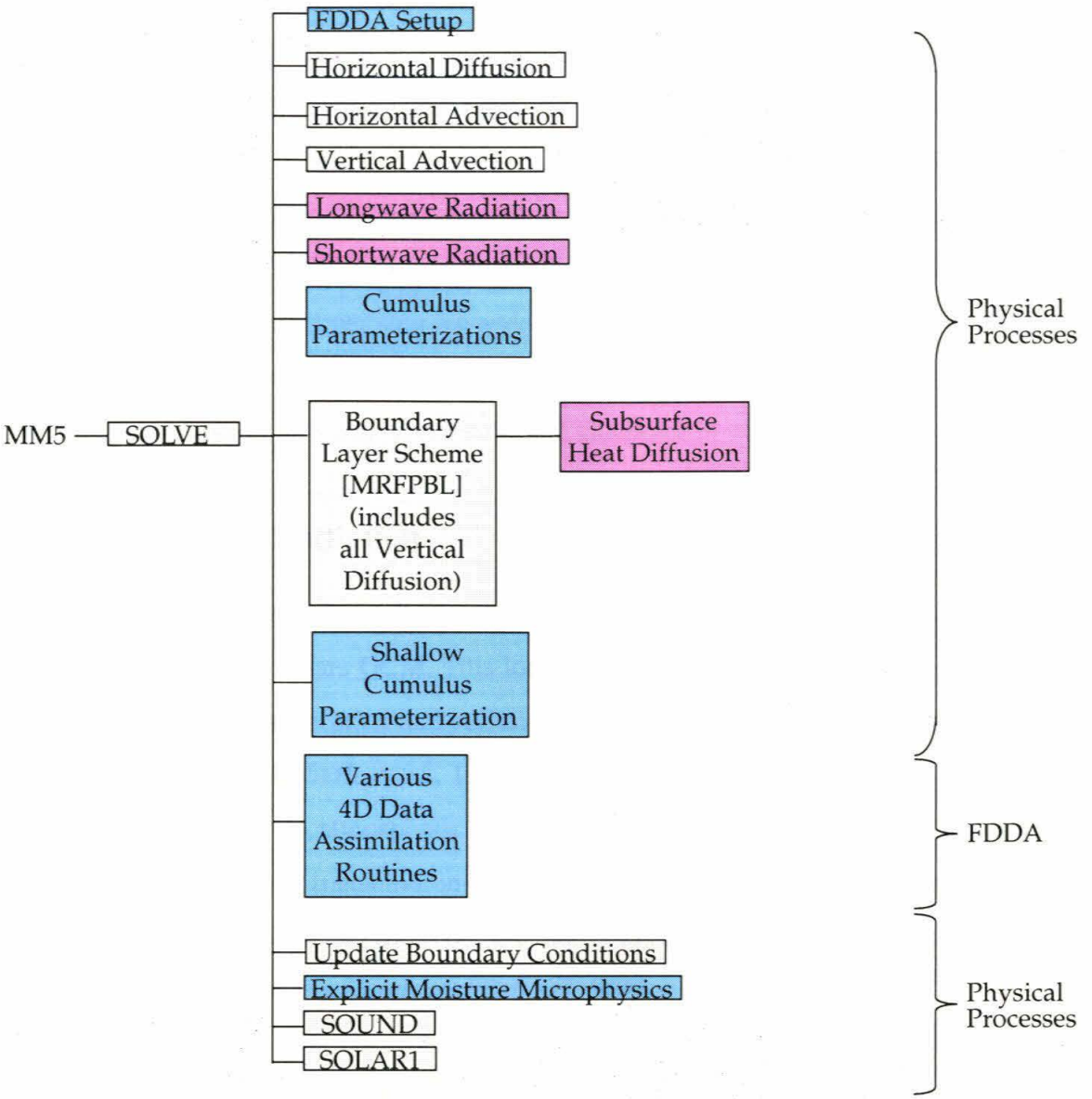

Figure A2: Schematic description of the forecast step in MM5 model. The gray boxes represent original elements of the terrestrial MM5 system that are unchanged, but extended to include dust tracers. Red boxes represent replacements of code in the terrestrial version with code appropriate to Mars. Blue boxes represent elements of the original terrestrial version turned off in the current Mars MM5 model. This figure is comparable to Figure A3 of *A Description of the Fifth-Generation Penn State/NCAR Mesoscale Model (MM5)* [*Haagenson et al.*, 1994]. SOUND is the subroutine that considers sound waves. FDDA is an acronym for Four-Dimensional Data Assimilation.

need to be specified in the run script used to initiate model integration. Dust is injected into and removed from the model in a subroutine added just before the radiation subroutines. Sedimentation is treated using a simple analytic formula that represents fall times based on the assumption that terminal velocity is readily attained. The equation is as given by *Haberle et al.* [1982] and appropriate for particles 0.6 and 2.5 μm, the two particle sizes treated by the model. Dust injection is treated by simply adding a fixed amount of dust of both particle sizes in each times step for which the lowest model level for any grid point at which the ground temperature exceeds the lowest level air temperature by 22 K. The flux of dust injected in each time step is constant and independent of location.

A.8.1 Longwave Radiation

The MM5 longwave radiation scheme was removed and replaced with the scheme implemented in the GFDL Mars GCM. This longwave scheme treats radiation in two broad bands associated with absorption and emission by dust and by CO_2. The dust scheme is described in detail by [*Haberle et al.*, 1982] and uses an emissivity approach (defining an effective emissivity for an atmospheric layer based on the amount of dust in that layer). The CO_2 scheme builds a transmission matrix appropriate to the 15 μm CO_2 band in the strong Lorentzian line limit and then uses the matrix to propagate radiation. The scheme is that of and fully described in *Goody and Belton* [1967].

A.8.2 Shortwave Radiation

The MM5 shorwave radiation scheme was also removed and replaced. Again, the implemented Martian schemes are the same as those used in the GFDL Mars GCM. Absorption of solar radiation by CO_2 in near-infrared bands is treated with a simple analytic formula developed by *Houghton* [1963] and as implemented by *Burk* [1976]. The treatment of dust interactions with radiation in the visible considers the full scattering and absorp-

tion processes. A two-stream delta-Eddington code is used as fully described by *Briegleb* [1992]. Dust properties (single-scattering albedo, asymmetry parameter, etc.) are taken from *Clancy and Lee* [1991].

A.8.3 Subsurface Heat Diffusion

Surface temperatures are calculated with a surface heat balance model that is called from within the boundary layer subroutine. Two of the three schemes included in the terrestrial model were either too complex (involving detailed treatment of surface vegetation and soil moisture availability, clearly inappropriate for Mars) or too simple (only one layer). The third scheme was appropriate, but did not extend deep enough to capture the annual wave. For consistency with the GCM, a fourth option (which is the default in the Mars model) was added that uses an implicit integration over 12 subsurface layers that extends to a depth of 2 m.

The physical constants used in the subsurface heat diffusion scheme are: bulk density of surficial soil, ρ_{ground}, 1500 kg m^{-3} [*Christensen and Moore*, 1992]; specific heat of soil, c, 837.2 J kg^{-1} K^{-1} [*Wechsler and Glaser*, 1965]; and latent heat of sublimation of CO_2, L_{CO_2}, 5.9×10^5 J kg^{-1} [*Paige*, 1985].

Bibliography

Anderson, F. S., R. Greeley, P. Xu, E. Lo, D. G. Blumberg, R. M. Haberle, and J. R. Murphy, Assessing the Martian surface distribution of aeolian sand using a Mars general circulation model, *J. Geophys. Res.*, *104*, 18,991–19,002, 1999.

Andrews, D. G., J. D. Mahlman, and R. W. Sinclair, Eliassen-Palm diagnostics of wave-mean flow interaction in the GFDL "SKYHI" general circulation model, *J. Atmos. Sci.*, *40*, 2768–2784, 1983.

Anthes, R. A., and T. Warner, Development of hydrodynamic models suitable for air pollution and other mesometeorological studies, *Mon. Wea. Rev.*, *106*, 1045–1078, 1978.

Arakawa, A., and V. R. Lamb, Computational design of the basic dynamical processes of the UCLA general circulation model, *Methods in Computational Physics*, *17*, 173–265, 1977.

Bagnold, R. A., *The Physics of Blown Sand and Desert Dunes*, Methuen, London, 1941.

Bandfield, J. L., P. R. Christensen, and M. D. Smith, Spectral data set factor analysis and end-member recovery: Application to analysis of Martian atmospheric particulates, *J. Geophys. Res.*, *105*, 9573–9588, 2000.

Beish, J. D., and D. C. Parker, Meteorological survey of Mars, 1969 – 1984, *J. Geophys. Res.*, *95*, 14,657–14,675, 1990.

Bohren, C. F., and D. R. Huffman, *Absorption and Scattering of Light by Small Particles*, Wiley, New York, 1983.

Briegleb, B. P., Delta-Eddington approximation for solar radiation in the NCAR community climate model, *J. Geophys. Res.*, *97*, 7603–7612, 1992.

Burk, S. D., Diurnal winds near the Martian polar caps, *J. Atmos. Sci.*, *33*, 923–939, 1976.

Christensen, P. R., Martian dust mantling and surface composition: Interpretation of thermophysical properties, *J. Geophys. Res.*, *87*, 9985–9998, 1982.

Christensen, P. R., and H. J. Moore, The Martian surface layer, in *Mars*, edited by H. H. Kieffer, B. M. Jakosky, C. W. Snyder, and M. S. Matthews, pp. 686–729, Univ. of Ariz. Press, Tucson, 1992.

Christensen, P. R., et al., Thermal Emission Spectrometer Experiment: Mars Observer Mission, *J. Geophys. Res.*, *97*, 7699–7718, 1992.

Clancy, R. T., and S. W. Lee, A new look at dust and clouds in the Mars atmosphere: Analysis of emission-phase-function sequences from global Viking IRTM observations, *Icarus*, *93*, 135–158, 1991.

Clancy, R. T., D. O. Muhleman, and G. L. Berge, Global changes in the 0-70 km thermal structure of the Mars atmosphere derived from 1975 to 1989 microwave CO spectra, *J. Geophys. Res.*, *95*, 14,543–14,554, 1990.

Clancy, R. T., A. W. Grossman, M. J. Wolff, P. B. James, D. J. Rudy, Y. N. Billawala, B. J. Sandor, S. W. Lee, and D. O. Muhleman, Water vapor saturation at low altitudes around Mars aphelion: A key to Mars climate?, *Icarus*, *122*, 36–62, 1996.

Clancy, R. T., B. J. Sandor, M. J. Wolff, P. R. Christensen, M. D. Smith, J. C. Pearl, B. J. Conrath, and R. J. Wilson, An intercomparison of ground-based millimeter, MGS TES, and Viking atmospheric temperature measurements: Seasonal and interannual variability of temperatures and dust loading in the global Mars atmosphere, *J. Geophys. Res.*, *105*, 9553–9572, 2000.

Colburn, D. S., J. B. Pollack, and R. M. Haberle, Diurnal variations in optical depth at Mars, *Icarus*, *79*, 159–189, 1989.

Conrath, B. J., Thermal structure of the Martian atmosphere during the dissipation of the dust storm of 1971, *Icarus*, *24*, 36–46, 1975.

Conrath, B. J., J. C. Pearl, M. D. Smith, W. C. Maguire, S. Dason, M. S. Kaelberer, and P. R. Christensen, Mars Global Surveyor Thermal Emission Spectrometer (TES) observations: Atmospheric temperatures during aerobraking and science phasing, *J. Geophys. Res.*, *105*, 9509–9520, 2000.

Curran, R. J., B. J. Conrath, R. A. Hanel, V. G. Kunde, and J. C. Pearl, Mars: Mariner 9 spectroscopic evidence for H_2O ice clouds, *Science*, *182*, 381–383, 1973.

Dudhia, J., A nonhydrostatic version of the Penn State-NCAR mesoscale model: Validation tests and simulation of an atlantic cyclone and cold front, *Mon. Wea. Rev.*, *121*, 1493–1513, 1993.

Fenton, L. K., J. C. Pearl, and T. Z. Martin, Mapping Mariner 9 dust opacities, *Icarus*, *130*, 115–124, 1997.

Gierasch, P. J., and R. M. Goody, A model of a Martian great dust storm, *J. Atmos. Sci.*, *30*, 169–179, 1973.

Goody, R. M., and M. J. S. Belton, Radiative relaxation times for Mars, *Planet. Space Sci.*, *15*, 247–256, 1967.

Greeley, R., Silt-clay aggregates on Mars, *J. Geophys. Res.*, *84*, 6248–6254, 1979.

Greeley, R., and J. D. Iversen, *Wind as a Geological Process on Earth, Mars, Venus, and Titan*, Cambridge Univ. Press, Cambridge, 1985.

Greeley, R., and R. Leach, A preliminary assessment of the effects of electrostatics on aeolian processes, in *Reports of Plantary Geology Program—1978–1979*, NASA TM-80339, pp. 304–307, 1979.

Greeley, R., R. Leach, B. R. White, J. D. Iversen, and J. B. Pollack, Threshold windspeeds for sand on Mars: Wind tunnel simulations, *Geophys. Res. Lett.*, *7*, 121–124, 1980.

Greeley, R., N. Lancaster, S. Lee, and P. Thomas, Martian aeolian process, sediments and features, in *Mars*, edited by H. H. Kieffer, B. M. Jakosky, C. W. Snyder, and M. S. Matthews, pp. 730–766, Univ. of Ariz. Press, Tucson, 1992.

Grell, G. A., J. Dudhia, and D. R. Stauffer, *A Description of the Fifth-Generation Penn State/NCAR Mesoscale Model (MM5), Tech. Rep.* NCAR/TN-398 + STR, Mesoscale and Microscale Meteorology Division, National Center for Atmospheric Research, 1994.

Haagenson, P. L., J. Dudhia, D. R. Stauffer, and G. A. Grell, *The Penn State/NCAR Mesoscale Model (MM5) Source Code Documentation, Tech. Rep.* NCAR/TN-392 + STR, Mesoscale and Microscale Meteorology Division, National Center for Atmospheric Research, 1994.

Haberle, R. M., and B. M. Jakosky, Atmospheric effects on the remote determination of thermal inertia on Mars, *Icarus*, *90*, 187–204, 1991.

Haberle, R. M., C. B. Leovy, and J. B. Pollack, A numerical model of the Martian polar cap winds, *Icarus*, *39*, 151–183, 1979.

Haberle, R. M., C. B. Leovy, and J. B. Pollack, Some effects of global dust storms on the atmospheric circulation of Mars, *Icarus*, *50*, 322–367, 1982.

Haberle, R. M., H. C. Houben, R. Hertenstein, and T. Herdtle, A boundary layer model for Mars: Comparison with Viking Lander and entry data, *J. Atmos. Sci.*, *50*, 1544–1559, 1993.

Haberle, R. M., et al., General circulation model simulations of the Mars Pathfinder atmospheric structure investigation/meterology data, *J. Geophys. Res.*, *104*, 8957–8974, 1999.

Hamilton, K., R. J. Wilson, J. D. Mahlman, and L. J. Umscheid, Climatology of the SKYHI troposphere-stratosphere-mesosphere general circulation model, *J. Atmos. Sci.*, *52*, 5–43, 1995.

Herr, K. C., and G. C. Pimental, Evidence for solid carbon dioxide in the upper atmosphere of Mars, *Science*, *167*, 496–499, 1969.

Hong, S.-Y., and H.-L. Pan, Nonlocal boundary layer vertical diffusion in a medium-range forecast model, *Mon. Wea. Rev.*, *124*, 2322–2339, 1996.

Houghton, J. T., The absoprtion of solar infra-red radiation by the lower stratosphere, *Quart. J. Roy. Meteor. Soc.*, *89*, 319–331, 1963.

Hourdin, F., A new representation of the CO_2 15-micron band for a Martian general circulation model, *J. Geophys. Res.*, *97*, 18,319–18,335, 1992.

Huguenin, R. L., S. M. Clifford, C. A. Sullivan, and K. J. Miller, Remote sensing evidence for oases on Mars, in *Reports of Plantary Geology Program—1978–1979*, NASA TM-80339, pp. 208–214, 1979.

Iversen, J. D., J. B. Pollack, R. Greeley, and B. R. White, Saltation threshold on Mars: The effect of interparticle froce, surface roughness, and low atmospheric density, *Icarus*, *29*, 381–393, 1976.

Jacobson, M. Z., *Fundamentals of Atmospheric Modeling*, Cambridge University Press, 1999.

Jakosky, B. M., and C. B. Farmer, The seasonal and global behavior of water vapor in the Mars atmosphere: Complete global results of the Viking atmospheric water detector experiment, *J. Geophys. Res.*, *87*, 2999–3019, 1982.

James, P. B., J. F. Bell III, R. T. Clancy, S. W. Lee, L. J. Martin, and M. J. Wolff, Global imaging of Mars by Hubble space telescope during the 1995 opposition, *J. Geophys. Res.*, *101*, 18,883–18,890, 1996.

James, P. B., J. L. Hollingsworth, M. J. Wolff, and S. W. Lee, North polar dust storms in early spring on Mars, *Icarus*, *138*, 64–73, 1999.

Johnson, D. W., P. Harteck, and R. R. Reeves, Dust injection into the Martian atmosphere, *Icarus*, *26*, 441–443, 1975.

Joshi, M., R. Haberle, J. Barnes, J. Murphy, and J. Schaeffer, Low-level jets in the nasa ames mars general circulation model, *J. Geophys. Res.*, *102*, 6511–6523, 1997.

Kahn, R., R. Goody, and J. Pollack, The Martian twilight, *J. Geophys. Res.*, *86*, 5833–5838, 1981.

Kahn, R. A., T. Z. Martin, R. W. Zurek, and S. W. Lee, The Martian dust cycle, in *Mars*, edited by H. H. Kieffer, B. M. Jakosky, C. W. Snyder, and M. S. Matthews, pp. 1017–1053, Univ. of Ariz. Press, Tucson, 1992.

Kieffer, H. H., B. M. Jakosky, and C. W. Snyder, The planet Mars: From antiquity to the present, in *Mars*, edited by H. H. Kieffer, B. M. Jakosky, C. W. Snyder, and M. S. Matthews, pp. 1–33, Univ. of Ariz. Press, Tucson, 1992.

Kirk, R. L., et al., Digital photogrammetric analysis of the IMP camera images: Mapping the Mars Pathfinder landing site in three dimensions, *J. Geophys. Res.*, *104*, 8869–8887, 1999.

Leovy, C. B., R. W. Zurek, and J. B. Pollack, Mechanisms for Mars dust storms, *J. Atmos. Sci.*, *30*, 749–762, 1973.

Malin, M. C., G. E. Danielson, A. P. Ingersoll, H. Masursky, J. Veverka, M. A. Ravine, and T. A. Soulanille, Mars Observer Camera, *J. Geophys. Res.*, *97*, 7699–7718, 1992.

Malin, M. C., et al., Early views of the Martian surface from the Mars orbiter camera of Mars Global Surveyor, *Science*, *279*, 1681–1685, 1998.

Martin, T. Z., Thermal infrared opacity of the Mars atmosphere, *Icarus*, *66*, 2–21, 1986.

Martin, T. Z., and M. I. Richardson, New dust opacity mapping from Viking infrared thermal mapper data, *J. Geophys. Res.*, *98*, 10,941–10,949, 1993.

Mellon, M. T., B. M. Jakosky, H. H. Kieffer, and P. R. Christensen, High-resolution thermal inertia mapping from the Mars Global Surveyor Thermal Emission Spectrometer, *Icarus*, *148*, 437–455, 2000.

Mellor, G. L., and T. Yamada, Development of a turbulence closure model for geophysical fluid problems, *Rev. Geophys. Space Phys.*, *20*, 851–875, 1982.

Metzger, S. M., J. R. Carr, J. R. Johnson, T. J. Parker, and M. T. Lemmon, Dust devil vortices seen by the Mars Pathfinder camera, *Geophys. Res. Lett.*, *26*, 2781–2784, 1999.

Murphy, J. R., The Martian atmospheric dust cycle: Insights from numerical model simulations, in *The Fifth International Conference on Mars*, Abstract #6087 in LPI Contribution No. 972, Lunar and Planetary Institute, Houston, 1999, (CDROM).

Murphy, J. R., J. B. Pollack, R. M. Haberle, C. B. Leovy, O. B. Toon, and J. Schaeffer, Three-dimensional numerical simulation of Martian global dust storms, *J. Geophys. Res.*, *100*, 26,357–26,376, 1995.

NCAR, *PSU/NCAR Mesoscale Modeling System Tutorial Class Notes and User's Guide: MM5 Modeling System Version 3*, Mesoscale and Microscale Meteorology Division, National Center for Atmospheric Research, Boulder, Colorado, 2000.

Ockert-Bell, M. E., J. F. Bell III, J. B. Pollack, C. P. McKay, and F. Forget, Absorption and scattering properties of the Martian dust in the solar wavelengths, *J. Geophys. Res.*, *102*, 9039–9050, 1997.

Paige, D. A., The annual heat balance of the martian polar caps from viking observations, Ph.D. thesis, California Institute of Technology, 1985.

Paige, D. A., and K. D. Keegan, Thermal and albedo mapping of the polar regions of Mars using Viking thermal mapper observations. 2. South polar region, *J. Geophys. Res.*, *99*, 25,993–26,013, 1994.

Paige, D. A., J. E. Bachman, and K. D. Keegan, Thermal and albedo mapping of the polar regions of Mars using Viking thermal mapper observations. 1. North polar region, *J. Geophys. Res.*, *99*, 25,959–25,991, 1994.

Palluconi, F. D., and H. H. Kieffer, Thermal inertia mapping of Mars for 60°S to 60°N, *Icarus*, *45*, 415–426, 1981.

Peterfreund, A. R., and H. H. Kieffer, Thermal infrared properties of the Martian atmosphere. 3. Local dust clouds, *J. Geophys. Res.*, *84*, 2853–2863, 1979.

Pleskot, L. K., and E. D. Miner, Time variability of Martian bolometric albedo, *Icarus*, *45*, 179–201, 1981.

Pollack, J. B., and J. N. Cuzzi, Scattering by nonspherical particles of size comparable to a wavelength: A new semi-empirical theory and its application to tropospheric aerosols, *J. Atmos. Sci.*, *37*, 868–881, 1980.

Pollack, J. B., D. S. Colburn, R. Kahn, J. Hunter, W. V. Camp, C. E. Carlston, and M. R. Wolf, Properties of aerosols in the Martian atmosphere, as inferred from Viking Lander imaging data, *J. Geophys. Res.*, *82*, 4479–4496, 1977.

Pollack, J. B., D. S. Colburn, M. Flasar, R. Kahn, C. E. Carlston, and D. Pidek, Properties and effects of dust particles suspended in the Martian atmosphere, *J. Geophys. Res.*, *84*, 2929–2945, 1979.

Pollack, J. B., R. M. Haberle, J. R. Murphy, J. Schaeffer, and H. Lee, Simulations of the general-circulation of the Martian atmosphere: 2. seasonal pressure variations, *J. Geophys. Res.*, *98*, 3149–3181, 1993.

Pollack, J. B., M. E. Ockert-Bell, and M. K. Shepard, Viking Lander image analysis of Martian atmospheric dust, *J. Geophys. Res.*, *100*, 5235–5250, 1995.

Renno, N. O., A. A. Nash, J. Lunine, and J. Murphy, Martian and terrestrial dust devils: Test of a scaling theory using Pathfinder data, *J. Geophys. Res.*, *105*, 1859–1865, 2000.

Richardson, M. I., Comparison of microwave and infrared measurements of Martian atmospheric temperatures: Implications for short-term climate variability, *J. Geophys. Res.*, *103*, 5911–5918, 1998.

Richardson, M. I., A general circulation model study of the Mars water cycle, Ph.D. thesis, University of California, Los Angeles, 1999.

Ryan, J. A., and R. D. Lucich, Possible dust devils, vortices on Mars, *J. Geophys. Res.*, *88*, 11,005–11,011, 1983.

Savijärvi, H., and T. Siili, The Martian slope winds and the nocturnal PBL jet, *J. Atmos. Sci.*, *50*, 77–88, 1993.

Schmidt, D. S., R. A. Schmidt, and J. D. Dent, Electrostatic force on saltating sand, *J. Geophys. Res.*, *103*, 8997–9001, 1998.

Schofield, J. T., J. R. Barnes, D. Crisp, R. M. Haberle, S. Larsen, J. A. Magalhães, J. R. Murphy, A. Seiff, and G. Wilson, The Mars Pathfinder Atmospheric Structure Investigation/Meteorology (ASI/MET) Experiment, *Science*, *278*, 1752–1758, 1997.

Seiff, A., Mars atmospheric winds indicated by motion of the Viking landers during parachute descent, *J. Geophys. Res.*, *98*, 7461–7474, 1993.

Siili, T., R. M. Haberle, and J. R. Murphy, Sensitivity of Martian southern polar cap edge winds and surface stresses to dust optical thickness and to the large-scale sublimation flow, *Adv. Space Res.*, *19*, 1241–1244, 1997.

Siili, T., R. M. Haberle, J. R. Murphy, and H. Savijärvi, Modelling of the combined late-winter ice cap edge and slope winds in Mars' hellas and argyre regions, *Planetary and Space Science*, *47*, 951–970, 1999.

Smith, D. E., et al., The global topography of Mars and implications for surface evolution, *Science*, *284*, 1495–1503, 1999.

Smith, M. D., J. L. Bandfield, and P. R. Christensen, Separation of atmospheric and surface spectral features in Mars Global Surveyor Thermal Emission Spectrometer (TES) spectra, *J. Geophys. Res.*, *105*, 9589–9608, 2000a.

Smith, M. D., J. C. Pearl, B. J. Conrath, and P. R. Christensen, Mars Global Surveyor Thermal Emission Spectrometer (TES) observations of dust opacity during aerobraking and science phasing, *J. Geophys. Res.*, *105*, 9539–9552, 2000b.

Smith, P. H., and M. Lemmon, Opacity of the Martian atmosphere measured by the Imager for Mars Pathfinder, *J. Geophys. Res.*, *104*, 8975–8985, 1999.

Tamppari, L. K., R. W. Zurek, and D. A. Paige, Viking era water ice clouds, *J. Geophys. Res.*, *105*, 4087–4108, 2000.

Thomas, P., and P. J. Gierasch, Dust devils on Mars, *Science*, *230*, 175–177, 1985.

Tomasko, M. G., L. R. Doose, M. Lemmon, P. H. Smith, and E. Wegryn, Properties of dust in the Martian atmosphere from the Imager on Mars Pathfinder, *J. Geophys. Res.*, *104*, 8987–9007, 1999.

Toon, O. B., J. B. Pollack, and C. Sagan, Physical properties of the particles composing the Martian dust storm of 1971-1972, *Icarus*, *30*, 663–696, 1977.

Touloukian, Y. S., and T. Makita, Specific heat: Nonmetallic liquids and gases, in *Thermophysical Properties of Matter*, edited by Y. S. Touloukian, vol. 6, pp. 143–151, IFI/Plenum, 1970.

Troen, I. B., and L. Mahrt, A simple model of the atmospheric boundary layer: Sensitivity to surface evaporation, *Boundary-Layer Meteorology*, *37*, 129–148, 1986.

Vasavada, A. R., J.-P. Williams, D. A. Paige, K. E. Herkenhoff, N. T. Bridges, R. Greeley, B. C. Murray, D. S. Bass, and K. S. McBride, Surface properties of Mars' polar layered deposits and polar landing sites, *J. Geophys. Res.*, *105*, 6961–6970, 2000.

Warren, S. G., Optical constants of ice from the ultraviolet to the microwave, *Appl. Opt.*, *23*, 1206–1225, 1984.

Wechsler, A. E., and P. E. Glaser, Pressure effects on postulated lunar materials, *Icarus*, *4*, 335–352, 1965.

White, B. R., Soil transport by winds on Mars, *J. Geophys. Res.*, *84*, 4643–4651, 1979.

White, B. R., and R. Greeley, Martian dust threshold measurements—Simulation under heated surface conditions, in *MECA Workshop on Dust on Mars III*, edited by S. Lee, LPI Tech. Rept. 89-01, pp. 60–61, 1989.

Wilson, G. R., and M. Joshi, The Martian surface boundary layer, in *The Fifth International Conference on Mars*, Abstract #6221 in LPI Contribution No. 972, Lunar and Planetary Institute, Houston, 1999, (CDROM).

Wilson, R. J., A general ciculation model simulation of the Martian polar warming, *Geophys. Res. Lett.*, *24*, 123–126, 1997.

Wilson, R. J., and K. Hamilton, Comprehensive model simulation of thermal tides in the Martian atmosphere, *J. Atmos. Sci.*, *53*, 1290–1326, 1996.

Wilson, R. J., and M. I. Richardson, The Martian atmosphere during the Viking Mission, 1: Infrared measurements of atmospheric temperatures revisited, *Icarus*, *145*, 555–579, 2000.

Ye, Z. J., M. Segal, and R. A. Pielke, A comparative study of daytime thermally induced upslope flow on Mars and Earth, *J. Atmos. Sci.*, *47*, 612–628, 1990.

Zurek, R. W., Inference of dust opacities for the 1977 Martian great dust storms from Viking Lander 1 pressure data, *Icarus*, *45*, 202–215, 1981.

Zurek, R. W., J. R. Barnes, R. M. Haberle, J. B. Pollack, J. E. Tillman, and C. B. Leovy, Dynamics of the atmosphere of Mars, in *Mars*, edited by H. H. Kieffer, B. M. Jakosky, C. W. Snyder, and M. S. Matthews, pp. 835–933, Univ. of Ariz. Press, Tucson, 1992.